



UNIL | Université de Lausanne

Unicentre

CH-1015 Lausanne

<http://serval.unil.ch>

Year : 2018

MULTI-MODAL MR IMAGE PROCESSING AT HIGH FIELD FOR THALAMIC NUCLEI SEGMENTATION: APPLICATION TO GAMMA KNIFE SURGERY

Najdenovska Elena

Najdenovska Elena, 2018, MULTI-MODAL MR IMAGE PROCESSING AT HIGH FIELD FOR
THALAMIC NUCLEI SEGMENTATION: APPLICATION TO GAMMA KNIFE SURGERY

Originally published at : Thesis, University of Lausanne

Posted at the University of Lausanne Open Archive <http://serval.unil.ch>

Document URN : urn:nbn:ch:serval-BIB_7983F1D18D965

Droits d'auteur

L'Université de Lausanne attire expressément l'attention des utilisateurs sur le fait que tous les documents publiés dans l'Archive SERVAL sont protégés par le droit d'auteur, conformément à la loi fédérale sur le droit d'auteur et les droits voisins (LDA). A ce titre, il est indispensable d'obtenir le consentement préalable de l'auteur et/ou de l'éditeur avant toute utilisation d'une oeuvre ou d'une partie d'une oeuvre ne relevant pas d'une utilisation à des fins personnelles au sens de la LDA (art. 19, al. 1 lettre a). A défaut, tout contrevenant s'expose aux sanctions prévues par cette loi. Nous déclinons toute responsabilité en la matière.

Copyright

The University of Lausanne expressly draws the attention of users to the fact that all documents published in the SERVAL Archive are protected by copyright in accordance with federal law on copyright and similar rights (LDA). Accordingly it is indispensable to obtain prior consent from the author and/or publisher before any use of a work or part of a work for purposes other than personal use within the meaning of LDA (art. 19, para. 1 letter a). Failure to do so will expose offenders to the sanctions laid down by this law. We accept no liability in this respect.



UNIL | Université de Lausanne

Faculté de biologie
et de médecine

Centre d'Imagerie BioMédicale,
Département de radiodiagnostic et radiologie interventionnelle, CHUV

**MULTI-MODAL MR IMAGE PROCESSING AT HIGH
FIELD FOR THALAMIC NUCLEI SEGMENTATION:
APPLICATION TO GAMMA KNIFE SURGERY**

Thèse de doctorat en sciences de la vie (PhD)

présentée à la

Faculté de biologie et de médecine
de l'Université de Lausanne

par

Elena Najdenovska

Ingénieure en génie électrique et électronique
diplômée de l'Ecole Polytechnique Fédérale de Lausanne

Jury:

Prof. Pedro Romero, président
Prof. Marc Levivier, directeur de thèse
Dr. Meritxell Bach Cuadra, co-directrice de thèse
Prof. Jocelyne Bloch, experte
Prof. Mauricio Reyes, expert
Prof. Benoit Dawant, expert

Lausanne, 2018

Imprimatur

Vu le rapport présenté par le jury d'examen, composé de

Président·e	Monsieur Prof. Pedro Romero
Directeur·trice de thèse	Monsieur Prof. Marc Levivier
Co-directeur·trice	Madame Dre Meritxell Bach Cuadra
Expert·e·s	Madame Dre Jocelyne Bloch Monsieur Prof. Mauricio Reyes Monsieur Prof. Benoit Dawant

le Conseil de Faculté autorise l'impression de la thèse de

Madame Elena Najdenovska

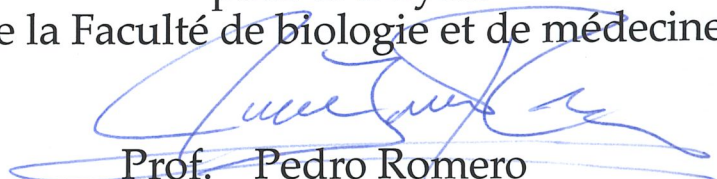
Msc en génie électrique et électronique EPFL, Suisse

intitulée

**MULTI-MODAL MR IMAGE PROCESSING AT HIGH FIELD FOR
THALAMIC NUCLEI SEGMENTATION:
APPLICATION TO GAMMA KNIFE SURGERY**

Lausanne, le 1 mars 2018

pour le Doyen
de la Faculté de biologie et de médecine



Prof. Pedro Romero

На мама, тато & дада

Acknowledgements

The whole journey as a PhD student has been an extraordinary experience and an extremely valuable occurrence for my professional growth. As a matter of fact, it was the people who made possible this opportunity and surrounded me throughout the entire path that brought the memorable and the successful side of it. Hence, I would like to dedicate this section to acknowledge them for all of their help, support and contribution to this work.

First of all, I would like to express my profound gratitude and appreciation to both of mine supervisors: Dr. Meritxell Bach Cuadra and Prof. Marc Levivier. You have been incredible mentors and a constant source of support throughout the years, no matter what the challenge was. Meri, since our first collaboration for my Master thesis, you've become an inspiration and the main reason for my affection towards the medical imaging research. Moreover, your guide and unceasing bright ideas, your trust and your effort to always provide the best for your collaborators, have made this thesis work completely enjoyable and educationally enduring in many spheres. Prof. Levivier, your kindness, faith and continuous encouragement, have always motivated me to go further and to give the best from me.

My heartfelt thanks goes as well to Prof. Jean-Philippe Thiran who has been, since the beginning, heavily involved in the project and was persistently bringing novel thoughts and perspectives, but moreover, an immeasurable support and new opportunities. Special thanks also to Dr. Constantin Tuleasca, my binôme, for all the neurosurgical insights, for the pleasant teamwork and, especially, for always seeing the bigger picture and pushing me towards it.

I would like to deeply thank as well Dr. Giovanni Battistella and Dr. Eleonora Fornari for accompanying me on the road of discovering the thalamus and, overall, for making it pleasant the challenge of building novel thalamic parcellation method. Also, my sincerest thanks to Prof. Philippe Maeder for his patience and time dedicated to analyze and interpret each new result as well as for the admirable knowledge of thalamus and its nuclei that he unselfishly shared and thereupon, made easier for me to confront the thesis defies.

Many warm thanks also to each of my current and former MIAL colleagues who, despite all topic diversities and spatial disparity, were always there to discuss, to advise or to search together for the solution. For this, I am especially grateful to Mário João, Carlos and Seb, with

Acknowledgements

who it was genuinely fun and pleasurable to share this path. Moreover, along the way, between conferences, courses assignments and team gatherings, a great friendship was born making this journey even more unforgettable. I am also extremely grateful to João, Yasser and Timo. Although we started collaborating towards the end of this project, all three of them, with their expertise and tremendous work, brought even bigger value to my thesis.

I was also very fortunate to be surrounded with other amazing colleagues, collaborators and office-mates, such as Naghmeh, Emeline, Jakub, Paul, Elsa, Sarah, Tatiana, Lena, Benedetta, Serena, Alessandra, Marina, Vijay, . . . , whose friendship is one of the most valuable things I gain in this experience. I am equally grateful to each one of them for all of their immeasurable help and encouragement, precious advises and care, the brainstorming walks, the late working hours keeping company to each other, as well as for all of the cheerful breaks, shared sweets and chocolates, shared fun and laughter, shared memories that will remain for a lifetime.

Finally, I would like to express my deepest gratitude to my family, my sister and my parents, who has been my eternal backbone and perpetual force supply for pursuing my dreams. I thank you from the bottom of my heart for all the unconditional love and infinite support, for all the enormous sacrifices and for never stop believing in me even in the hardest times. Because of them I become the person I am today and for all of this I dedicate this work to them!

E. N.

Abstract

The thalamus is a preeminent brain relay and has a substantial role in regulating the motor and the sensory signals driven by the cortical-subcortical pathways. Although relatively small in size, it is characterised by a complex anatomical architecture built of numerous small nuclei, differing between them in both histological and functional aspect. The nuclei are mediating the broadly spread involvement of the thalamus in the neurological functioning and therefore, are of key importance in many neurodevelopmental and neurodegenerative studies and clinical treatments.

The central interest in this thesis is the ventro-intermediate thalamic nuclei (Vim) that represents the most commonly used target for treatment of drug-resistant patients in functional neurosurgical procedures, such as Deep Brain Stimulation and Gamma Knife Surgery. The treatment planning of these procedures is mainly depended on images obtained from Magnetic Resonance Imaging (MRI) techniques that presents an enhanced characterisation of the soft tissue. Unfortunately, current standard MRI protocols used in everyday clinical practice are not able to provide a direct visualisation of the thalamic subparts and therefore, alternatively, indirect targeting approaches, prone to engender variabilities, are applied. Hence, a standardisation of the targeting procedure via computer-assisted image-processing techniques becomes of crucial importance to support the treatment planning.

The diffusion-weighted MR images (DWI) by depicting the water molecules displacement give exquisite details about the underlying tissue microstructure and therefore, are able to discriminate the thalamic nuclei regarding their different fibre characteristics. For the problematic of automated parcellation of the thalamic subparts, several methods exploring the DWI information have been proposed, but they are mainly based on coarse diffusion measures. In this thesis, I propose the use of the orientation distribution functions (ODF) expressed in spherical harmonics basis that is fully characterising the diffusion process at each voxel and therefore outperforms the state-of-the art features. The built framework was tested in an extensive cohort of 123 healthy subjects and 65 tremor patients demonstrating its ability of robust and reproducible segmentation of seven thalamic groups of nuclei closely matching the histological atlas of Morel. One of them is the group of motor-related nuclei including

Abstract

the Vim, whose spatial distribution was further validated in a follow-up data of 18 tremor patients. However, the DWI are mainly limited by their spatial resolution and therefore could not provide more refined outline comparable to the size of the thalamic nuclei.

Ultra-high magnetic-field of 7T allows an improved spatial resolution, considerably increased signal to noise ratio as well as a superior sensitivity to magnetic susceptibility engendered contrast. In that context, the susceptibility-weighted images (SWI) acquired at 7 T are not only providing a complementary tissue characterisations regarding the 3T DWI but also they allow a direct visualisation of the thalamic subparts. Another contribution of this thesis refers the image analysis developments for exploring the 7T SWI advantages that, in current literature are done mainly in a qualitative manner. For five young healthy subjects, the spatial distribution of the thalamic subparts resulting from the ODF-based clustering was validated. Moreover, the comparison between the visually distinguishable Vim against the clinical targeting and the automatically segmented group of motor nuclei gave new insights of this nucleus localisation. Classical atlas-based registration techniques for segmenting the VIM based on 7T SWI were also applied. Finally, the combination between the spatial prior of the Vim and the intensity-based features distinguishable on 7T SWI led to an automated discrimination of the Vim area.

Résumé

Le thalamus est une région-relais cérébrale prééminente qui joue un rôle important dans la régulation du moteur et des signaux sensoriels conduits par les voies cortico-sous-corticales. Malgré sa taille relativement petite, il se caractérise par une architecture anatomique complexe constituée de nombreux petits noyaux qui diffèrent entre eux sur le plan histologique et fonctionnel. Les noyaux modèrent la grande implication du thalamus dans le fonctionnement neurologique et, par conséquent, sont d'une importance clé dans de nombreuses études neurodéveloppementales et neurodégénératives ainsi que des traitements cliniques.

L'intérêt central de cette thèse est le noyau thalamique ventro-intermédiaire (Vim) qui représente la cible la plus couramment utilisée pour le traitement des tremblements pharmaco-résistants dans le cadre d'interventions neurochirurgicales fonctionnelles, telles que la stimulation cérébrale profonde et la chirurgie Gamma Knife. La planification du traitement de ces procédures dépend principalement des images obtenues à l'aide de techniques d'imagerie par résonance magnétique (IRM) qui présentent une meilleure caractérisation des tissus mous. Malheureusement, les protocoles d'IRM standards actuellement utilisés dans la pratique clinique quotidienne ne sont pas capables de fournir une visualisation directe des sous-parties thalamiques. Comme alternative, des approches de ciblage indirect susceptibles d'engendrer des variabilités, sont appliquées. Par conséquent, une standardisation de la procédure de ciblage par des techniques de traitement d'images assistées par ordinateur devient d'une importance cruciale pour soutenir la planification du traitement.

Les images d'IRM pondérées en diffusion (DWI), en dépeignant le déplacement des molécules d'eau, donnent des détails exquis sur la microstructure tissulaire sous-jacente et sont donc capables de discriminer les noyaux thalamiques par leurs différentes caractéristiques de fibres. Dans le domaine de la parcellisation automatisée des sous-parties thalamiques, plusieurs méthodes explorant l'information de DWI ont été proposées, mais elles sont principalement basées sur des mesures de diffusion grossière. Dans cette thèse, je propose l'utilisation des fonctions de distribution d'orientation (ODF) exprimées en harmoniques sphériques qui caractérisent pleinement le processus de diffusion à chaque voxel et ainsi surpassent les caractéristiques de l'état de l'art. La méthode développée a été testée dans une vaste cohorte de 123

Résumé

sujets sains et 65 patients présentant des tremblements, démontrant sa capacité à segmenter, de façon robuste et reproductible, sept groupes de noyaux thalamiques correspondant étroitement à l'histologie présentée dans l'atlas de Morel. L'un d'entre eux est le groupe des noyaux liés à la motricité, incluant le Vim, dont la distribution spatiale a été validée dans les données de suivi de 18 patients atteints de tremblements. Cependant, les DWI sont principalement limitées par leur résolution spatiale et ne peuvent donc pas fournir un contour plus raffiné comparable à la taille des noyaux thalamiques.

Le champ magnétique ultra-élevé de 7 T permet une résolution spatiale améliorée, un rapport signal sur bruit considérablement augmenté ainsi qu'une sensibilité supérieure au contraste engendré par la susceptibilité magnétique. Dans ce contexte, les images pondérées par la susceptibilité (SWI) acquises à 7 T fournissent non seulement une caractérisation complémentaire des tissus en ce qui concerne le 3W DWI, mais permettent également une visualisation directe des sous-parties thalamiques, dont le Vim. Une autre contribution de cette thèse concerne les développements de l'analyse d'images pour explorer les avantages du SWI à 7 T lesquels, dans la littérature actuelle, sont réalisés principalement de manière qualitative. Pour cinq jeunes sujets sains, la distribution spatiale des sous-parties thalamiques résultant du regroupement basé sur l'ODF a été validée. De plus, la comparaison entre le Vim visuellement discernable, le ciblage clinique et le groupe de noyaux moteurs automatiquement segmenté a donné de nouvelles informations sur la localisation de ce noyau. Des techniques classiques basées sur des atlas pour segmenter le Vim en utilisant l'information de SWI à 7 T ont également été appliquées. Enfin, la combinaison entre l'a priori spatial du Vim et les caractéristiques basées sur l'intensité que l'on peut distinguer sur le 7 T SWI a conduit à une discrimination automatique de la région de Vim.

Table des matières

Acknowledgements	i
Abstract (English/Français)	iii
1 Introduction	1
1.1 Thalamus	1
1.1.1 Thalamic function	5
1.1.2 Clinical target	5
1.2 Magnetic Resonance Imaging of the thalamus	8
1.2.1 Diffusion Weighted Imaging	9
1.2.2 Susceptibility Weighted Imaging	13
1.3 Thesis goals and outline	15
Bibliographie	17
2 Thalamic Parcellation	25
2.1 Introduction	25
2.2 Materials and methods	27
2.2.1 Data	27
2.2.2 Pre-processing	28
2.2.3 Thalamus extraction	28
2.2.4 Reconstruction of the orientation distribution functions (ODFs)	29
2.2.5 Clustering of the thalamic nuclei	31
2.2.6 Evaluation of the results	32
2.3 Results	34
2.4 Discussion	39
2.5 Conclusion	43
Bibliographie	45

3	Evaluation of Thalamic Parcellation in Clinical Data	51
3.1	Introduction	51
3.2	Thalamic Parcellation in Drug-resistant Tremor Patients	52
3.3	Validation of the Segmented Motor Group of Nuclei	53
3.4	Graph-cut Partition of the Motor Group of Nuclei	54
3.4.1	Graph notions	54
3.4.2	Graph partition	54
3.4.3	VLV subdivision	55
3.5	Study Extension on DBS data	57
3.6	Discussion	58
3.7	Conclusion	59
	Bibliographie	61
4	Comparison with 7 T Data	63
4.1	Introduction	63
4.2	Materials and Methods	65
4.2.1	Participants	65
4.2.2	Image acquisitions	65
4.2.3	Common image space	65
4.2.4	Targeting methods	66
4.2.5	Quantitative analyses	69
4.2.6	Qualitative analyses	69
4.3	Results	70
4.3.1	Quadrilateral of Guiot	70
4.3.2	Automated 3T dMRI-based segmentation	70
4.3.3	Manual Vim delineation on 7 T SWI	71
4.3.4	Multi-atlas segmentation	71
4.3.5	Subdivision of the VLV cluster	73
4.3.6	Qualitative comparison	73
4.4	Discussion	74
4.5	Conclusion	75
	Bibliographie	77
5	Multi-modal segmentation of the Vim	83
5.1	Introduction	83
5.2	Materials and Methods	84
5.2.1	Dataset	84
5.2.2	Common Image Space	85
5.2.3	Thalamic Parcellation	85
5.2.4	The Proposed Framework	86
5.2.5	Manual delineation of the Vim	89
5.2.6	Multi-atlas segmentation	89
5.2.7	Quantitative comparison	89

5.3 Results	89
5.4 Discussion	92
5.5 Conclusion	93
Bibliographie	97
6 Conclusion and Perspectives	99
Bibliographie	103
A Appendixes	105
A.1 Assessment of Frameless versus Frame-based Registration of Computed Tomography and Magnetic Resonance Imaging in Gamma Knife Surgery Planning . .	105
A.2 Thalamic parcellation	116
A.2.1 Suppelementary material	116
A.2.2 Study extension	117
Bibliographie	119
Curriculum Vitae	121

1

Introduction

1.1 Thalamus

The thalamus is, at the same time, a preeminent brain relay and a substantial regulator of the motor and sensory signals driven by the cortical-subcortical pathways. With its ovoid shape it represents the largest diencephalon entity, and thereupon, it occupies the central brain core. Laterally it is delimited by the posterior part of the internal capsule and medially by the lateral wall of the third ventricle. Following the brain symmetry, each hemisphere includes a thalamus. Both thalami meet at the brain mid-plane. The anatomical position of the thalamus could be closely related to its function [1, 2].

The name of the thalamus originates from the Greek word *thalamos* meaning the "inner chamber" or "storeroom" of ancient Greek or Roman houses. In clear anatomical context it was initially used by Galen, a biomedical scientist that lived in the first century of the current era and remained the most influential one until the beginning of the Renaissance. According to the literature, with the term *thalamos*, Galen was alluding to a brain region in the inferior horn of the lateral ventricle, resembling an inner chamber, which could be seen as *a reservoir of vital spirit* for regeneration and continuity of the optical nerve and therefore, the eye [1, 2]. Similarly, the word thalamus could also take roots from the same Egyptian word *thalamos* meaning antechamber or "a small room leading to the main one" that again in some way illustrates this brain structure [1].

Approximatively, the thalamus occupies 15 cm^3 or, in other words, 1% of the total human brain volume. In average, both its height and width are around 20 mm, while in the rostrocaudal directions it measures about 30 mm. Regarding the number of cells, the estimation of the

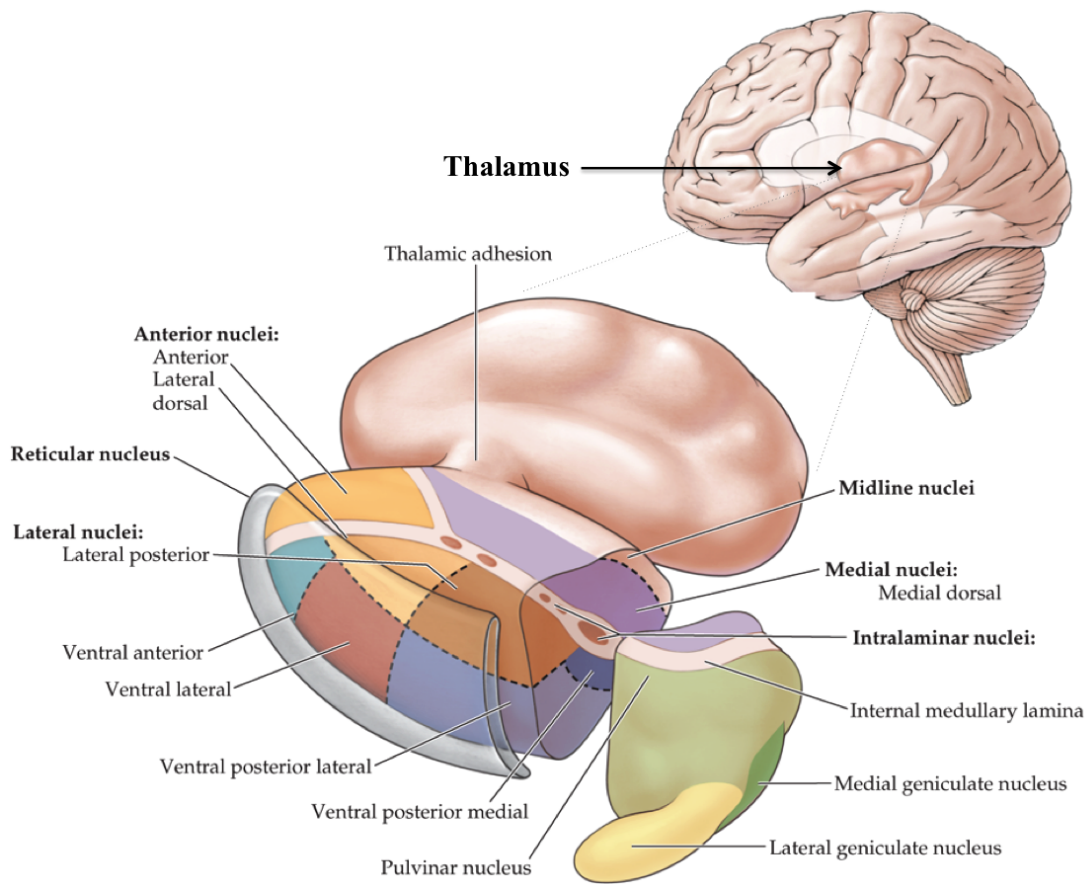


FIGURE 1.1 – Schematic representation of the thalamus, its localization and simplified structure. Adapted from [4]

thalamic neurons goes up to 10 million [2, 3].

The thalamus is characterised by a complex anatomical architecture (see figure 1.1). It is composed of numerous small isolated groups of distinct cells, the thalamic nuclei, differing between them in both anatomical and functional aspect. The pioneer study concerning the thalamic subdivision dates from 1822 by the neuroanatomist Karl Friedrich Burdach indicating only three segments. Through a dissection of post-mortem human brains, Burdach was able to identify, for the first time, the internal medullary lamina that represents a Y-shaped fibres-bundle (see figure 1.1) subdividing the thalamus into its anterior (superior), medial (inner) and lateral (external) part [1]. Since then, the knowledge of the thalamic inner structure has considerably increased, and nowadays more than 50 nuclei are identified [2, 3].

Each nucleus receives a different input and furthermore, sends a particular afferent signal to one or a few specific cortical regions from the same hemisphere via the thalamocortical white-matter pathways [1–3, 5]. In terms of nature of the incoming fibres, there are two groups of thalamic nuclei. The first group represents the nuclei which receive afferents from the ascending pathways before they go to the cortex such as the sensory information, the

basal ganglia's and the cerebellum's output. Consequently, they are called the *first order relays*. Without changing the essence of the incoming signal, the primary role of the first order nuclei is to moderate or, to filter the received signal with the intention to send the "right message" to the respective cortical area. Differently, the other group known as the *second order relays* encloses the nuclei which receive afferents mainly from the cortex and transmit further this information to another cortical area. Hence, they allow and, at the same time, control the communication between different cortical regions and therefore, are indispensable for regulating high-order cortical functions [5–7]. Additionally, both types of relays have, in general, different projections. The first order nuclei transmit principally to the primary cortical regions, while the second order nuclei to the association cortex [5]. Nevertheless, the barrier between both types of nuclei should not be considered in an absolute manner [6].

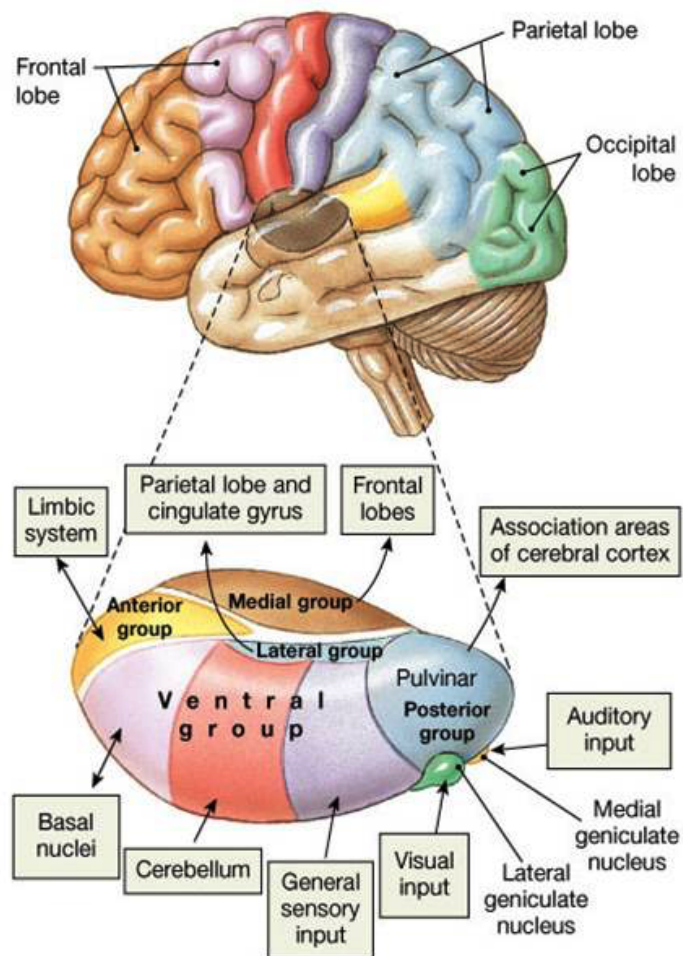


FIGURE 1.2 – Colour-coded representation of the main thalamic connections. Each thalamic subpart is projection towards different brain area. Adapted from [8].

As exception of the well-defined connection patterns previously described, there is a third smaller group of thalamic nuclei that have rather spread diffused cortical projections. They are known as the *non-specific* thalamic nuclei and enclose the inter-laminar nuclei taking part

Chapitre 1. Introduction

of the internal medullary lamina, and the thalamic reticular nucleus (TRN), which represents the thalamic envelope [3].

The TRN, in particular, receives signals from both thalamus and the cortex, but on its turn, it projects only towards the thalamus, i.e. different thalamic nuclei. Moreover, it acts as a major inhibitor system of the thalamic function [6, 9].

The number of nuclei, their nomenclature and extent vary among the investigators and with the criteria used for defining them. The classical delimitation of the nuclei relies on the underlying anatomy seen through the myelo- and the cytoarchitectural inspections of the thalamic histology [10, 11]. The most commonly used atlases, Morel's [12] and Schaltenbrand and Wahren's [13], are representing such subdivision. However, the scientific and technical modernisation, allowing more profound insights and refined details, suggested a much higher complexity of the thalamic structure. Additionally, it changed the perception of the nuclei as a singleton with its proper, well-defined, structure, function and connection [1, 5]. The cells composing one structural thalamic entity are not compulsorily portraying the same function and connection, rather the same type of cells forms a pathway passing through neighbouring anatomically defined nuclei. In that sense, a structural nucleus encloses many separate pathways functionally independent that not necessarily interact with the nucleus itself [5]. Consequently, the thalamic connectivity provides different subdivision pattern [14, 15] (see figure 1.3). Nonetheless, despite the achieved advanced knowledge, many aspects of the thalamus and its relation with the cortex remain still an enigma [3, 5].

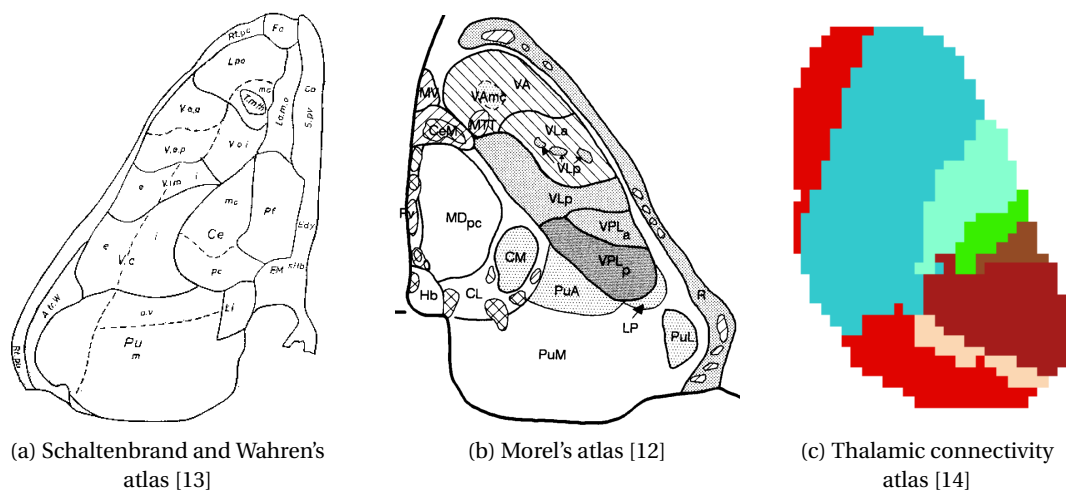


FIGURE 1.3 – Visual comparison between axial slices of the three most commonly used thalamic atlases. One can observe that the atlas build from the thalamic connections (panel (c)) shows different division pattern that the histology (panels (a) and (b)). Nonetheless, a dissimilarity can also be noticed between those based on histology criteria. Morel's atlas, as more recent one, is using calcium-binding proteins for the subdivision, while Schaltenbrand is based on simple myeloarchitectonic survey.

1.1.1 Thalamic function

The initial association of the thalamus with the optic nerve remained the main thalamic interpretation throughout a relatively long period. In the 18th century only, the thalamus started to be seen as a relay of many sensory afferents. In that time, several postmortem studies related the lesions observed solely in the thalamus with the loss of sight, hearing, memory, and sensation of touch, smell and taste. Additionally, some investigations indicated the involvement of the thalamus in the motor control [1, 5].

With the rise of the microscopic anatomical studies, in the second half of last century, the thalamus was further inspected at a synaptic level which revealed more extensively the complex network of thalamocortical and intrathalamic connections and therefore, the thalamic role [1]. Today the thalamus is known as the key brain relay that regulates and modulates all the motor and sensory systems but also cognitive functions such as awareness, consciousness, attention, memory and language [3]. The only exception is the olfactory, i.e. smell afferents that do not pass through the thalamus before reaching the cortex [16].

In that sense, nowadays many neuroscientific studies demonstrated the thalamic involvement in a wide range of functional impairments. For instance, a degeneration or damage of specific thalamic cells or connections could cause a severe chronic pain on the contralateral part of the body [17–20], a partial or complete blindness [21, 22], insomnia [23–25], vestibular disorders [26, 27] and memory loss [28]. Structural changes in the thalamus or in its anatomical subparts has also been related to schizophrenia [29–31], Alzheimer's disease [32–34], epilepsy [35–37], multiple sclerosis [38–40], and movement disorders [41].

We could only agree with M. Guillery and M. Sherman [5] that the thalamus should be rather seen as "deepest layer of the cortex", and furthermore, since the cortex and the thalamus are in a mutual functional dependence, a proper and profound analysis of either one of them should always include the other. Or using the words of M. Sherman : "cerebral cortex without thalamus is rather like a great church organ without an organist : fascinating, but useless" [5].

1.1.2 Clinical target

The ventral thalamic part, acting as a relay in the cerebello-thalamo-cortical pathway, is well known as the motor thalamus [42, 43]. Its primary projections are towards the motor and premotor cortex, the supplementary motor area and the cerebellum. It is also connected to the basal ganglia and substantia nigra [42, 44]. Consequently, it is of crucial importance for the control of movement and thereby, substantial in movement disorders studies [44, 45].

One of the most frequent and, at the same time, most severe movement disorders is the essential tremor (ET) affecting 9% of the worldwide population above 60 years old [43, 46–49]. It is manifesting with a forceful shaking of the arms during voluntary movements that in later stage could spread to other parts of the body causing important physical disabilities [46, 50]. Although the cause and the underlying mechanism of ET is still not fully understood [43, 48,

Chapitre 1. Introduction

49, 51, 52], one specific motor thalamic subpart, the ventral intermediate nucleus (Vim), is of central interest in the related research. As initially described by the neurosurgeon Guiot in 1960s, the cells building the Vim are with neuronal activity bursting almost synchronously with the peripheral tremor and therefore, they are very likely to engender the tremor [51, 53, 54].

The initial therapy for ET involves sedative medication but, unfortunately, one to two-quarters of the patients are becoming resistant to such treatment [46, 50, 55, 56]. As alternative, stereotactic neurosurgical procedures, such as deep brain stimulation (DBS) [46], gamma knife surgery (GKS) [57] and high intensity focussed ultrasound (HIFU) [47], are nowadays applied for treatment of drug-resistant tremor [50, 56]. For all these surgery the Vim is established as a highly effective target for ET arrest [58, 59].

DBS is currently accepted as the *gold standard* neurosurgical treatment of tremor in medically refractory cases, allowing an intraoperative confirmation of the targeting and an immediate post-operative clinical effect [46, 55, 60, 61]. It represents an implantation of electrodes in the previously set target for neuromodulation of its function and, as such, it stands as an invasive treatment enclosing the risks of open surgical procedures [47].

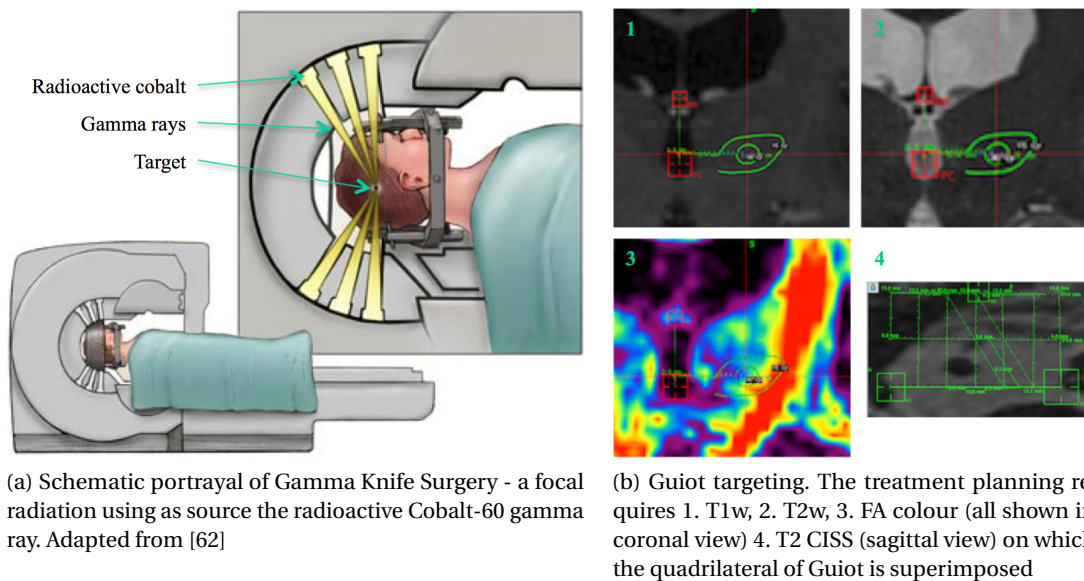


FIGURE 1.4 – Treatment of tremor in Gamma Knife Surgery framework. The main isodose of 90 Gy (internal green round contour shown in (b)1-3) is centred on the Guiot point representing the Vim. As internal capsule (appearing in red on FA colour) should be preserved intact, the marginal isodose of 15 Gy (external green ellipsoidal contour) is adapted accordingly.

Complementary to DBS are HIFU and GKS as minimally invasive approaches since they do not require opening of the skull. HIFU uses 1000 ultrasound rays for generating a focal lesion, which size and location are controlled via MR thermography measuring in real time the temperature of the targeted area [47]. On the other hand, GKS is a focal radiation based on the high-precision convergence of multiple Cobalt-60 gamma rays (see figure 1.4(a)) [63, 64]

allowing the healthy tissue to stay intact. Moreover, in contrast to DBS and HIFU, GKS is lacking in immediate intraoperative confirmation of the target localisation. However, both GKS and HIFU are fully image-guided techniques or, in other words, their targeting relies solely on the information provided by the images acquired for the treatment planning. These acquisitions are principally based on magnetic resonance imaging (MRI).

Unfortunately, current standard MRI protocols used in everyday clinical practice are not able to provide a direct visualisation of the Vim (refer to figures (see figure 1.4(b) and figure 1.5) [43, 59]. Therefore, the targeting is performed in indirect manner by employing methodologies build upon known brain landmarks, such as the anterior commissure (AC) and the posterior commissure (PC) [59].

Since none of the used landmarks is in a well-determined relationship with the underlying thalamic morphology, the currently used indirect targeting approaches are insensitive to the anatomical inter-subject variability [53, 59]. Furthermore, among the centres worldwide there is no consensus regarding the *gold standard* method for targeting the Vim.

In Lausanne University Hospital (CHUV) the Vim targeting for GKS treatment purposes is achieved by employing the quadrilateral of Guiot (see figure 1.4(b)) which is requiring identification of the AC and PC as well as the height of the thalamus on the pre-operative images [53]. The same treatment procedure is also applied in Marseille University Hospital (CHU Timone) in France with which the thesis project was in close collaboration.

To optimally select those landmarks, the GKS treatment planning is involving several MRI modalities : T1-weighted (T1w), T2-weighted, T2-weighted Constructive Interference Steady State (CISS)/Fiesta and diffusion weighted images (DWI) [65]. The role of the DWI is to only ensure intactness of the internal capsule by the applied radiation gradient (see figure 1.4(b)). More details about DWI as a MRI modality will be discussed further bellow. Combining information from all the modalities in an accurate manner demands mainly a voxel-to-voxel matching between the used images. In Appendix A1 we provide an assessment of the accuracy of the standard voxel-based registration used in such framework. The study shows that the committed error for multi-modal registration is less than the voxel-size of the used images. Moreover, it demonstrates that there is no statistically significant difference between the voxel-wise registration and the one based on the stereotactic frame only, which is predominantly used for the Gamma Knife treatment planning.

A precise definition of the target's position is crucial for an optimal clinical outcome [59]. In this context, having a standardised procedure, i.e. an accurate and robust automatic segmentation of the Vim addressing the current limitations, becomes of crucial importance to support the ET treatment planning.

1.2 Magnetic Resonance Imaging of the thalamus

MRI is a noninvasive imaging technique that, in contrast to other clinically used imaging modalities, provides an enhanced characterization of the soft tissue [66]. Additionally, its acquisitions are not involving any ionizing radiation and are able to image a sequence of equidistant slices parallel to any plane of the human body [67]. These advantages led MRI to become an indispensable medical tool for a wide range of noninvasive diagnostic procedures and surgical treatments [66].

However, as previously mentioned, the information available from current clinical MRI protocol is very poor in regards the identification of Vim (figure 1.4(b) and figure 1.5). In fact, due to the great number of its axonal connections in regards its relatively small size, the thalamus appears with highly insufficient intrinsic contrast on standard T1w and T2w images which makes impossible the distinction of any features within [68].

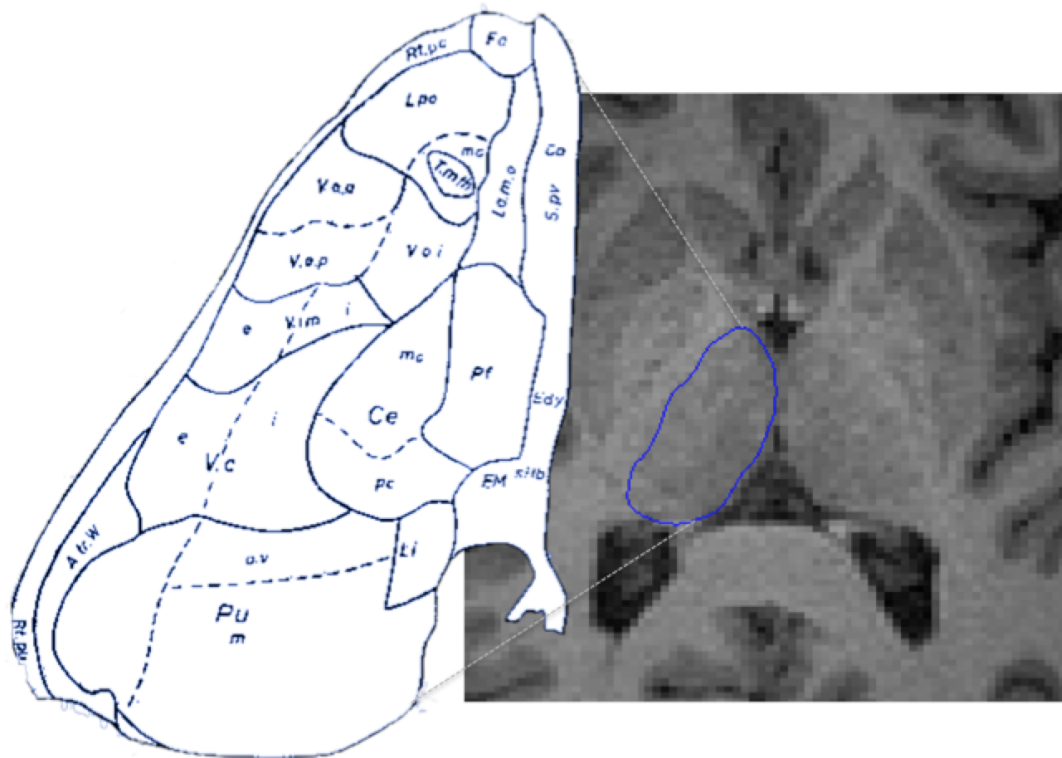


FIGURE 1.5 – Comparison between the thalamus appearing on the T1w images (right panel) with the corresponding axial slice of the Schaltenbrand atlas (left pannel, [13]). The T1w images, as well as the other current standard modalities, could not provide enough intrinsic contrast for distinguishing the thalamic subparts. The thalamus on them is appearing as a homogeneous region.

One possible image-based alternative could be the use of digital atlases. Nevertheless, such methodology also presents various limitations. Primarily, there are very few thalamic at-

lases [12, 13, 69] which, in addition, are built from a few species only. Hence, they are highly limited at including the inter-individual thalamic variations which are not homogeneous [12]. Moreover, due to the low intrinsic contrast inside the thalamus, a classical registration between the subject's image and the atlas template could also lead to an inaccurate matching of the thalamic structures.

The conversion of the atlases into digital format is also facing several challenges mainly engendered from the relatively low resolution of their slices together with the variable inter-slice distance as well as the complex thalamic architecture difficult to accurately capture on such slice-scale [70]. Another drawback comes from the inconsistency between the outlines of different atlases and their nomenclature. For instance, the neurosurgeons and the anatomists utilize mainly the atlas of Schaltenbrand and Wahren [13] built upon a postmortem myeloarchitectonic inspection and existing only in a paper book format. Morel's atlas [12] gives the histology revealed by calcium-binding proteins is further digitalised and therefore, most commonly used. Both atlases are based on different terminology and therefore, a correspondence between them is difficult to achieve [70] (figure 1.3).

Recent advancement in the field of MRI technologies provides, however, a highly promising potential for a more precise resolution of the thalamic subparts based solely on the proper subject anatomy [70] and, as such, they should further be explored.

1.2.1 Diffusion Weighted Imaging

In unhindered homogeneous medium, a molecule moves freely in random direction due to the thermal energy that is carrying [71]. In other words, it follows an isotropic diffusion that is also known as Brownian motion [72, 73]. However, in a heterogeneous milieu where there are different barriers or obstacles, the diffusion of the molecule becomes more restricted. For instance, the white matter of the brain is composed of densely distributed axons forming coherently aligned fibres that transmit the signals to the cortex [71]. As consequence, the water molecules inside the brain, representing 73% of its total volume [74], are mainly constrained in diffusion parallel to the direction of the axonal pathways, while motions perpendicular to it are hindered. Hence, in such structured tissue there is an anisotropic diffusion [71, 75].

Initially introduced in the middle of the 1980s, the diffusion-weighted MR images (DWI) nowadays evolved into a remarkably powerful tool for an unique and profound analysis of the underlying microstructure of the human body. While capturing the preferred diffusion orientation of the water molecules' natural displacement inside a structured tissue, the DWI reveals the architecture of that tissue in a noninvasive manner [75, 76]. The fundamentals of its acquisition rely on introducing a spatially varying magnetic field with pairs of encoded gradient pulses that engender phase difference between the moving water molecules causing loss of signal in the direction of the applied gradient. In other words, it only measures the displacement occurred in the imposed gradient axis [76].

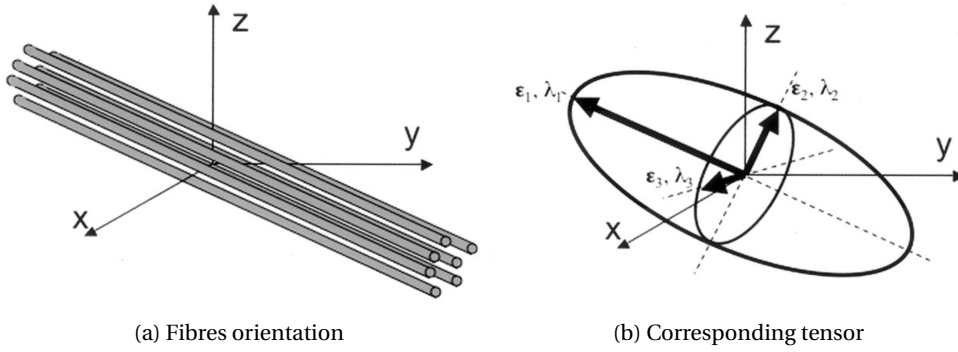


FIGURE 1.6 – Tensor representation of the diffusion orientation within a voxel. In (b) the vectors ϵ_1 , ϵ_2 and ϵ_3 are the eigenvectors of the fitted tensor, while λ_1 , λ_2 and λ_3 its eigenvalues. The eigenvector ϵ_1 corresponding to the biggest eigenvalue (λ_1) is parallel to the main direction of the fibres. Adapted from [80]

Knowing that the axonal diameter is between 0.1 to 20 μm [77], DWI could be seen as a quantitative method that reveals, within a voxel, the average properties of the water diffusion happening at microscopic level [75, 76].

The simplest invariant model describing the diffusion profile in a voxel scale is the Diffusion Tensor (DT) modelling introduced in 1994 [78]. While assuming that the diffusion process of the water molecules follows a Gaussian distribution, this model uses an ellipsoid representation to express the level of anisotropy (figure 1.6). The ellipsoid is defined by a 3x3 symmetric and semi-positive matrix expressing the diffusion variation along the different axis. Therefore, it requires six degrees of freedom or, in terms of acquisition, at least six non-collinear encoded gradient directions [71, 75, 79].

The eigendecomposition of the tensor depicts the shape of the fitted ellipsoid : the eigenvectors are representing its principle directions, while the eigenvalues are giving the maximum radius in each plane (figure 1.6(b)). Hence, for an isotropic diffusion the shape of the ellipsoid is mainly spherical, while for a highly anisotropic milieu it tends towards the form of a slender cylinder [71]. Furthermore, the eigenvector corresponding to the biggest eigenvalue is presumed to be parallel to the respective fibre direction.

The DT eigenvalues are also used to derive scalar maps characterizing the diffusion. One example is the fractional anisotropy (FA) map that quantifies the degree of anisotropy at each voxel [81] :

$$FA = \frac{\sqrt{(\lambda_1 - \lambda_2)^2 + (\lambda_2 - \lambda_3)^2 + (\lambda_3 - \lambda_1)^2}}{\sqrt{2(\lambda_1^2 + \lambda_2^2 + \lambda_3^2)}} \quad (1.1)$$

where λ_1 , λ_2 and λ_3 are the three eigenvalues respectively.

FA takes values in the range between 0 and 1. From its definition, we could see that low FA values correspond to voxels with isotropic diffusion, while the high ones to anisotropic diffusion.

As first diffusion MRI modelling, DT has been widely used as a quantitative tool for many neurodegenerative and neurodevelopmental studies such as the cerebrovascular diseases, multiple sclerosis, schizophrenia and brain tumours [75]. However, being a Gaussian modelling, it is rather too simplistic for an accurate portraying of the complex diffusion process. DT is adequate for describing the orientation of a single fibre population. Among the voxels that could be imaged in the brain via DWI, one to two-thirds incorporates a crossing between the white matter fibres [82] for which DTI will fail to fit accurately the respective signal [75, 83] (refer to figure 1.7).

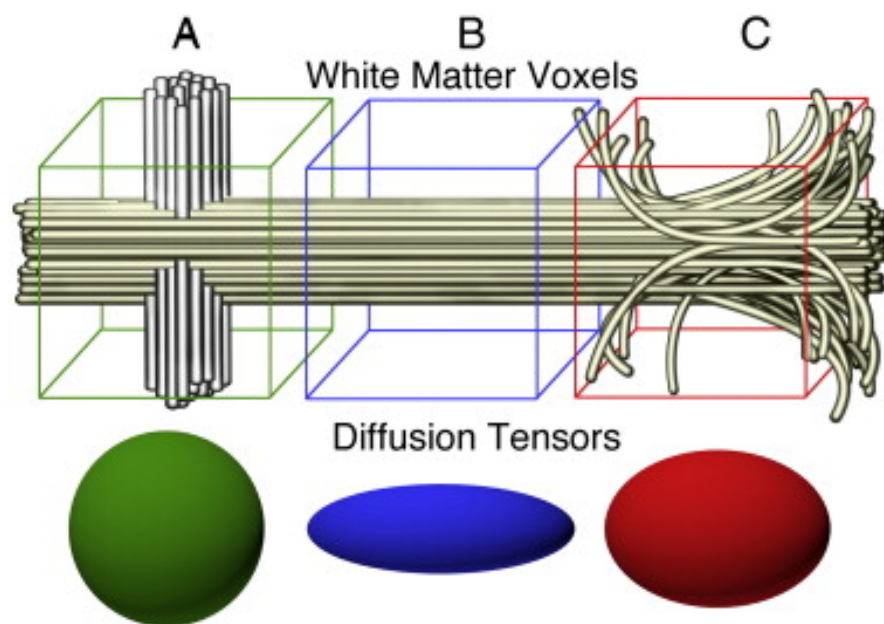


FIGURE 1.7 – Illustration of the DTI limitation for different fiber populations. While it can well model an anisotropic diffusion population (B), it fails to portrait the cases of fibre crossings (A) and fibre bending (C). Taken from [84].

Several methods have been proposed to address this limitation and, with the introduction of the acquisition scheme providing high angular resolution diffusion imaging (HARDI), more suitable model emerged [85]. HARDI relies on a large number of uniformly distributed gradient directions for the DWI acquisition which provides more refined details of the underlying local diffusion orientation [75, 85].

One of the most widely used model-free HARDI approaches is the Q-Ball Imaging (QBI) [83] that is able to characterise the full angular profile of probability density function of water molecules' diffusion displacement. This angular estimation is also known as the diffusion orientation distribution function (ODF), and it represents a spherical function whose maximum radius, at each voxel, is parallel to the intrinsic fibre orientation [75, 86].

Chapitre 1. Introduction

Diffusion ODF, or further referred as ODF only, can be estimated directly with the Funk-Random transform (FRT) [83]. Each point of the obtained spherical function, while corresponding to a unique direction, represents the great circle integral of the signal on the sphere delimited by the perpendicular plane passing through the chosen point [75, 86].

Taking advantage of the Spherical Harmonics (SH) representation, Descoteaux proposed an analytical solution of the QBI signal that is fast, robust to noise and flexible in acquisition parameters [86]. The SH basis can be represented as follows :

$$Y_l^m(\theta, \phi) = \sqrt{\frac{(2l+1)(l-m)!}{4\pi(l+m)!}} P_l^m(\cos(\theta)) e^{im\phi} \quad (1.2)$$

where $\theta \in [0, \pi]$, $\phi \in [0, 2\pi]$, P_l^m is an associated Legendre polynomial, l the order and m the phase factor [86].

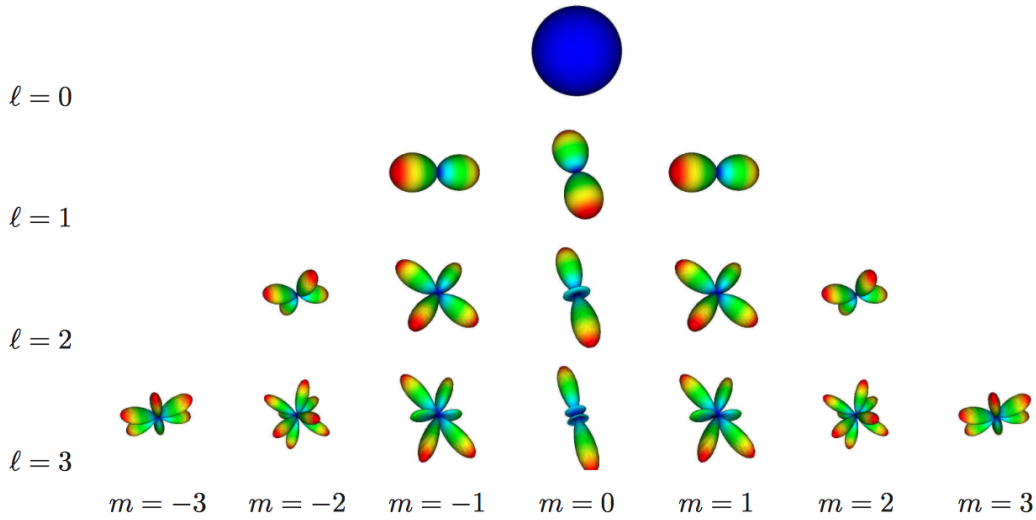


FIGURE 1.8 – Illustration of the squared real part of the SH basis up to order 3, where the colours from blue to red are representing the value incremental from minimum to maximum respectively. Taken from [87].

To solve the FRT function in such framework, the SH basis was modified into symmetrical, real and orthonormal :

$$Y_j = \begin{cases} \sqrt{2} \operatorname{Re}(Y_k^m), & \text{if } -k \leq m < 0 \\ Y_k^0, & \text{if } m=0 \\ \sqrt{2} \operatorname{Im}(Y_k^m), & \text{if } 0 < m \leq k \end{cases} \quad (1.3)$$

for $k = 0, 2, 4, \dots, l$ and m taking values between $-k, \dots, 0, \dots, k$ and $j = j(k, m) = (k^2 + k + 2)/2 + m$.

Hence, having c_j as the SH coefficient describing the HARDI signal, the ODF could be estimated as :

$$\Psi(\theta, \phi) = \sum_{j=1}^{(l+1)(l+2)/2} 2\pi P_{l(j)}(0) c_j Y_j(\theta, \phi) \quad (1.4)$$

Subsequently, Descoteaux provides a vectorial representation of the diffusion signal which is easily explorable and, in this thesis, it would be of central interest for the delimitation of the thalamic subparts.

1.2.2 Susceptibility Weighted Imaging

Susceptibility-weighted imaging (SWI) is an MRI technique that generates a unique image contrast relying on tissue sensitivity to magnetic susceptibility effects [88–90]. The magnetic susceptibility, in a general sense, describes the degree of magnetisation in an object resulting from an external field [91]. Moreover, the variations of local magnetic properties engendered from a slight field perturbations cause susceptibility contrast appearing inside the scanned biological tissue [91].

In the framework of standard gradient echo imaging, SWI is built as a combination of the MRI signal's magnitude and phase, both of them strongly affected by the magnetic susceptibility and the tissue geometry. More precisely, the magnitude information is derived from the differences in effective transverse signal relaxation (T2* effect), while the phase-shifting is occurring, for sufficiently long echo times, as a result of magnetic susceptibilities differences between the neighbouring tissues [88, 89].

Several tissues, such as the de-oxygenated blood vessels, the axonal lesions, the air/tissue interfaces, as well as the calcium and iron-laden tissue, manifest a unique magnetic susceptibility differences with respect to their surroundings [88, 90, 91]. Accordingly, for these tissues, SWI provides a more enhanced contrast than the standard T1, T2 or T2*-weighted imaging [88].

The susceptibility-based contrast imaging of the brain started towards the end of the 1980s employing 1.5 T machines and, despite the low resolution and the poor sensitivity to the field perturbation, they were however able to reveal some brain pathologies such as stroke, trauma and tumours [91]. Today, higher magnetic field strength, like 7 T for instance, allows an improved spatial resolution, considerably increased signal to noise ratio (SNR) as well as a superior sensitivity to magnetic susceptibility engendered contrast [91]. Hence, along with the MRI advancements, SWI has gained an expanded popularity in brain-pathology studies mainly related to vascular diseases, but also brain degeneration and malfunction [88, 90–92]. Additionally, it also provides better visualization of the deep brain structures [93].

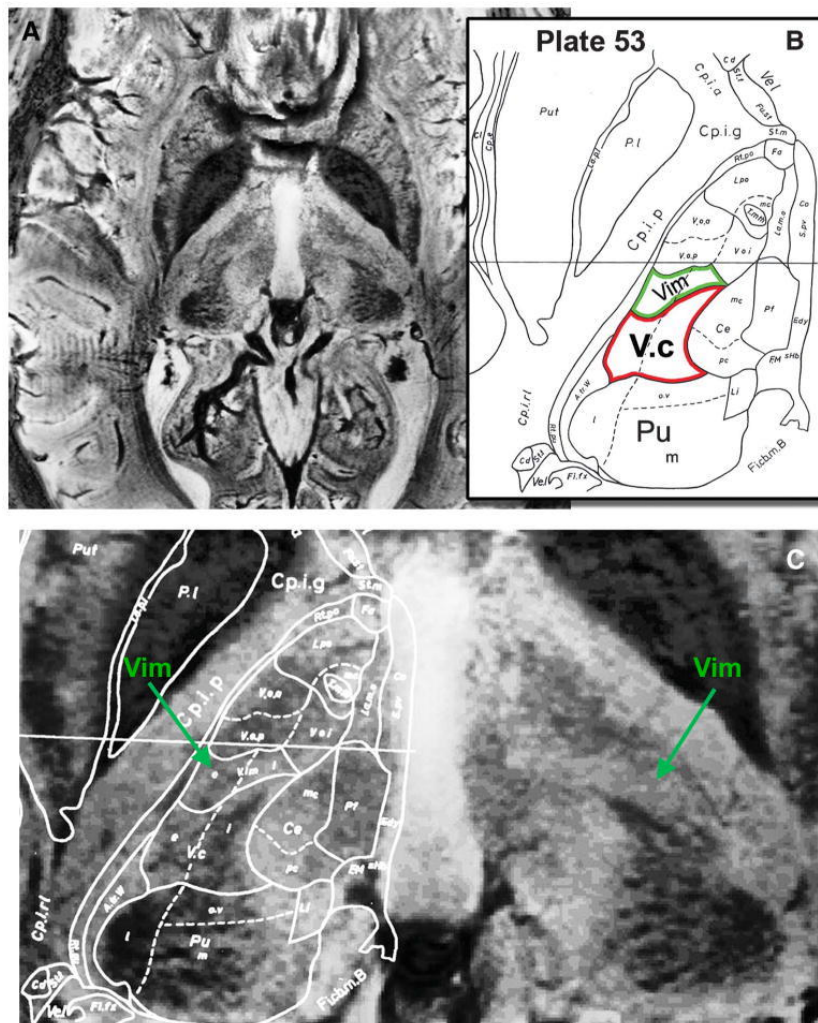


FIGURE 1.9 – Thalamic structures seen on 7T SWI (panels A and C) in comparison with the Schaltenbrand atlas (panels B and C). Adapted from [93]

Although oriented more to basal ganglia, the study of Abosch et al. [93] introduced the first evidence for *in vivo* identification of the thalamic nuclei on SWI acquired at 7 T. On those images, the thalamus is no longer appearing as a homogeneous region but with numerous internal contrast modulations. A comparison between the observed thalamic features and the histological parcellation given by Schaltenbrand and Wahren's atlas indicate the shape and localization-based differentiation of the Pulvinar, the medio-dorsal part and several ventral nuclei including the Vim. Particularly, the Vim appears as a well-distinguishable hyperintensity structure surrounded by darker regions (see figure 1.9).

The presented observation have a qualitative character and were made based on data from a single subject. But, at the same time, they introduce a new mean of vital importance for an unbiased and direct discrimination of the complex thalamic architecture.

1.3 Thesis goals and outline

The central objective of this thesis is to develop an automated segmentation of the anatomical thalamic subparts based on multi-modal MRI information from both 3 and 7 T. Through such parcellation, the primary goal is to provide an improved and more standardised 3D targeting of the Vim for the surgical treatment of drug-resistant tremor. Additionally, knowing the role of the thalamus and its involvement in many neurological diseases, an automated outline of all the other nuclei would be beneficial, beyond targeting, in a wide range of clinical studies and applications.

Chapter 2 presents the automated framework I developed for **segmentation of seven thalamic regions**, each of them enclosing anatomically different group of nuclei. One of the segmented group is the motor-related nuclei including the Vim. The segmentation is based on both spatial position and local diffusion properties from 3 T DWI, expressed by the **ODF coefficients in the SH basis** to explore the full angular characterisation of the complex diffusion process inside the thalamus. The method was tested and evaluated on a dataset of 35 healthy subject which showed its **robustness** and the **anatomical meaning** of the outlined subparts regarding the Morel's atlas. In additional scan-rescan dataset of 8 subject, the **reproducibility** of the method was also demonstrated. Furthermore, the proposed approach outperforms the state-of-the-art in reproducibility and matching the anatomy presented by Morel.

Chapter 3 covers the **application of the developed segmentation method** in clinical cases or, more precisely, 65 **drug-resistant tremor patients** treated with GKS. The available follow-up data from one-third of the cohort allowed **validation of the segmented motor group of nuclei** with respect the radiologically observable contrast enhancement corresponding to the surgical target. Moreover, exploring again the ODF coefficients in SH basis, a **sub-segmentation of the motor-nuclei cluster allowed a more narrowed localization of the targeted Vim**. These findings were confirmed in 2 additional ET patient that were treated with DBS.

Chapter 4 presents a **comparison between four methods that define the Vim** : the targeting with the quadrilateral of Guiot, the 3T diffusion-based segmentation of the motor nuclei, the manual delineation on the 7T SWI and the multi-atlas delineation employing the SWI features for a more accurate thalamic matching. Although done on a small dataset from healthy subjects, this analysis imply **better discrimination of the Guiot points and the manually outlined Vim-area inside the automatically segmented motor group of nuclei**. Moreover, the Vim outline provided by the SWI-based atlas matches closely the manual delineation.

Chapter 5 shows the **combination of both 3T DWI and 7T SWI information for an automated segmentation of the Vim nuclei**. The proposed framework was tested on a dataset including young and elderly subjects for which the SWI contrast and the distinguishable regions appear differently. Lacking a *ground truth*, the outcome was compared to the respective manual delineation showing the potential of the proposed framework to detect the Vim area.

Chapter 6 concludes this thesis and discusses about the possible future extensions.

Bibliographie

- [1] E. G. Jones, *The Thalamus*, Springer, 1985.
- [2] C. M. Elder, J. L. Vitek, *The Motor Thalamus : Alteration of Neuronal Activity in the Parkinsonian State*, in : *Basal Ganglia and Thalamus in Health and Movement Disorders*, Springer, Boston, MA, 2001, pp. 257–265.
- [3] M.-T. Herrero, C. Barcia, J. M. Navarro, *Functional anatomy of thalamus and basal ganglia*, *Childs Nerv Syst* 18 (8) (2002) 386–404.
- [4] John Martin, *Neuroanatomy Text and Atlas, Fourth Edition*, McGraw-Hill Medical, 2012.
- [5] R. W. Guillery, S. M. Sherman, *Exploring the Thalamus and Its Role in Cortical Function*, *The Quarterly Review of Biology* 82 (2) (2007) 176–177.
- [6] R. W. Guillery, *Anatomical evidence concerning the role of the thalamus in corticocortical communication : a brief review.*, *J Anat* 187 (Pt 3) (1995) 583–592.
- [7] J. O’Muircheartaigh, S. S. Keller, G. J. Barker, M. P. Richardson, *White Matter Connectivity of the Thalamus Delineates the Functional Architecture of Competing Thalamocortical Systems*, *Cereb Cortex* 25 (11) (2015) 4477–4489.
- [8] Austin Community College. *Associate degree nursing physiology review* [online, cited 20.11.2017].
- [9] M. M. Halassa, *AL, Thalamic inhibition : diverse sources, diverse scales*, *Trends Neurosci* 39 (10) (2016) 680–693.
- [10] R. Hassler, *[Anatomy of the thalamus]*, *Arch Psychiatr Nervenkr Z Gesamte Neurol Psychiatr* 184 (3-4) (1950) 249–256.
- [11] T. Hirai, E. G. Jones, *A new parcellation of the human thalamus on the basis of histochemical staining*, *Brain Res. Brain Res. Rev.* 14 (1) (1989) 1–34.
- [12] A. Morel, M. Magnin, D. Jeanmonod, *Multiarchitectonic and stereotactic atlas of the human thalamus*, *J. Comp. Neurol.* 387 (4) (1997) 588–630.
- [13] G. Schaltenbrand, W. Wahren, *Atlas for Stereotaxy of the Human Brain*, Thieme, 1977.
- [14] T. E. J. Behrens, H. Johansen-Berg, M. W. Woolrich, S. M. Smith, C. a. M. Wheeler-Kingshott, P. A. Boulby, G. J. Barker, E. L. Sillery, K. Sheehan, O. Ciccarelli, A. J. Thompson, J. M. Brady, P. M. Matthews, *Non-invasive mapping of connections between human thalamus and cortex using diffusion imaging*, *Nature Neuroscience* 6 (7) (2003) 750–757.

Bibliography

- [15] J. O'Muircheartaigh, C. Vollmar, C. Traynor, G. J. Barker, V. Kumari, M. R. Symms, P. Thompson, J. S. Duncan, M. J. Koepp, M. P. Richardson, Clustering probabilistic tractograms using independent component analysis applied to the thalamus, *NeuroImage* 54 (3) (2011) 2020–2032.
- [16] S. M. Sherman, Thalamic relays and cortical functioning, *Prog. Brain Res.* 149 (2005) 107–126.
- [17] C. B. Ab Aziz, A. H. Ahmad, The Role of the Thalamus in Modulating Pain, *The Malaysian Journal of Medical Sciences : MJMS* 13 (2) (2006) 11–18.
- [18] S. M. Gustin, C. C. Peck, S. L. Wilcox, P. G. Nash, G. M. Murray, L. A. Henderson, Different pain, different brain : thalamic anatomy in neuropathic and non-neuropathic chronic pain syndromes, *The Journal of Neuroscience : The Official Journal of the Society for Neuroscience* 31 (16) (2011) 5956–5964.
- [19] L. A. Henderson, C. C. Peck, E. T. Petersen, C. D. Rae, A. M. Youssef, J. M. Reeves, S. L. Wilcox, R. Akhter, G. M. Murray, S. M. Gustin, Chronic pain : lost inhibition ?, *The Journal of Neuroscience : The Official Journal of the Society for Neuroscience* 33 (17) (2013) 7574–7582.
- [20] C.-T. Yen, P.-L. Lu, Thalamus and pain, *Acta Anaesthesiologica Taiwanica : Official Journal of the Taiwan Society of Anesthesiologists* 51 (2) (2013) 73–80.
- [21] G. S. L. Coullon, F. Jiang, I. Fine, K. E. Watkins, H. Bridge, Subcortical functional reorganization due to early blindness, *Journal of Neurophysiology* 113 (7) (2015) 2889–2899.
- [22] N. H. Reisle, T. B. Dyrby, H. R. Siebner, H. Lundell, M. Ptito, R. Kupers, Thalamocortical Connectivity and Microstructural Changes in Congenital and Late Blindness, *Neural Plasticity* 2017 (2017) 9807512.
- [23] P. Montagna, Fatal familial insomnia and the role of the thalamus in sleep regulation, *Handbook of Clinical Neurology* 99 (2011) 981–996.
- [24] C.-H. Liu, C.-Z. Liu, J. Zhang, Z. Yuan, L.-R. Tang, C.-L. Tie, J. Fan, Q.-Q. Liu, Reduced spontaneous neuronal activity in the insular cortex and thalamus in healthy adults with insomnia symptoms, *Brain Research* 1648 (2016) 317–324.
- [25] D. L. Koo, J.-H. Shin, J.-S. Lim, J.-K. Seong, E. Y. Joo, Changes in subcortical shape and cognitive function in patients with chronic insomnia, *Sleep Medicine* 35 (2017) 23–26.
- [26] M. Dieterich, T. Brandt, Functional brain imaging of peripheral and central vestibular disorders, *Brain : A Journal of Neurology* 131 (2008) 2538–2552.
- [27] B. Baier, J. Conrad, T. Stephan, V. Kirsch, T. Vogt, J. Wilting, W. Muller-Forell, M. Dieterich, Vestibular thalamus : Two distinct graviceptive pathways, *Neurology* 86 (2) (2016) 134–140.

- [28] G. A. Carlesimo, M. G. Lombardi, C. Caltagirone, Vascular thalamic amnesia : a reappraisal, *Neuropsychologia* 49 (5) (2011) 777–789.
- [29] R. Alelú-Paz, J. Giménez-Amaya, The mediodorsal thalamic nucleus and schizophrenia, *Journal of Psychiatry & Neuroscience : JPN* 33 (6) (2008) 489–498.
- [30] M. J. Smith, L. Wang, W. Cronenwett, D. Mamah, D. M. Barch, J. G. Csernansky, Thalamic morphology in schizophrenia and schizoaffective disorder, *Journal of Psychiatric Research* 45 (3) (2011) 378–385.
- [31] G. Pergola, P. Selvaggi, S. Trizio, A. Bertolino, G. Blasi, The role of the thalamus in schizophrenia from a neuroimaging perspective, *Neuroscience and Biobehavioral Reviews* 54 (2015) 57–75.
- [32] B. Zhou, Y. Liu, Z. Zhang, N. An, H. Yao, P. Wang, L. Wang, X. Zhang, T. Jiang, Impaired functional connectivity of the thalamus in Alzheimer's disease and mild cognitive impairment : a resting-state fMRI study, *Current Alzheimer Research* 10 (7) (2013) 754–766.
- [33] N. S. Ryan, S. Keihaninejad, T. J. Shakespeare, M. Lehmann, S. J. Crutch, I. B. Malone, J. S. Thornton, L. Mancini, H. Hyare, T. Yousry, G. R. Ridgway, H. Zhang, M. Modat, D. C. Alexander, M. N. Rossor, S. Ourselin, N. C. Fox, Magnetic resonance imaging evidence for presymptomatic change in thalamus and caudate in familial Alzheimer's disease, *Brain : A Journal of Neurology* 136 (Pt 5) (2013) 1399–1414.
- [34] H. Cho, J.-H. Kim, C. Kim, B. S. Ye, H. J. Kim, C. W. Yoon, Y. Noh, G. H. Kim, Y. J. Kim, J.-H. Kim, C.-H. Kim, S. J. Kang, J. Chin, S. T. Kim, K.-H. Lee, D. L. Na, J.-K. Seong, S. W. Seo, Shape changes of the basal ganglia and thalamus in Alzheimer's disease : a three-year longitudinal study, *Journal of Alzheimer's disease : JAD* 40 (2) (2014) 285–295.
- [35] W. Huang, G. Lu, Z. Zhang, Y. Zhong, Z. Wang, C. Yuan, Q. Jiao, Z. Qian, Q. Tan, G. Chen, Z. Zhang, Y. Liu, Gray-matter volume reduction in the thalamus and frontal lobe in epileptic patients with generalized tonic-clonic seizures, *Journal of Neuroradiology. Journal De Neuroradiologie* 38 (5) (2011) 298–303.
- [36] J. B. Kim, S.-I. Suh, W.-K. Seo, K. Oh, S.-B. Koh, J. H. Kim, Altered thalamocortical functional connectivity in idiopathic generalized epilepsy, *Epilepsia* 55 (4) (2014) 592–600.
- [37] X.-M. Chen, D.-H. Huang, Z.-R. Chen, W. Ye, Z.-X. Lv, J.-O. Zheng, Temporal lobe epilepsy : decreased thalamic resting-state functional connectivity and their relationships with alertness performance, *Epilepsy & Behavior* 44 (2015) 47–54.
- [38] M. M. Schoonheim, H. E. Hulst, R. B. Brandt, M. Strik, A. M. Wink, B. M. J. Uitdehaag, F. Barkhof, J. J. G. Geurts, Thalamus structure and function determine severity of cognitive impairment in multiple sclerosis, *Neurology* 84 (8) (2015) 776–783.
- [39] Y. Liu, P. Liang, Y. Duan, J. Huang, Z. Ren, X. Jia, H. Dong, J. Ye, F.-D. Shi, H. Butzkueven, K. Li, Altered thalamic functional connectivity in multiple sclerosis, *European Journal of Radiology* 84 (4) (2015) 703–708.

Bibliography

- [40] A. d'Ambrosio, M. Hidalgo de la Cruz, P. Valsasina, E. Pagani, B. Colombo, M. Rodegher, G. Comi, M. Filippi, M. A. Rocca, Structural connectivity-defined thalamic subregions have different functional connectivity abnormalities in multiple sclerosis patients : Implications for clinical correlations, *Human Brain Mapping*.
- [41] C. Ohye, T. Shibasaki, Behavior of Thalamic Neurons in the Movement Disorders - Tremor and Dystonia, in : *Basal Ganglia and Thalamus in Health and Movement Disorders*, Springer, Boston, MA, 2001, pp. 285–292.
- [42] C. Hamani, J. O. Dostrovsky, A. M. Lozano, The Motor Thalamus in Neurosurgery, *Neurosurgery* 58 (1) (2006) 146–158.
- [43] S. Sharifi, A. J. Nederveen, J. Booij, A.-E. van Rootselaar, Neuroimaging essentials in essential tremor : a systematic review, *NeuroImage. Clinical* 5 (2014) 217–231.
- [44] C. Bosch-Bouju, B. I. Hyland, L. C. Parr-Brownlie, Motor thalamus integration of cortical, cerebellar and basal ganglia information : implications for normal and parkinsonian conditions, *Frontiers in Computational Neuroscience* 7.
- [45] K. Yamada, K. Akazawa, S. Yuen, M. Goto, S. Matsushima, A. Takahata, M. Nakagawa, K. Mineura, T. Nishimura, MR imaging of ventral thalamic nuclei, *AJNR. American journal of neuroradiology* 31 (4) (2010) 732–735.
- [46] E. D. Flora, C. L. Perera, A. L. Cameron, G. J. Maddern, Deep brain stimulation for essential tremor : a systematic review, *Movement Disorders : Official Journal of the Movement Disorder Society* 25 (11) (2010) 1550–1559.
- [47] N. Lipsman, M. L. Schwartz, Y. Huang, L. Lee, T. Sankar, M. Chapman, K. Hynynen, A. M. Lozano, MR-guided focused ultrasound thalamotomy for essential tremor : a proof-of-concept study, *The Lancet. Neurology* 12 (5) (2013) 462–468.
- [48] H. Cagnan, S. Little, T. Foltynie, P. Limousin, L. Zrinzo, M. Hariz, B. Cheeran, J. Fitzgerald, A. L. Green, T. Aziz, P. Brown, The nature of tremor circuits in parkinsonian and essential tremor, *Brain* 137 (12) (2014) 3223–3234.
- [49] M. Rohani, A. Fasano, Focused Ultrasound for Essential Tremor : Review of the Evidence and Discussion of Current Hurdles, *Tremor and Other Hyperkinetic Movements* 7.
- [50] F. Sammartino, V. Krishna, N. K. K. King, A. M. Lozano, M. L. Schwartz, Y. Huang, M. Hodaie, Tractography-based Ventral Intermediate Nucleus Targeting : Novel Methodology and Intraoperative Validation, *Movement Disorders* 31 (8) (2016) 1217–1225.
- [51] S. E. Hua, F. A. Lenz, Posture-related oscillations in human cerebellar thalamus in essential tremor are enabled by voluntary motor circuits, *Journal of Neurophysiology* 93 (1) (2005) 117–127.
- [52] M. Hallett, Tremor : pathophysiology, *Parkinsonism & Related Disorders* 20 Suppl 1 (2014) S118–122.

- [53] G. Guiot, J. Hardy, D. Albe-Fessard, G. Arfel, G. Vourc'h, E. Hertzog, P. Aleonard, Délimitation précise des structures sous-corticales et identification de noyaux thalamiques chez l'homme par l'électrophysiologie stéréotaxique, *Neurochirurgia* 5 (01) (1962) 1–18.
- [54] J. A. Brodkey, R. R. Tasker, C. Hamani, M. P. McAndrews, J. O. Dostrovsky, A. M. Lozano, Tremor cells in the human thalamus : differences among neurological disorders, *Journal of Neurosurgery* 101 (1) (2004) 43–47.
- [55] W. C. Koller, P. R. Pahwa, K. E. Lyons, S. B. Wilkinson, Deep brain stimulation of the Vim nucleus of the thalamus for the treatment of tremor, *Neurology* 55 (12 Suppl 6) (2000) S29–33.
- [56] E. Bardinet, H. Belaid, D. Grabli, M.-L. Welter, S. F. Vidal, D. Galanaud, S. Derrey, D. Dormont, P. Cornu, J. Yelnik, C. Karachi, Thalamic stimulation for tremor : can target determination be improved ?, *Movement Disorders : Official Journal of the Movement Disorder Society* 26 (2) (2011) 307–312.
- [57] D. Kondziolka, J. G. Ong, J. Y. K. Lee, R. Y. Moore, J. C. Flickinger, L. D. Lunsford, Gamma Knife thalamotomy for essential tremor, *Journal of Neurosurgery* 108 (1) (2008) 111–117.
- [58] A. M. Lozano, Vim thalamic stimulation for tremor, *Archives of Medical Research* 31 (3) (2000) 266–269.
- [59] N. K. K. King, V. Krishna, F. Sammartino, A. Bari, G. D. Reddy, M. Hodaie, S. K. Kalia, A. Fasano, R. P. Munhoz, A. M. Lozano, C. Hamani, Anatomic Targeting of the Optimal Location for Thalamic Deep Brain Stimulation in Patients with Essential Tremor, *World Neurosurgery* 107 (2017) 168–174.
- [60] Y. Sadeghi, E. Pralong, J.-F. Knebel, F. Vingerhoets, C. Pollo, M. Levivier, J. Bloch, Bilateral Deep Brain Stimulation : The Placement of the Second Electrode Is Not Necessarily Less Accurate Than That of the First One, *Stereotactic and Functional Neurosurgery* 93 (3) (2015) 160–167.
- [61] T. M. Herrington, J. J. Cheng, E. N. Eskandar, Mechanisms of deep brain stimulation, *Journal of Neurophysiology* 115 (1) (2016) 19–38.
- [62] Mayo Foundation for Medical Education and Research. Gamma knife targeting [online, cited 20.11.2017].
- [63] M. Levivier, T. Gevaert, L. Negretti, Gamma Knife, CyberKnife, TomoTherapy : gadgets or useful tools ?, *Current Opinion in Neurology* 24 (6) (2011) 616–625.
- [64] T. Witjas, R. Carron, P. Krack, A. Eusebio, M. Vaugoyeau, M. I. Hariz, J.-P. Azulay, J. Regis, A prospective single-blind study of Gamma Knife thalamotomy for tremor, *Neurology* 85 (18) (2015) 1562–1568.

Bibliography

- [65] C. Ohye, Y. Higuchi, T. Shibazaki, T. Hashimoto, T. Koyama, T. Hirai, S. Matsuda, T. Serizawa, T. Hori, M. Hayashi, T. Ochiai, H. Samura, K. Yamashiro, Gamma knife thalamotomy for Parkinson disease and essential tremor : a prospective multicenter study, *Neurosurgery* 70 (3) (2012) 526–536.
- [66] D. Nam, R. L. Barrack, H. G. Potter, What Are the Advantages and Disadvantages of Imaging Modalities to Diagnose Wear-related Corrosion Problems?, *Clinical Orthopaedics and Related Research* 472 (12) (2014) 3665–3673.
- [67] W. Oldendorf, W. Oldendorf, Advantages and Disadvantages of MRI, in : *Basics of Magnetic Resonance Imaging*, Topics in Neurology, Springer, Boston, MA, 1988, pp. 125–138.
- [68] L. Jonasson, P. Hagmann, C. Pollo, X. Bresson, C. Richero Wilson, R. Meuli, J.-P. Thiran, A level set method for segmentation of the thalamus and its nuclei in DT-MRI, *Signal Processing* 87 (2) (2007) 309–321.
- [69] J. Mai, M. Majtanik, G. Paxinos, *Atlas of the Human Brain*, 4th Edition, Academic Press, 2016.
- [70] A. F. Sadikot, M. M. Chakravarty, G. Bertrand, V. V. Rymar, F. Al-Subaie, D. L. Collins, Creation of Computerized 3d MRI-Integrated Atlases of the Human Basal Ganglia and Thalamus, *Front Syst Neurosci* 5.
- [71] P. Hagmann, L. Jonasson, P. Maeder, J.-P. Thiran, V. J. Wedeen, R. Meuli, Understanding Diffusion MR Imaging Techniques : From Scalar Diffusion-weighted Imaging to Diffusion Tensor Imaging and Beyond, *RadioGraphics* 26 (2006) S205–S223.
- [72] R. Brown, A brief account of microscopical observations made in the months of June, July and August 1827, on the particles contained in the pollen of plants; and on the general existence of active molecules in organic and inorganic bodies, *The Philosophical Magazine* 4 (21) (1828) 161–173.
- [73] A. Einstein, Über die von der molekularkinetischen Theorie der Wärme geforderte Bewegung von in ruhenden Flüssigkeiten suspendierten Teilchen, *Annalen der Physik* 322 (1905) 549–560.
- [74] H. H. Mitchell, T. S. Hamilton, F. R. Steggerda, H. W. Bean, The Chemical Composition of the Adult Human Body and Its Bearing on the Biochemistry of Growth, *Journal of Biological Chemistry* 158 (3) (1945) 625–637.
- [75] C. Lenglet, J. S. W. Campbell, M. Descoteaux, G. Haro, P. Savadjiev, D. Wassermann, A. Anwender, R. Deriche, G. B. Pike, G. Sapiro, K. Siddiqi, P. M. Thompson, Mathematical methods for diffusion MRI processing, *NeuroImage* 45 (1 Suppl) (2009) S111–122.
- [76] D. Le Bihan, Looking into the functional architecture of the brain with diffusion MRI, *Nature Reviews. Neuroscience* 4 (6) (2003) 469–480.

- [77] T. B. Dyrby, L. V. Sogaard, M. G. Hall, M. Ptito, D. C. Alexander, Contrast and stability of the axon diameter index from microstructure imaging with diffusion MRI, *Magnetic Resonance in Medicine* 70 (3) (2013) 711–721.
- [78] P. J. Basser, J. Mattiello, D. LeBihan, Estimation of the effective self-diffusion tensor from the NMR spin echo, *Journal of Magnetic Resonance. Series B* 103 (3) (1994) 247–254.
- [79] A. L. Alexander, J. E. Lee, M. Lazar, A. S. Field, Diffusion Tensor Imaging of the Brain, *Neurotherapeutics : the journal of the American Society for Experimental NeuroTherapeutics* 4 (3).
- [80] B. J. Jellison, A. S. Field, J. Medow, M. Lazar, M. S. Salamat, A. L. Alexander, Diffusion Tensor Imaging of Cerebral White Matter : A Pictorial Review of Physics, Fiber Tract Anatomy, and Tumor Imaging Patterns, *American Journal of Neuroradiology* 25 (3) (2004) 356–369.
- [81] P. J. Basser, C. Pierpaoli, Microstructural and physiological features of tissues elucidated by quantitative-diffusion-tensor MRI, *Journal of Magnetic Resonance. Series B* 111 (3) (1996) 209–219.
- [82] T. E. J. Behrens, H. J. Berg, S. Jbabdi, M. F. S. Rushworth, M. W. Woolrich, Probabilistic diffusion tractography with multiple fibre orientations : What can we gain ?, *NeuroImage* 34 (1) (2007) 144–155.
- [83] D. S. Tuch, Q-ball imaging, *Magnetic Resonance in Medicine* 52 (6) (2004) 1358–1372.
- [84] R. T. Johnson, J. D. Yeatman, B. A. Wandell, M. H. Buonocore, D. G. Amaral, C. W. Nordahl, Diffusion properties of major white matter tracts in young, typically developing children, *NeuroImage* 88 (Supplement C) (2014) 143–154.
- [85] D. S. Tuch, T. G. Reese, M. R. Wiegell, N. Makris, J. W. Belliveau, V. J. Wedeen, High angular resolution diffusion imaging reveals intravoxel white matter fiber heterogeneity, *Magnetic Resonance in Medicine* 48 (4) (2002) 577–582.
- [86] M. Descoteaux, E. Angelino, S. Fitzgibbons, R. Deriche, Regularized, fast, and robust analytical Q-ball imaging, *Magnetic Resonance in Medicine* 58 (3) (2007) 497–510.
- [87] M. Descoteaux, High Angular Resolution Diffusion MRI : from Local Estimation to Segmentation and Tractography, Ph.D. thesis, University of Nice-Sophia Antipolis, Nice, France (2008).
- [88] E. M. Haacke, Y. Xu, Y.-C. N. Cheng, J. R. Reichenbach, Susceptibility weighted imaging (SWI), *Magnetic Resonance in Medicine* 52 (3) (2004) 612–618.
- [89] E. M. Haacke, S. Mittal, Z. Wu, J. Neelavalli, Y.-C. N. Cheng, Susceptibility-Weighted Imaging : Technical Aspects and Clinical Applications, Part 1, *American Journal of Neuroradiology* 30 (1) (2009) 19–30.

Bibliography

- [90] Y.-K. Tsui, F. Y. Tsai, A. N. Hasso, F. Greensite, B. V. Nguyen, Susceptibility-weighted imaging for differential diagnosis of cerebral vascular pathology : a pictorial review, *Journal of the Neurological Sciences* 287 (1-2) (2009) 7–16.
- [91] J. Duyn, MR Susceptibility Imaging, *Journal of magnetic resonance* (San Diego, Calif. : 1997) 229 (2013) 198–207.
- [92] V. Sehgal, Z. Delproposto, E. M. Haacke, K. A. Tong, N. Wycliffe, D. K. Kido, Y. Xu, J. Neelavalli, D. Haddar, J. R. Reichenbach, Clinical applications of neuroimaging with susceptibility-weighted imaging, *Journal of magnetic resonance imaging : JMRI* 22 (4) (2005) 439–450.
- [93] A. Abosch, E. Yacoub, K. Ugurbil, N. Harel, An Assessment of Current Brain Targets for Deep Brain Stimulation Surgery With Susceptibility-Weighted Imaging at 7 Tesla, *Neurosurgery* 67 (6) (2010) 1745–1756.

2

Thalamic Parcellation

The work presented in this chapter is originally published as “**Robust thalamic nuclei segmentation method based on local diffusion magnetic resonance properties**“ with co-authors : E. Najdenovska, G. Battistella, P. Maeder, N. Ghazaleh, A. Daducci, J.-P. Thiran, S. Jacquemont, C. Tuleasca, M. Levivier, E. Fornari and M. Bach Cuadra in **Brain Structure and Function 2017, Volume 222, Issue 5, pp 2203–2216**. E. Najdenovska, G. Battistella, E. Fornari and M. Bach Cuadra are equally contributing authors.

An extension of this study over a bigger cohort of healthy subject was done subsequently and the results are shown in section A.2.2 of the Appendixes.

2.1 Introduction

The thalamus, which is involved in the regulation of several sensorimotor and cognitive functions, acts as a relay station between cortical and subcortical areas. Many neural signals directed towards the cortex are routed through the thalamus via long ascending fiber tracts, while short fibers connect the thalamus to deep gray matter structures and cerebellum. The thalamus has a complex architecture, made of small cytoarchitectonically subdivided nuclei [1], which are connected to each other by intra-thalamic fibers. These nuclei mediate the thalamus’s involvement in a wide range of neurological functions and, therefore, are of key importance in many neurodevelopmental and neurodegenerative disorders.

The automatic segmentation of the thalamic nuclei in vivo using magnetic resonance imaging (MRI) has been limited by the difficulty of obtaining high-resolution images with sufficient contrast and by the lack of appropriate MRI-based features [2, 3]. The majority of the published

studies for thalamic nuclei segmentation are based on information derived from diffusion-weighted MR imaging (DWI). These approaches use local diffusion properties, such as the full diffusion tensor [4–7] and principal diffusion directions [8–12], global diffusion properties utilizing long-distance projections of each nucleus to the cortex [13, 14], or a combination of both local and global diffusion properties [15]. These approaches are of potential interest, but they present several drawbacks. Some of them use data acquired with a relatively low number of diffusion gradient directions [4, 6, 10, 12], while others can only identify few nuclei within the thalamus [11, 15]. Importantly, most methods require a prior knowledge for the primer initialization and give an outcome that is very sensitive to it [4, 8, 9, 11, 13–15]. Overall, robustness and consistency could not be properly evaluated because most of these methods have been tested in only a few subjects [4, 5, 7–9, 11, 13].

Tractography-based approaches [13, 14] represent an interesting alternative to the aforementioned local-based ones. They provide functionally reliable clusters [16], although these clusters do not necessarily correspond to cytoarchitectonic delineation [17]. Moreover, they are of limited use if the subject has abnormal white matter status or in the presence of large focal brain lesions, like tumors or vascular lesions. In such cases, fiber reconstruction algorithms can easily fail to identify the connectivity patterns.

The primary objective of this work is to introduce a novel segmentation framework for delineating the thalamic nuclei. The originality of our method is the use of the complete orientation distribution functions (ODFs) rather than a summary statistics, using diffusion MR images at 3 T. The use of spherical harmonics (SH) for the ODFs representation provides full angular characterization of the diffusion process at each voxel.

The framework was tested on 35 healthy volunteers. The diffusion data were acquired using a diffusion-weighted imaging (DWI) sequence widely used in a clinical setting, with the aim of potentially providing a useful tool in everyday clinical practice.

The evaluation of the results was performed both qualitatively, by an experienced neuroradiologist who compared them to a histological atlas, and quantitatively, by measuring clusters' extent and clusters' spatial distribution across subjects and hemispheres. We further assessed the reproducibility of our findings using a scan-rescan analysis as well as the robustness of our method across different MR scanners and sequence parameters. At last, we compared our results with the organization of the long connections between each thalamic nucleus and its projections depicted by diffusion MR-based tractography. Our approach could be of potential interest for studying brain anatomy in healthy subjects and for clinical purposes in patients with subcortical white matter lesions or tumours where global thalamo-cortical tractography cannot be performed.

2.2 Materials and methods

The local institutional review board approved the study and all participants gave written informed consent.

2.2.1 Data

The core of the research project (build-up of the segmentation pipeline, qualitatively and quantitative evaluation of the results) was built using subjects whose demographic characteristics are described in section Dataset 1. We further assessed robustness across different sequences and scanners, and intra-subject reproducibility of the thalamic clusters using two additional datasets (Dataset 2 and Dataset 3).

Dataset 1

Thirty-seven healthy subjects with no history of neurological illnesses, aged 20–70 years (mean \pm std, 42.5 ± 12 years), were recruited. The exclusion criterion was the presence of white matter alterations visible on fluid-attenuated inversion recovery (FLAIR) images examined by an experienced neuroradiologist. Two subjects were excluded because of technical problems during MRI acquisition leading to a final dataset of 35 control subjects. All subjects were scanned in a 3-T Siemens Trio scanner (Siemens AG, Erlangen, Germany) using a 32-channel head coil. The protocol included a sagittal T1-weighted gradient-echo sequence (MPRAGE), 160 contiguous slices, 1-mm isotropic voxel, repetition time (TR) 2300 ms, echo time (TE) 2.98 ms, field of view 256 mm as a basis for segmentation. FLAIR contrast images were acquired with a voxel size of $0.9 \times 0.9 \times 2.5 \text{ mm}^3$, flip angle 150° , TR 9500 ms, TE 84 ms, 32 axial slices. Diffusion-weighted images were acquired using a spin-echo echo-planar imaging sequence (64 gradient directions, b value 1000 s/mm^2 , voxel size $2 \times 2 \times 2.5 \text{ mm}^3$, 52 axial slices, TR 6700 ms, TE 89 ms, field of view $192 \times 192 \text{ mm}$) plus 1 volume without diffusion weighting (b value 0 s/mm^2 , i.e. b_0) at the beginning of the sequence as anatomic reference for motion and eddy current correction.

Dataset 2

Six healthy males (30.2 ± 6.2 years) were imaged with a 3-T Prisma Siemens scanner (Siemens AG, Erlangen, Germany). For all of them, an identical diffusion sequence was acquired twice the same day using the following parameters: TR/TE = 7800/78 ms, flip angle = 90° , 60 gradient directions with b value = 2000 s/mm^2 , voxel size of $2 \times 2 \times 2 \text{ mm}^3$, 60 axial slices and 10 volumes without diffusion weighting. Additional MPRAGE was obtained with TR/TE = 2300/2 ms, flip angle = 9° , voxel size of $1 \times 1 \times 1.2 \text{ mm}^3$, 160 axial slices.

Dataset 3

The third dataset was composed of two elderly essential-tremor patients (2 males, 86 years of age) treated with Gamma Knife thalamotomy. The images were acquired at two different time points : the day before the treatment and 6 months after using a 3-T Prisma Siemens scanner. The parameters for the diffusion sequence were similar to those used for Data 1 : TR/TE = 7100/84 ms, flip angle = 90° , 64 gradient directions with b value = 1000 s/mm^2 , voxel size of $2.2 \times 2.2 \times 2.2 \text{ mm}^3$, 62 axial slices and 10 volumes without diffusion weighting. The corresponding MPRAGEs on both dates were obtained with TR/TE = 2300/2 ms, flip angle = 9° , voxel size of $1 \times 1 \times 1.2 \text{ mm}^3$, 160 axial slices. Both patients underwent Gamma Knife surgery on their left thalamus, and consequently, we performed analyses only on their right thalamus.

2.2.2 Pre-processing

Diffusion-weighted images were first filtered using an isotropic Gaussian kernel ($\sigma = 0.8 \text{ mm}^3$) and then analyzed with FSL (<http://www.fmrib.ox.ac.uk/fsl/index.html>). The pre-processing of the diffusion dataset (64 gradient directions) involved motion and eddy current correction. In this step, each diffusion-weighted image was registered to the b_0 image (no diffusion encoding) using a 12-parameter affine transformation. This transformation accounts for motion between scans and residual eddy current distortions present in the diffusion-weighted images. The diffusion tensor was then estimated [18] and the three eigenvalues of the tensor were used to compute the fractional anisotropy (FA) map for each subject on a voxel-by-voxel basis [19]. This scalar measure of white matter fiber integrity was used to refine the segmentation of the thalamus (see section 2.2.3 for details).

In addition, the T1-weighted image was automatically segmented in the subject's native space in gray matter (GM), white matter (WM), and cerebrospinal fluid (CSF) using the unified segmentation approach [20] implemented in SPM8 (Wellcome Trust Centre for Neuroimaging : <http://www.fil.ion.ucl.ac.uk/spm/>) running under Matlab 7.11 (MathWorks Inc, Sherborn, MA, USA). The T1-weighted image was registered to the diffusion space using a rigid-body transformation with 6 degrees of freedom and Mattes Mutual Information as cost function [21]. The same transformation was then applied to the CSF probability map. The CSF image, together with the FA image, were used to increase the accuracy of the automatic thalamus extraction as described in the following paragraph.

2.2.3 Thalamus extraction

The processing steps to obtain an accurate mask of the whole thalamus are summarized in figure 2.1 . First, we performed cortical and subcortical parcellation of the T1-weighted images with the FreeSurfer software (<http://surfer.nmr.mgh.harvard.edu>). The subcortical parcellation includes the pre-processing of the MRI data (bias correction, intensity normalization) and the subcortical labeling of the tissues classes [22, 23]. Second, the labels corresponding to the

right and the left thalamus were identified, converted to binary masks, and registered to the diffusion space by applying the previously estimated transform (details in section 2.2.2). Third, the registered binary masks of the thalamus were then refined using the CSF and FA maps. To exclude partial volume contaminations, we only considered voxels with CSF probability value lower than 0.05. In addition, to avoid partial volume of the internal capsule in the proximity of the thalamus, voxels within a 2-mm distance from the border of the mask with FA values greater than 0.55 were also excluded. All these steps were performed in each subject's diffusion space.

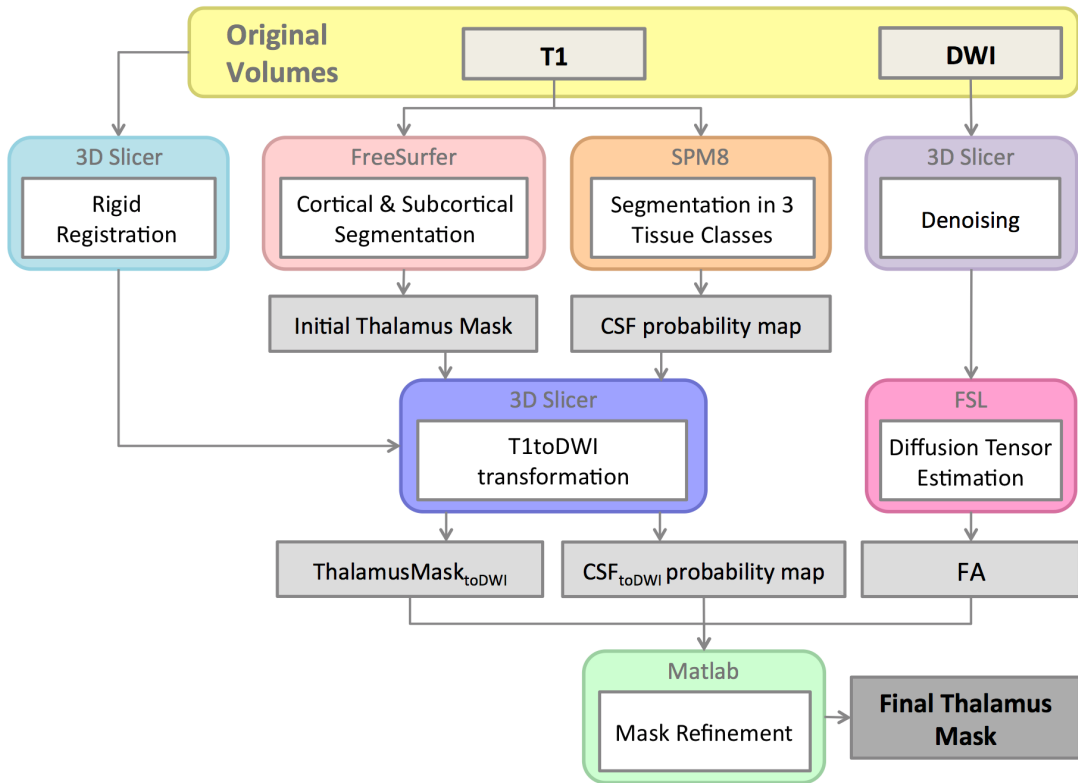


FIGURE 2.1 – Outline of the main pre-processing steps for accurate thalamus extraction

2.2.4 Reconstruction of the orientation distribution functions (ODFs)

The orientation distribution functions (ODFs, equation 2.1) were computed using q-ball imaging in constant solid angle [24] using the *Qboot* tool available in FSL :

$$ODF_{CSA}(\mathbf{u}) \propto FRT\{\Delta_b^2 \ln(-\ln \frac{S(\mathbf{u})}{S(0)})\} \quad (2.1)$$

where FRT is the Funk Radom transform, and Δ_b^2 the Laplace–Beltrami operator. The diffusion signal S was modeled by means of the real and symmetric spherical harmonic (SH) basis as in

[25] :

$$\ln\left(-\ln\frac{S(\mathbf{u})}{S(0)}\right) = \sum_{j=1}^{(l+1)(l+2)/2} c_j Y_j(\mathbf{u}) + e_{bstr} \quad (2.2)$$

with c_j the coefficient of the j^{th} SH basis function Y_j , l the maximum SH basis order, and e_{bstr} the Bootstrapped residual.

For each subject, the *Qboot* algorithm was applied by setting the maximum number of ODF peaks to be detected to 2 using 50 samples for residual bootstrapping [26], as in the default settings of the *Qboot* command in FSL. The maximum SH basis order was instead set to 6 ($l = 6$). Results of the *Qboot* bootstrapping were samples of ODF shapes for each voxel, and the mean coefficients of each voxel served as inputs to the clustering algorithm.

The SH basis allows a full angular characterization of the ODFs (figure 2.2) by means of real-SH vectors. Therefore, it was possible to assess similarities of diffusion properties across ODFs using simple distance metrics [27].

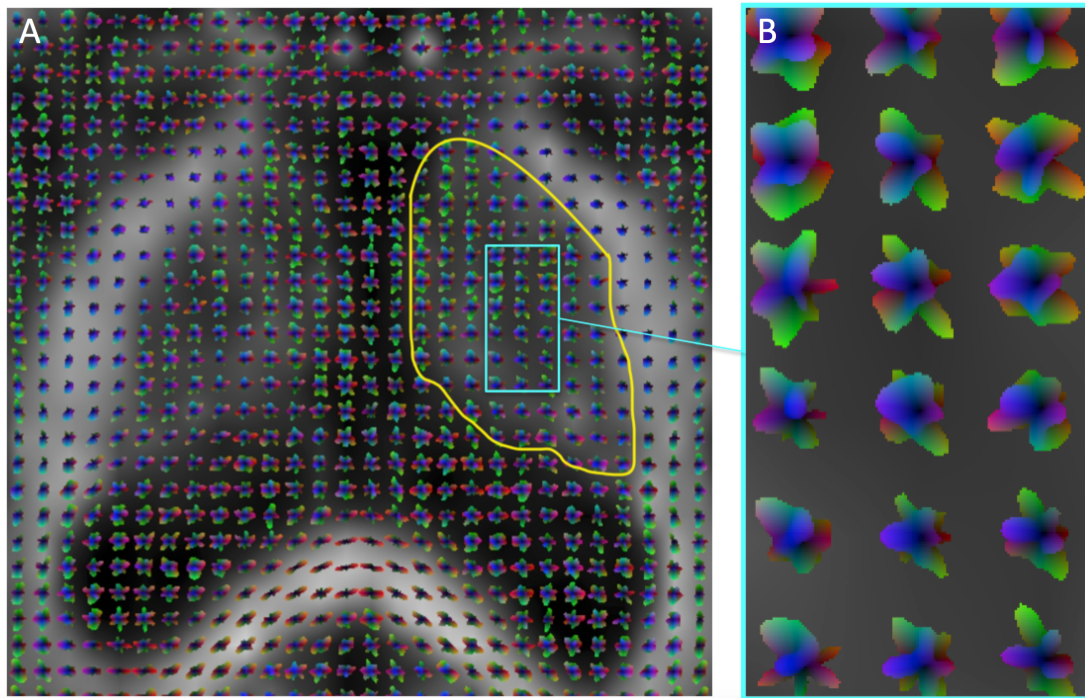


FIGURE 2.2 – Visualization of the ODFs in a slice of the thalamus. The yellow contour in A delineates the thalamus, while B provides a close-up view of the ODFs shapes inside the thalamic area identified by the light-blue box

2.2.5 Clustering of the thalamic nuclei

Clustering was performed using a modified unsupervised k-means algorithm. A schematic overview of our method is shown in figure 2.3. Inputs were mean SH coefficients and voxel position. The number of clusters to be segmented was set to seven based on a preliminary analysis that used a lower number of subjects aimed at determining the maximum number of clusters that would provide a robust segmentation pattern across subjects. Additionally, previous studies subdivided the thalamus in seven nuclei [13, 14].

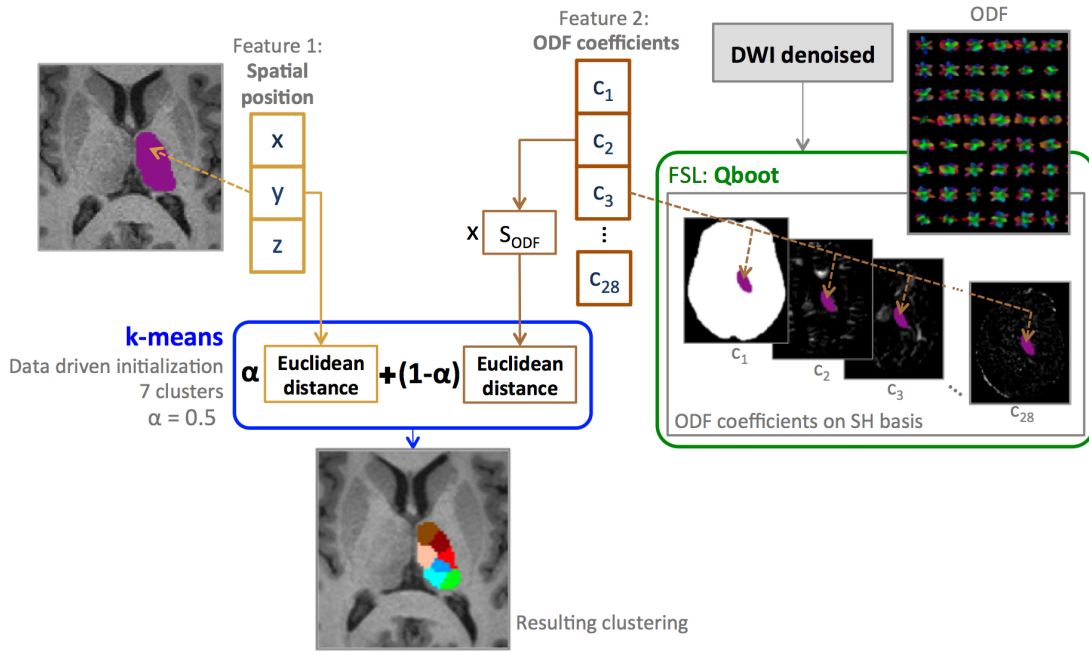


FIGURE 2.3 – Schematic overview of the clustering framework. Segmentation of the seven thalamic nuclei has been performed using a k-means clustering algorithm with two equally weighted features : the spatial position of the voxels inside the thalamus (x, y, z) and the mean ODF coefficients ($C_i, i \in [1, 28]$) expressed in the SH basis of maximum order 6. k-means is initialized in a data-driven fashion

The decision metric for the final clustering was a combination of the Euclidean distance of the voxels position and of the Euclidean distance calculated from the SH coefficients (equation 2.3) :

$$\|ODF - ODF'\| = \sqrt{\sum_{j=1}^R (c_j - c'_j)^2} \quad (2.3)$$

To avoid any bias in the k-means clustering, we applied a scaling factor (S_{ODF}) to the SH coefficients to scale the ODF distances inside the interval of the spatial-distance values. The scaling factor $S_{ODF} = 55$ was first empirically estimated on a small group of subjects and then

applied to the remaining dataset. The contribution of the two features to the final clustering was equal, i.e. the weight α was set to 0.5.

To avoid dependency of the results on the initialization method, we first ran 5000 randomly initialized k-means, using only the position as the input feature, and then used the average centroid over the 5000 results as the initial setting for the clustering algorithm.

2.2.6 Evaluation of the results

To assess the robustness of the outcome, we studied the average spatial distribution of the resulting clustering. Clustering results were all registered to the Montreal Neurological Institute (MNI) space using a combination of rigid, affine, and B-spline transformations (with 5 as maximum allowed displacement of the control grid along each axis) implemented in 3D Slicer (<http://www.slicer.org>). We then created a weighted average map in which each voxel was defined with the label value represented by the majority of subjects in that voxel (we will further refer to it as weighted mean map by majority voting or just mean segmentation map).

The assessment of the thalamic nuclei clustering is extremely challenging due to the absence of a gold standard, and this limitation is shared by all previously proposed techniques. Moreover, none of the methods in the literature evaluated reproducibility across different time points or different diffusion sequences. To this end, four different approaches for evaluating the anatomical consistency of our results were used.

(a) Qualitative evaluation

An experienced neuroradiologist (PM) visually assessed the quality of the segmentation results and further compared them to Morel histological atlas [17].

(b) Quantitative evaluation

i. Symmetry between the left and the right thalamus. To test the symmetry between results of the left and right thalamus, we statistically compared the volume and the spatial distribution of the centroids of each segmented cluster between the left and the right hemisphere using a non-parametric Wilcoxon signed-rank test. All analyses were performed on the subjects' diffusion space. For each hemisphere, each cluster volume was normalized by the size of the thalamus to take into account the inter- and the intra-individual size variability. The distribution of the centroids was calculated using a distance map representing the relative position of the centroids' coordinates to the closest contour of the thalamus mask.

ii. Intra-subject reproducibility. We assessed intra-subject variability using scan-rescan data from Dataset 2 and Dataset 3. For each subject, we performed the clustering on both time points scans separately. The resulting clusters obtained from each dataset were brought to

the same image space by applying a rigid 6-parameter transformation, which was estimated with 3D Slicer [21]. Finally, clusters of scan–rescan time points were quantitatively compared using:

- Dice’s coefficient for assessing the overlap
- Euclidean distance between the centroids
- Modified Hausdorff distance for evaluating the similarity between the cluster contours. The modified distance has been shown to be more robust to outliers than the traditional Hausdorff distance [28].

(c) Comparison with thalamic long connections

The behavior of our algorithm, which uses local information derived from DWI, was compared to the organization of the long fibers connections between the thalamus and its afferent and efferent projections. We used probabilistic tractography (computed with probtrackx from FSL package) to highlight those pathways. Based on anatomy [29], we first identified, for each group of thalamic nuclei, the regions characterizing its afferent and efferent connections. The mask of the whole left thalamus was maintained as a constant seed region in the tractography, while target masks were chosen according to the regions representing the two endpoints of each specific pathway of interest.

The results of the tractography showed the portion of the thalamus whose fibers were connected to the target masks. We then compared the location of those subparts of the thalamus with our clustering results. For each cluster, we defined the frequency of success (FS) as the percentage of subjects in which the tract of interest overlapped the expected cluster.

For each cluster in each subject, probabilistic streamlines were computed using the modified Euler integration [30], by drawing 7000 individual samples using a value of 0.5 mm for step length and 0.2 for curvature threshold. To reduce potential bias from spurious tracts, we have excluded voxels having probabilistic streamlines value below 5% of the maximum. All the streamlines between the respective that survive this threshold were considered as part of the tracts of interest and included in a mask.

(d) Comparison with state-of-art methods based on local diffusion properties

Up to date, the angular difference (AD) between the principle directions of the diffusion tensor was considered as the most reliable local feature for thalamic nuclei parcellation [8]. To assess our contribution and the advantage of using SH representations of the ODFs over existing techniques, we compared the results of our pipeline with those obtained using AD as feature. First, we computed the diffusion tensor at each voxel with FSL diffusion toolbox, and then, instead of using the Euclidean distance between the ODF coefficients inside the clustering framework, we calculated the angular difference between the main eigenvector of the diffusion tensor [8, 10, 12]. In order to have both distances in the same range of values within the k-means algorithm, we scaled AD after computing it by a factor of 6, which was

empirically determined. Comparison between ODF and AD features is done at one time point (using Morel’s atlas for validation in two different axial slices) as well as with scan–rescan setting.

2.3 Results

The thalamic nuclei clustering in Dataset 1 was highly reproducible and characterized by a robust pattern of spatial distribution. Only one subject out of the 35 deviated from this pattern. In fact, he presented an intensity spike in ODF coefficients’ values as an artifact of the reconstruction that anomalously biased the clustering. Therefore, this subject was removed from further analysis. The mean segmentation map that represents the spatial distribution pattern is shown in figure 2.4 , while figure 2.5 gives an example of five individual results.

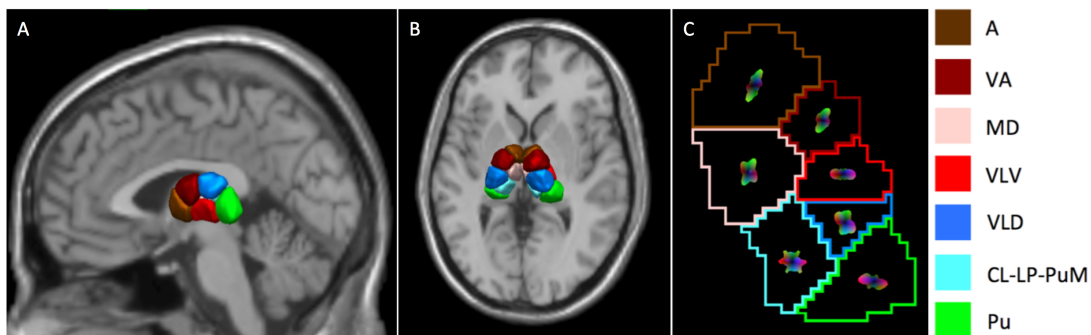


FIGURE 2.4 – Rendering of the weighted mean clustering map by majority voting. The map is superposed on a T1-weighted image in the Montreal Neurological Institute (MNI) space in sagittal (A) and transversal (B) views. Panel C represents the mean ODF characteristic for each cluster. Each averaged ODFs were reconstructed on a representative subject and superposed on the weighted mean clustering map. Thalamic nuclei are color-coded as follows : *brown* for the anterior group (A), *maroon* for the ventral anterior group (VA), *light pink* for the medio-dorsal group (MD), *red* for the ventral latero-ventral group (VLV), *blue* for the ventral latero-dorsal group (VLD), *green* for the pulvinar (Pu), and *cyan* for the cluster representing the central lateral nucleus, the lateral posterior and a portion of the medial part of the pulvinar (CL–LP–PuM)

(a) Qualitative evaluation

For each subject, the expert evaluated the spatial distribution and extent of the clusters segmented with our algorithm, and while comparing them to Morel’s atlas, he labeled each cluster by its anatomical correspondence (see figures 2.4, 2.6 and 2.7). Six out of seven clusters could be uniquely identified as a known anatomical nucleus or group of nuclei, and we, therefore, assigned the name of the dominant nucleus to each of them in each respective group. The seventh cluster instead, was characterized by two predominant nuclei, the central lateral (CL) and the lateral posterior (LP), as well as by a portion of the anterior part of the

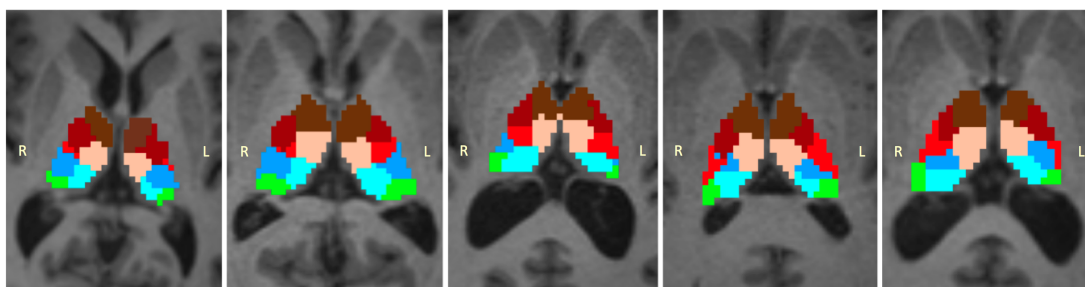


FIGURE 2.5 – Individual results of the thalamic nuclei segmentation. Spatial distribution of the segmented nuclei are shown in axial view for five different cases and superposed on each subject’s MPRAGE image

TABLE 2.1 – Statistical comparison of the normalized volumes of the thalamic nuclei across hemispheres

Volume							
Wilcoxon signed-rank	Pu	A	MD	VLD	CL-LP_PuM	VA	VLV
p value	0.77	0.55	0.5	0.28	0.14	0.63	0.25
Median values (mm)							
Left	0.1319	0.1599	0.1571	0.1239	0.1248	0.1540	0.1371
Right	0.1331	0.1618	0.1606	0.1317	0.1317	0.1513	0.1326

medial pulvinar (PuM). The anatomical partitions derived from our clustering were labeled as follows : anterior group (A), ventral anterior group (VA), medio-dorsal group (MD), ventral latero-ventral group (VLV), ventral latero-dorsal group (VLD), pulvinar (Pu) and CL-LP-PuM group (see figures 2.4, 2.6 and 2.7).

Based on the qualitative comparison with the histological atlas, one subject did not pass the expert evaluation, since the spatial distribution of the segmented clusters deviated from the one of the other 33 cases. We assume that such an outcome is due to large neuroanatomical variation, but since it represented an outlier, we decided to exclude this subject from further evaluation analyses.

(b) Quantitative evaluation

i. Symmetry between the left and the right thalamus. We observed an important symmetry between the results on the left and on the right thalamus across all subjects, which was confirmed by our statistical analysis. As shown in tables 2.1 and 2.2 respectively, neither the normalized volumes nor the centroids distribution of the corresponding cluster over hemispheres were significantly different.

ii. Intra-subject reproducibility. The resulting clustering from Dataset 2 and Dataset 3 presented the same segmentation pattern as observed for the 33 subjects in Dataset 1. Similarly, the same

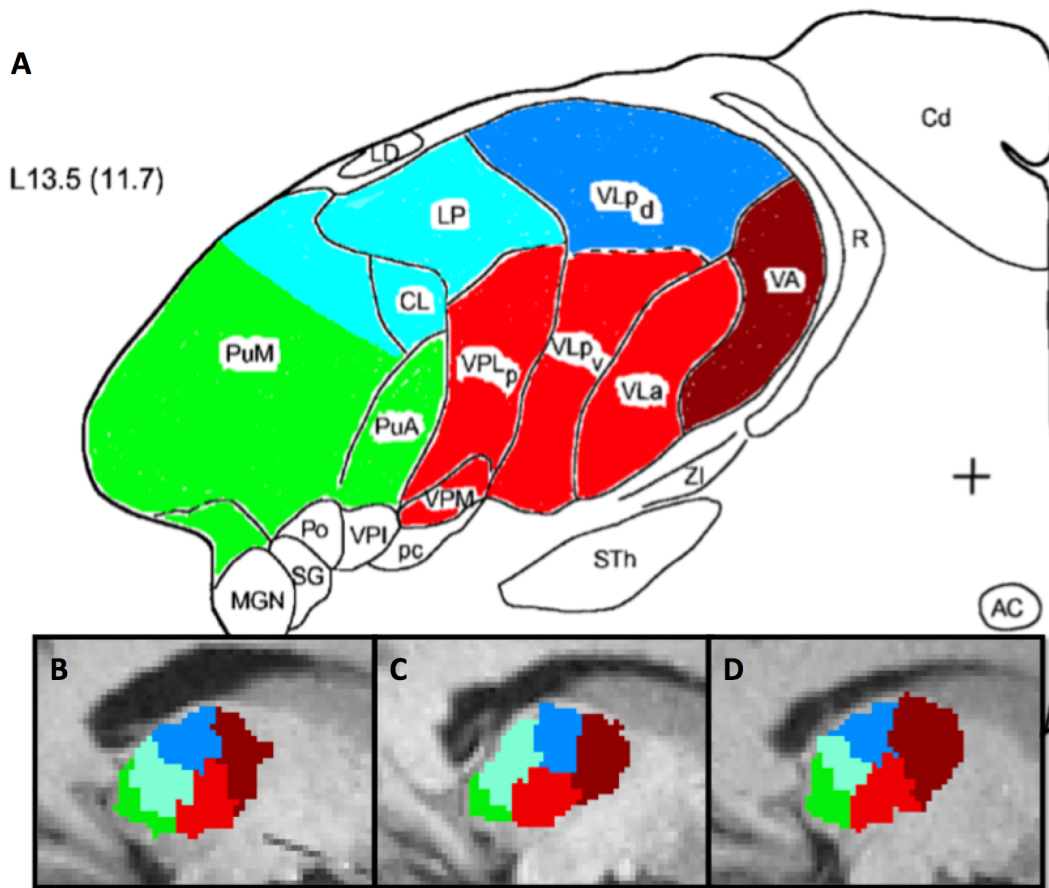


FIGURE 2.6 – Comparison of the results of our clustering algorithm with the Morel’s histological atlas. **A** shows a sagittal view of the Morel atlas. **B-D** show instead the spatial distribution of the thalamic nuclei segmented with our framework in the same sagittal slice for three different cases in the Talairach space. Each color gives the anatomical correspondence of each group of nuclei

pattern was observed in the scan–rescan analysis in both datasets. In particular, for all the 14 inspected thalami, the average Dice’s coefficient value per cluster was always higher than 0.8, while centroid’s and Hausdorff distance were lower than the original spatial resolution of the diffusion images used. Table 2.3 gives a summary of these results, while figures 2.7, A.9 and A.10 in the Appendixes show a visual illustration of them, together with additional comparisons with Morel’s atlas.

(c) Comparison with thalamic long connections

According to the anatomy [29], we reconstructed six specific pathways, one for each nucleus characterized by a unique anatomical distribution, i.e. A, VA, MD, VLD, VLV, and Pu. The respective pairs of target masks that define the specific pathway for each cluster are summarized in table 2.4.

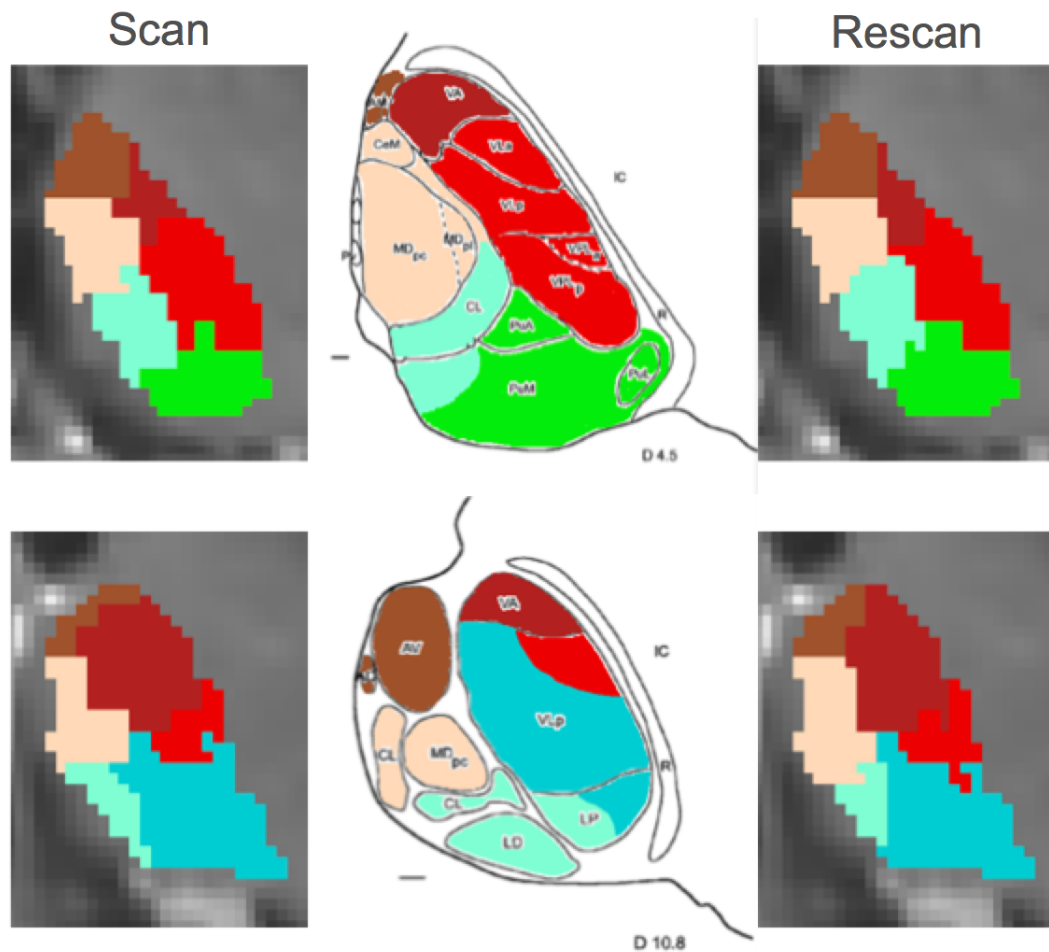


FIGURE 2.7 – Resulting clustering from the scan–rescan analysis compared with two different axial slices from the Morel’s atlas (D 4.5 and D 10.8 top and bottom row, respectively)

This approach included all clusters except CL–LP–PuM since it is composed by more than one dominant nucleus ; thus, its specific pathway could not be uniquely identified.

The estimated average FS for all clusters was 92.4% with minimum value of 81.8% for the VA cluster and maximum of 100% for the pulvinar. More details about FS values for each cluster, respectively, are given in table table 2.4.

An illustration of the motor tract passing through the VLV cluster is given in figure 2.8. Examples of the reconstruction of two other tracts are shown in figure A.11 of the Appendixes.

(d) Comparison with state-of-art methods based on local diffusion properties

Unlike the results given by our ODF-based approach, the AD-based segmentation clustered nuclei whose spatial distribution could not be uniquely assigned to a specific anatomical

Chapitre 2. Thalamic Parcellation

TABLE 2.2 – Statistical comparison of the centroids distribution of the thalamic nuclei across hemispheres

Centroids' border distance							
Wilcoxon signed-rank	Pu	A	MD	VLD	CL-LP_PuM	VA	VLV
p value	0.75	0.4	0.36	0.49	0.39	0.79	0.24
Median values (mm)							
Left	2	2.2361	2.1180	2	2	2.2361	2
Right	2	2.2361	2.2361	2.2361	2.2361	2.2361	2

TABLE 2.3 – Quantitative measures of similarity between the scan–rescan clusters

Measure	Dice coefficient		Centroids' distance (mm)		Hausdorf distance (mm)	
	Mean	Variance	Mean	Variance	Mean	Variance
Cluster						
Pu	0.93	0.0007	0.56	0.08	0.17	0.0025
A	0.90	0.0024	0.86	0.34	0.24	0.0036
MD	0.84	0.0080	1.36	1.08	0.28	0.0055
VLD	0.87	0.0018	0.98	0.26	0.27	0.0043
CL-LP-PuM	0.83	0.0101	1.41	1.24	0.28	0.0053
VA	0.89	0.0016	0.79	0.28	0.26	0.0038
VLV	0.89	0.0031	0.66	0.26	0.22	0.0019

TABLE 2.4 – Summary of the pairs of target masks chosen for the reconstruction of the pathways characteristic of each group of nuclei

Cluster	Target 1	Target 2	FS (%)
A	Anterior cingulate cortex	Fornix	97
VA	Premotor cortex (Brodmann area 6)	Substantia nigra	81.8
MD	Middle frontal sulcus	Amygdala	90.9
VLD	Posterior singular cortex	Fornix	87.9
VLV	Precentral gyrus	Red nucleus (left) and superior cerebellar peduncle (right)	97
Pu	Inferior angular gyrus	Calcarine sulcus	100

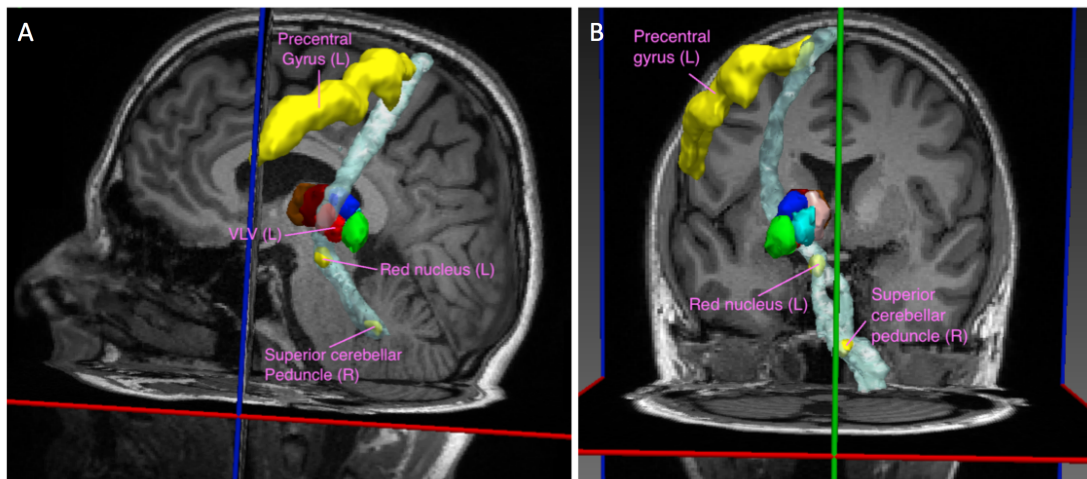


FIGURE 2.8 – Reconstruction of thalamic long connections. Sagittal **A** and coronal **B** 3D views of the motor fiber tracts passing through the cluster VLV (in *red*). Probabilistic tracts (in *white*) were reconstructed using the whole thalamus mask and the following seed regions (in *yellow*): left precentral gyrus, left red nucleus, and right superior cerebellar peduncle

group, according to the Morel’s atlas (see figures 2.7, A.9 and A.10). We further noticed that the clusters distribution obtained from Dataset 2, characterized by a diffusion acquisition at high b value, had less smooth boundaries, noisy contours, and isolated voxels.

In the scan–rescan framework, we observed lower intra-subject reproducibility of the AD-based segmentation compared to the ODF-based one. These observations were then confirmed with the quantitative measures showed in figure 2.9. More precisely, the average Dice coefficients per cluster from the AD-based segmentation were between 0.5 and 0.8, while the average distance between the corresponding centroids reached 4 mm.

2.4 Discussion

We presented a novel segmentation framework based on local diffusion properties and spatial features for thalamic nuclei clustering in diffusion MRI. Unlike most of the existing methods, which are limited by the low angular resolution of DWI [4–11], ours provides a robust and accurate diffusion-based segmentation by the inclusion of the orientation distribution functions (ODFs) from MR images at 3 T. Our major contribution is the use of spherical harmonics for the ODFs representation that provide full angular characterization of the diffusion processes in each voxel, and, therefore, a better differentiation of the complex intra-thalamic microstructure [29]. We proved the robustness of our approach across sequences, scanners and acquisitions at different time points. We further demonstrated its outperformance compared to AD-based clustering.

The segmentation was performed using the k-means algorithm. Unlike the state-of-the-art

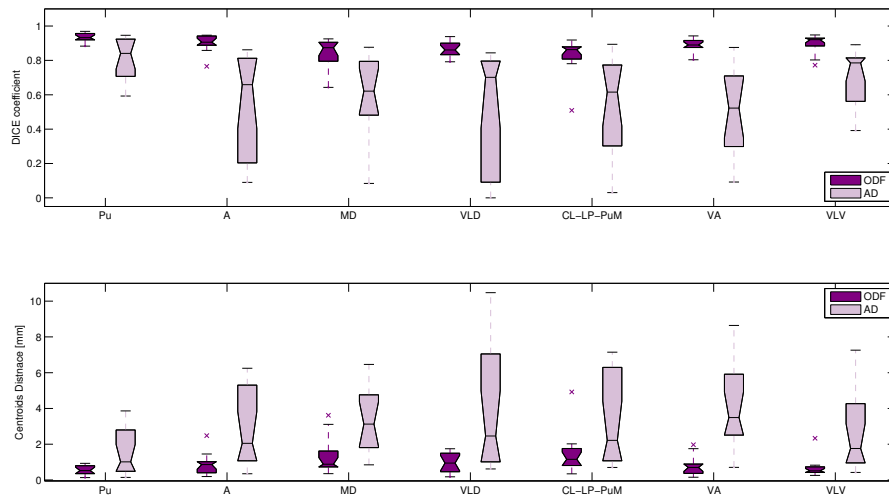


FIGURE 2.9 – Quantitative measures of overlap between the corresponding clusters in scan-rescan analysis : ODF- versus AD-based segmentation

methods published so far, the initialization made in a data-driven fashion (primer centroids extracted from 5000 initial randomly-initialized k-means runs) adds another strong point to our framework since it is a user-independent procedure. Moreover, such initialization might be a contributing factor to the high reproducibility of the final clustering results.

We segmented the thalamus in seven independent groups of nuclei with a success rate of 97.1% of the tested 35 cases. Six clusters are characterized with unique anatomical distribution, while the importance of the seventh cluster, the CL-LP-PuM, comes from the nuclei grouped within. More precisely, CL is part of the intralaminar nuclei, which are characterized by various connections to frontal and parietal cortices, and potentially involved in arousal mechanisms [31], while LP together with the pulvinar take part in attention processes to visual stimuli [32]. The choice of the number of nuclei was based on a preliminary analysis aiming at identifying the number of clusters that provide a robust segmentation pattern and was further supported by the existing approaches used in the literature. Thalamic nuclei segmentation using thalamo-cortical projections [13] used seven cortical targets to draw probability distribution of connections from voxels within the thalamus to those regions that have been shown to correspond to known connection areas of major thalamic nuclear groups. On the other hand, the myelo- [33] and cytoarchitectonical [17] atlases, which, instead, provide histological information about the structural organization of the thalamus, give a more complete and detailed picture of the thalamic nuclei even though they are built on very limited number of specimens, and therefore, they do not account for any anatomical variability. Nevertheless, as in the Morel atlas [17], all nuclei can be spatially grouped into seven main groups. In addition, the number of clusters used in our study seemed to be a good trade-off between spatial resolution of the ordinary DWI acquisition and anatomical accuracy of the clustering. For instance, a recent

work [12] attempted to segment the thalamus in 21 different clusters but only five of them appeared to be consistent across subjects. Collectively, these considerations suggest that the robustness of the segmentation method is preserved solely for a small number of clusters when utilizing classical diffusion sequences.

The developed framework was tested in a main dataset of 35 healthy volunteers, which is a relatively large dataset compared to the data used for testing the majority of the existing methods. Validation also remains a challenge for all previously published methods. By employing four different evaluation approaches to assess the results (qualitative comparison of the segmented clusters to the cytoarchitectonic atlas, quantitative analysis of cluster spatial extent and volume across hemispheres, as well as intra-subject reproducibility and correspondence of the thalamic clusters distribution to thalamic long connections), we ensured thorough validation of our algorithm.

A high degree of symmetry of nuclei volume and spatial distribution is in accordance with previous studies using fiber-tracking connectivity-based clustering [13], functional information derived from resting-state BOLD signal [34–36], and histological reports [37]. In fact, the reported cerebral asymmetries in the brain are mainly related to its functional activity. For instance, language functions are historically known to be left-lateralized, while those involved in spatial orientation and emotional control are predominantly associated with the right hemisphere [38, 39]. In our study, since we recruited only right-handed subjects, we could expect possible inter-hemispheric differences between the groups of nuclei involved in motor control (i.e. the VLV) because of the largely known motor-related lateralization of the brain [40]. To the best of our knowledge, there is no evidence of strong structural left–right asymmetries in the spatial organization of the thalamic nuclei, and our findings are in line with that. Another reason for the absence of hemispheric asymmetries can be attributed to the low spatial resolution of the DWI acquisition in comparison to the small size of the thalamus. This represents a limitation of our study that is shared with all the previous published research on the same topic.

The findings from the core data (Dataset 1) were also observed in the analyses of the additional two datasets, proving the reproducibility of the outcome over different diffusion sequences and different scanner machines. Moreover, in a scan–rescan scenario, with very high Dice values considering the relative small size of the clusters, we show strong reproducibility of the results over different time points, and therefore, we reinforce the validation of our findings. The reproducibility of the test-retest analysis is also proven by both centroids and borders distances, which are always smaller than the original spatial resolution of the used diffusion data.

We also performed a long-connection tractography-based analysis to further evaluate the robustness of our clustering algorithm and the ability to identify appropriate anatomical pathways described in the literature [29]. We observed a high frequency of success (FS) for the expected overlaps, 92.4% in average, which further supports the anatomical accuracy of the spatial distribution of the segmented clusters. We want to emphasize the fact that such

evaluation has no intent of comparing fiber-tracking-based clustering with our local diffusion property-based clustering. Instead, to provide additional anatomical value to our results, we tested the hypothesis that the main thalamo-cortical fibers characteristic of a nucleus should pass through it.

Our clustering method, which is based on local diffusion properties, is a robust tool for thalamic nuclei segmentation that closely matches histological atlases. We showed that our method outperforms recent state-of-the-art methods based on local diffusion properties, or more precisely, the angular difference (AD), in terms of reproducibility and parcellation matching closely with the known anatomical architecture of the thalamus. Moreover, the AD-based segmentation outcome presented less smooth cluster boundaries for diffusion data acquired with b values of 2000 s/mm². We assume this is due to the limitations of the tensor modeling that fails to represent properly the additional diffusion information, presumably coming from the intra-voxel compartments [41] that such data provide.

Our results differ from cortical connectivity-based approaches results [13, 14], which generally found overlapping connections to multiple cortical areas as well as great inter-subject variability. Several factors may have contributed to this result. First, the cortical target ROIs used for tractography were large and characterized by fuzzy borders, which favored the existence of multiple cortical connections from each connectivity-defined thalamic region. Second, the diffusion tractography is sensitive to major pathways, and therefore, smaller pathways, especially if crossing other tracts, are not always detected. Third, the thalamus is a very complex structure, characterized by different cell types and specific cortical connections (matrix and core neurons ; [42]) which can bias the results of long-connection fiber tractography. It should also be considered that the thalamus segmentation by fiber-tracking does not necessarily correspond to an anatomical subdivision of the thalamus [13, 14, 43, 44]. This is particularly true for nuclei connected to the sensorimotor cortex, whereas good correspondence was found for the pulvinar, the thalamic nucleus mainly projecting to the occipital cortex [45]. This scenario has also been replicated in functional-based connectivity studies [34]. They revealed distinct features of thalamo-cortical connectivity [36] when compared to structural-based ones, showing that these two methodologies provide complementary information. As with tractography-based approaches, they share the same problems of overlapping of connectivity and inter-subject variability.

With the aim of providing a tool of a potential interest in everyday clinical practice, we estimated the ODFs using a DWI sequence typically acquired in a clinical setting. As a drawback, we share the limitation of all the other published studies so far that are related to the low spatial resolution of the DWI sequences. With a voxel size of approximately 2 x 2 x 2 mm³, we were not able to distinguish smaller nuclei or nuclear groups. Complementary techniques should be additionally considered to drive the segmentation towards smaller anatomical subdivisions. These include high angular acquisition schemes, such as diffusion spectrum imaging (DSI), which has been demonstrated to better characterize crossing fibers [46], and/or the use of high-field MRI scanner. For instance, it has been shown that susceptibility-weighted imaging

acquired at 7 T [47], is able to provide complementary information to those extracted from DWI about thalamic microstructure, which can help in delineating the different groups of thalamic nuclei. Future studies may also include the acquisition of diffusion images at higher b values ($>2000 \text{ s/mm}^2$), and/or the use of scanner with higher gradient systems.

With our approach, we were able to show robust and anatomically consistent segmentation of the main groups of thalamic nuclei. Thus, our framework can be of potential use in many clinical applications. We would like to emphasize that unlike the cortical connectivity-based algorithms, relying on local diffusion properties may be an important asset when studying patients that have moderate or severe lesions in WM or GM (such as tumors, stroke or vascular lesions), for whom long-distance fiber-tracking may fail. Other examples of possible applications can be related to movement disorders. Our recent findings [48] in young asymptomatic FMR1 premutation carriers at risk of developing a late-onset movement disorder called fragile X tremor–ataxia Syndrome (FXTAS), encourage further evaluation of the motor-control pathway and in particular, the thalamic ventral intermediate nucleus (Vim) that is part of this network (included in the VLV group in this study). Similarly, the VLV delineation is of potential interest to clinical studies and treatment planning for other movement-related disorders, such as essential tremor, where the central element is again the Vim [49]. The automatic delineation of all seven groups of nuclei also represent a useful tool for studies related to brain development [50] or to better interpret functional studies.

2.5 Conclusion

We propose a novel automated framework for segmenting the thalamic subparts, which explores the orientation distribution functions represented in spherical harmonics basis from diffusion MR images at 3 T. The ability to fully characterize the crossing fibers, in addition to a data-driven initialization of the clustering algorithm, provides a robust, reproducible and an accurate segmentation of seven groups of thalamic nuclei that outperforms the current state-of-art based on local diffusion properties. Each segmented nuclei group has a characteristic spatial distribution, which closely matches histological atlases, and identifies a major cortico-thalamic pathway.

Bibliographie

- [1] S. M. Sherman, R. W. Guillery, The role of the thalamus in the flow of information to the cortex., *Philosophical Transactions of the Royal Society B : Biological Sciences* 357 (1428) (2002) 1695–1708.
- [2] T. Gringel, W. Schulz-Schaeffer, E. Eloff, A. Frölich, P. Dechent, G. Helms, Optimized high-resolution mapping of magnetization transfer (MT) at 3 Tesla for direct visualization of substructures of the human thalamus in clinically feasible measurement time, *Journal of magnetic resonance imaging : JMRI* 29 (6) (2009) 1285–1292.
- [3] T. Tourdias, M. Saranathan, I. R. Levesque, J. Su, B. K. Rutt, Visualization of intra-thalamic nuclei with optimized white-matter-nulled MPRAGE at 7t, *NeuroImage* 84 (2014) 534–545.
- [4] M. R. Wiegell, D. S. Tuch, H. B. W. Larsson, V. J. Wedeen, Automatic segmentation of thalamic nuclei from diffusion tensor magnetic resonance imaging, *NeuroImage* 19 (2 Pt 1) (2003) 391–401.
- [5] Y. Duan, X. Li, Y. Xi, Thalamus segmentation from diffusion tensor magnetic resonance imaging, *International Journal of Biomedical Imaging* 2007 (2007) 90216.
- [6] L. Jonasson, P. Hagmann, C. Pollo, X. Bresson, C. Richero Wilson, R. Meuli, J.-P. Thiran, A level set method for segmentation of the thalamus and its nuclei in DT-MRI, *Signal Processing* 87 (2) (2007) 309–321.
- [7] L. Rittner, R. A. Lotufo, J. Campbell, G. B. Pike, Segmentation of thalamic nuclei based on tensorial morphological gradient of diffusion tensor fields, in : 2010 IEEE International Symposium on Biomedical Imaging : From Nano to Macro, 2010, pp. 1173–1176.
- [8] U. Ziyang, D. Tuch, C.-F. Westin, Segmentation of Thalamic Nuclei from DTI Using Spectral Clustering, in : *Medical Image Computing and Computer-Assisted Intervention - MICCAI 2006*, Lecture Notes in Computer Science, Springer, Berlin, Heidelberg, 2006, pp. 807–814.
- [9] U. Ziyang, C.-F. Westin, Joint Segmentation of Thalamic Nuclei from a Population of Diffusion Tensor MR Images, *Medical image computing and computer-assisted intervention : MICCAI International Conference on Medical Image Computing and Computer-Assisted Intervention* 11 (2008) 279–286.
- [10] S. C. Mang, A. Busza, S. Reiterer, W. Grodd, A. U. Klose, Thalamus segmentation based on the local diffusion direction : a group study, *Magnetic Resonance in Medicine* 67 (1) (2012) 118–126.

Bibliography

- [11] C. Ye, J. A. Bogovic, S. H. Ying, J. L. Prince, Parcellation of the Thalamus Using Diffusion Tensor Images and a Multi-object Geometric Deformable Model, *Proceedings of SPIE* 8669.
- [12] V. Kumar, S. Mang, W. Grodd, Direct diffusion-based parcellation of the human thalamus, *Brain Structure & Function* 220 (3) (2015) 1619–1635.
- [13] T. E. J. Behrens, H. Johansen-Berg, M. W. Woolrich, S. M. Smith, C. a. M. Wheeler-Kingshott, P. A. Boulby, G. J. Barker, E. L. Sillery, K. Sheehan, O. Ciccarelli, A. J. Thompson, J. M. Brady, P. M. Matthews, Non-invasive mapping of connections between human thalamus and cortex using diffusion imaging, *Nature Neuroscience* 6 (7) (2003) 750–757.
- [14] J. O’Muircheartaigh, C. Vollmar, C. Traynor, G. J. Barker, V. Kumari, M. R. Symms, P. Thompson, J. S. Duncan, M. J. Koepp, M. P. Richardson, Clustering probabilistic tractograms using independent component analysis applied to the thalamus, *NeuroImage* 54 (3) (2011) 2020–2032.
- [15] J. V. Stough, J. Glaister, C. Ye, S. H. Ying, J. L. Prince, A. Carass, Automatic method for thalamus parcellation using multi-modal feature classification, *Medical image computing and computer-assisted intervention : MICCAI ... International Conference on Medical Image Computing and Computer-Assisted Intervention* 17 (2014) 169–176.
- [16] H. Johansen-Berg, T. E. J. Behrens, M. D. Robson, I. Drobnjak, M. F. S. Rushworth, J. M. Brady, S. M. Smith, D. J. Higham, P. M. Matthews, Changes in connectivity profiles define functionally distinct regions in human medial frontal cortex, *Proceedings of the National Academy of Sciences of the United States of America* 101 (36) (2004) 13335–13340.
- [17] A. Morel, M. Magnin, D. Jeanmonod, Multiarchitectonic and stereotactic atlas of the human thalamus, *J. Comp. Neurol.* 387 (4) (1997) 588–630.
- [18] S. Mori, J. Zhang, Principles of diffusion tensor imaging and its applications to basic neuroscience research, *Neuron* 51 (5) (2006) 527–539.
- [19] C. Pierpaoli, P. J. Basser, Toward a quantitative assessment of diffusion anisotropy, *Magnetic Resonance in Medicine* 36.
- [20] J. Ashburner, K. J. Friston, Unified segmentation, *NeuroImage* 26 (3) (2005) 839–851.
- [21] H. J. Johnson, G. Harris, K. Williams, BRAINSFit : Mutual Information Registrations of Whole-Brain 3d Images, Using the Insight Toolkit.
- [22] B. Fischl, D. H. Salat, E. Busa, M. Albert, M. Dieterich, C. Haselgrove, A. van der Kouwe, R. Killiany, D. Kennedy, S. Klaveness, A. Montillo, N. Makris, B. Rosen, A. M. Dale, Whole brain segmentation : automated labeling of neuroanatomical structures in the human brain, *Neuron* 33 (3) (2002) 341–355.

-
- [23] B. Fischl, A. van der Kouwe, C. Destrieux, E. Halgren, F. Ségonne, D. H. Salat, E. Busa, L. J. Seidman, J. Goldstein, D. Kennedy, V. Caviness, N. Makris, B. Rosen, A. M. Dale, Automatically parcellating the human cerebral cortex, *Cerebral Cortex (New York, N.Y. : 1991)* 14 (1) (2004) 11–22.
- [24] I. Aganj, C. Lenglet, G. Sapiro, E. Yacoub, K. Ugurbil, N. Harel, Reconstruction of the orientation distribution function in single- and multiple-shell q-ball imaging within constant solid angle, *Magnetic Resonance in Medicine* 64 (2) (2010) 554–566.
- [25] M. Descoteaux, E. Angelino, S. Fitzgibbons, R. Deriche, Regularized, fast, and robust analytical Q-ball imaging, *Magnetic Resonance in Medicine* 58 (3) (2007) 497–510.
- [26] B. Whitcher, D. S. Tuch, J. J. Wisco, A. G. Sorensen, L. Wang, Using the wild bootstrap to quantify uncertainty in diffusion tensor imaging, *Human Brain Mapping* 29 (3) (2008) 346–362.
- [27] D. Wassermann, M. Descoteaux, R. Deriche, Diffusion maps clustering for magnetic resonance q-ball imaging segmentation, *International Journal of Biomedical Imaging* 2008 (2008) 526906.
- [28] M.-P. Dubuisson, A. Jain, A modified hausdorff distance for object matching, in : *Proceedings of the 12th IAPR International Conference, Vol. Vol. 1, 1994*, pp. 566 – 568 vol.1.
- [29] E. G. Jones, *The Thalamus*, Springer, 1985.
- [30] J. Q. Cordova, C. E. Pearson, On a modified streamline curvature method for the Euler equations, *Communications in Applied Numerical Methods* 4 (3) (1988) 327–333.
- [31] Y. B. Saalmann, Intralaminar and medial thalamic influence on cortical synchrony, information transmission and cognition, *Frontiers in Systems Neuroscience* 8 (2014) 83.
- [32] R. S. Swenson, *Review of Clinical and Functional Neuroscience*, Dartmouth Medical School, 2006.
- [33] V. A. Magnotta, S. Gold, N. C. Andreasen, J. C. Ehrhardt, W. T. Yuh, Visualization of subthalamic nuclei with cortex attenuated inversion recovery MR imaging, *NeuroImage* 11 (4) (2000) 341–346.
- [34] J. R. Hale, S. D. Mayhew, K. J. Mullinger, R. S. Wilson, T. N. Arvanitis, S. T. Francis, A. P. Bagshaw, Comparison of functional thalamic segmentation from seed-based analysis and ICA, *NeuroImage* 114 (2015) 448–465.
- [35] D.-J. Kim, B. Park, H.-J. Park, Functional connectivity-based identification of subdivisions of the basal ganglia and thalamus using multilevel independent component analysis of resting state fMRI, *Human Brain Mapping* 34 (6) (2013) 1371–1385.

Bibliography

- [36] D. Zhang, A. Z. Snyder, J. S. Shimony, M. D. Fox, M. E. Raichle, Noninvasive functional and structural connectivity mapping of the human thalamocortical system, *Cerebral Cortex* (New York, N.Y. : 1991) 20 (5) (2010) 1187–1194.
- [37] D. Eidelberg, A. M. Galaburda, Symmetry and asymmetry in the human posterior thalamus. I. Cytoarchitectonic analysis in normal persons, *Archives of Neurology* (6) (1982) 325–332.
- [38] L. M. Rimol, K. Specht, K. Hugdahl, Controlling for individual differences in fMRI brain activation to tones, syllables, and words, *NeuroImage* 30 (2) (2006) 554–562.
- [39] A. W. Toga, P. M. Thompson, Mapping brain asymmetry, *Nature Reviews. Neuroscience* 4 (1) (2003) 37–48.
- [40] M. Gut, A. Urbanik, L. Forsberg, M. Binder, K. Rymarczyk, B. Sobiecka, J. Kozub, A. Grabowska, Brain correlates of right-handedness, *Acta Neurobiologiae Experimentalis* 67 (1) (2007) 43–51.
- [41] P. S. Baumann, L. Cammoun, P. Conus, K. Q. Do, P. Marquet, D. Meskaldji, R. Meuli, J.-P. Thiran, P. Hagmann, High b-value diffusion-weighted imaging : a sensitive method to reveal white matter differences in schizophrenia, *Psychiatry Research* 201 (2) (2012) 144–151.
- [42] E. G. Jones, The thalamic matrix and thalamocortical synchrony, *Trends in Neurosciences* 24 (10) (2001) 595–601.
- [43] S. C. L. Deoni, M. J. C. Josseau, B. K. Rutt, T. M. Peters, Visualization of thalamic nuclei on high resolution, multi-averaged T1 and T2 maps acquired at 1.5 T, *Human Brain Mapping* 25 (3) (2005) 353–359.
- [44] C. R. Traynor, G. J. Barker, W. R. Crum, S. C. R. Williams, M. P. Richardson, Segmentation of the thalamus in MRI based on T1 and T2, *NeuroImage* 56 (3) (2011) 939–950.
- [45] S. Shipp, The functional logic of cortico-pulvinar connections., *Philosophical Transactions of the Royal Society B : Biological Sciences* 358 (1438) (2003) 1605–1624.
- [46] V. J. Wedeen, R. P. Wang, J. D. Schmahmann, T. Benner, W. Y. I. Tseng, G. Dai, D. N. Pandya, P. Hagmann, H. D’Arceuil, A. J. de Crespigny, Diffusion spectrum magnetic resonance imaging (DSI) tractography of crossing fibers, *NeuroImage* 41 (4) (2008) 1267–1277.
- [47] A. Abosch, E. Yacoub, K. Ugurbil, N. Harel, An Assessment of Current Brain Targets for Deep Brain Stimulation Surgery With Susceptibility-Weighted Imaging at 7 Tesla, *Neurosurgery* 67 (6) (2010) 1745–1756.
- [48] G. Battistella, J. Niederhauser, E. Fornari, L. Hippolyte, A. Gronchi Perrin, G. Lesca, F. Forzano, P. Hagmann, F. J. G. Vingerhoets, B. Draganski, P. Maeder, S. Jacquemont, Brain structure in asymptomatic FMR1 premutation carriers at risk for fragile X-associated tremor/ataxia syndrome, *Neurobiology of Aging* 34 (6) (2013) 1700–1707.

- [49] C. Ohye, Y. Higuchi, T. Shibasaki, T. Hashimoto, T. Koyama, T. Hirai, S. Matsuda, T. Serizawa, T. Hori, M. Hayashi, T. Ochiai, H. Samura, K. Yamashiro, Gamma knife thalamotomy for Parkinson disease and essential tremor : a prospective multicenter study, *Neurosurgery* 70 (3) (2012) 526–536.
- [50] E. G. Jones, Cortical development and thalamic pathology in schizophrenia, *Schizophrenia Bulletin* 23 (3) (1997) 483–501.

3

Evaluation of Thalamic Parcellation in Clinical Data

The work in this chapter represents a synthesis of three conference contributions presented as first author : 1. 23rd Annual Meeting and Exhibition of the International Society for Magnetic Resonance in Medicine (ISMRM) in 2015 as : **"Novel Robust Segmentation of the Thalamic Nuclei – Validation on Healthy Subjects and Patients"** with co-authors : E. Najdenovska, G. Battistella, C. Tuleasca, P. Maeder, A. Daducci, J.-P. Thiran, M. Levivier and M. Bach Cuadra (poster) ; 2. 22nd Annual Meeting of the Organization for Human Brain Mapping (OHBM) in 2016 as : **"Localization of the Vento-Intermediate Thalamic Nucleus Using Local Diffusion Properties"** with co-authors : E. Najdenovska, C. Tuleasca, X. Bresson, P. Maeder, G. Battistella, E. Formari, J. Regis, J.-P. Thiran, M. Levivier and M. Bach Cuadra (poster) ; 3. 13th International Stereotactic Radiosurgery Society (ISRS) congress in 2017 as **"Exploring Local Diffusion MRI Properties for Vim Localization : Evaluation in Clinical Cases"** with co-authors : E. Najdenovska, C. Tuleasca, J. Bloch, P. Maeder, N. Girard, T. Witjas, J. Regis, J.-P. Thiran, M. Bach Cuadra and M. Levivier (oral communication).

3.1 Introduction

The previous chapter presented the framework I propose for a robust and reproducible segmentation of thalamus in seven group of nuclei based on the Spherical Harmonic (SH) representation of the Orientation Distribution Function (ODF). This feature gives a full angular characterisation of the diffusion process in a voxel. The method is tested on a large HARDI datasets from 114 healthy subjects in total. It produced an equivalent outcome for both data obtained with different acquisition schemes and different 3 T scanners.

In this chapter, I extend the evaluation of the segmentation framework behaviour for 63 drug-

resistant tremor patients that were treated with GKS. The treatment target for all of them was the Vim determined by employing the quadrilateral of Guiot [8] (refer also to section 1.1.2 and figure 1.4(b)). For one-third of them, the follow-up data was also available allowing a validation of the motor-nuclei group against the observable contrast enhancement corresponding to the therapeutic target. Furthermore, to provide a more confined localization of the Vim in an automated manner, the group of motor nuclei was further subdivided.

3.2 Thalamic Parcellation in Drug-resistant Tremor Patients

The dataset included pre-operational images acquired several days before the GKS from 63 tremor patients (mean age : 71.7 ± 8.2) where 59 were treated at Marseille University Hospital (CHU Timone, France) and four at Lausanne University Hospital (CHUV, Switzerland). At CHUV, the data can be divided in two subsets with two patients each. The first included T1w (MPRAGE) images acquired at 1.5 T Aera Siemens (TR/TE=1910/3.01 ms, 176 slices, isotropic voxel of 1 mm^3) and DWI at 3T TimTrio Siemens scanner (72 gradient directions, TR/TE=6300/84 ms, b-value=1000s/mm², 52 slices and voxel-size : $2.24 \times 2.24 \times 2.2 \text{ mm}^3$). The second subset was acquired at 3T Prisma Siemens enclosing T1w (MPRAGE) images (TR/TE=2300/2.01 ms, TI=900 ms, 192 slices and isotropic voxel of 1 mm^3) and DWI (64 gradient directions, TR/TE=7100/84 ms, b-value=1000s/mm², 62 slices and voxel-size : $2.24 \times 2.24 \times 2.2 \text{ mm}^3$). The remaining data from CHU Timone was acquired with 3T Skyra Siemens using similar acquisition parameter as for the second CHUV dataset.

Following to the procedure described in the previous chapter, the DWI data underwent several preprocessing steps including : de-noising, motion and eddy-current correction. Furthermore the thalamic mask obtained initially from the FreeSurfer parcellation was also refined by excluding voxels from the CSF and the internal capsule. The ODF coefficient in the SH basis were obtained from the *Qboot* FSL function and finally the proposed modified k-means algorithm, subdividing the thalamus from the trade-off between the spatial position and the diffusion similarity distance, was applied. Please refer to Chapter 2 for more details.

The robust parcellation pattern previously observed in the healthy population was found again in 62 out of the 63 tested patient cases. The last case, for reasons that should be further

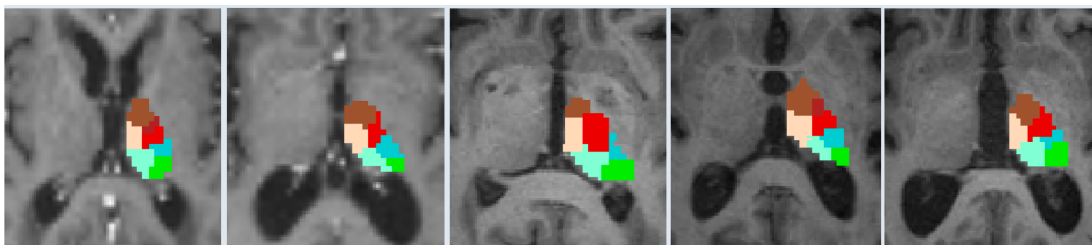


FIGURE 3.1 – Individual results of the thalamic nuclei segmentation in tremor patients showed in axial view and superposed on each respective pre-operational MPRAGE image

3.3. Validation of the Segmented Motor Group of Nuclei

explored, failed to provide the same spatial distribution of the resulting clusters. Figure 3.1 gives examples of the clustering outcome for several cases among the 62.

3.3 Validation of the Segmented Motor Group of Nuclei

For 18 out of the 63 patients, a follow-up data was available : for one patient at 3, for 12 at 6, for two at 9, and for four at 12 months after the surgery. The data included T1w (MPRAGE) images with enhanced contrast with injection of gadolinium. One of the CHUV patient was scanned on 3T Skyra Siemens (T1w acquisition parameters : TR/TE=1900/2.43 ms, TI=900 ms, voxel-size : 0.47x0.47.0.9 mm³), while the other on 3T Prisma Siemens (TR/TE=2300/2.01 ms, TI=900 ms and isotropic voxel of 1 mm). At CHU Timoine all 16 post-operative T1w were acquired with 3T Skyra Siemens (with TR/TE=1900/2.49 ms, TI=993 ms and isotropic voxels of 0.9 mm).

Although acquired at different stages, a contrast enhancement (CE) corresponding to the targeted area was observable for each patient and was further considered as a reference for evaluating the spatial distribution of the motor-related group of nuclei or here referred as the ventral latero-ventral cluster (VLV).

The correspondence between the DWI, where the thalamic subdivision was done, and the respective post-operative T1w was realised with a linear rigid transform [9]. This transformation was later used to propagate the delineated VLV into the post-operative T1w space.

For all 18 cases, the VLV contour always included inside the observable CE contrast (see figure 3.2) additionally confirming the spatial distribution of the proposed segmentation of the motor-related group of nuclei (the VLV cluster). Nevertheless, the size of the VLV was relatively bigger compared to the size of the observed CE, which was an expected outcome since the cluster encloses several other motor-related nuclei besides the Vim. Consequently, the next aim was to learn the localisation of the CE within the VLV by a further subdivision of that cluster. Exceptionally, in one patient the observable CE was exceeding the size of the VLV, therefore it was excluded from the following analysis.

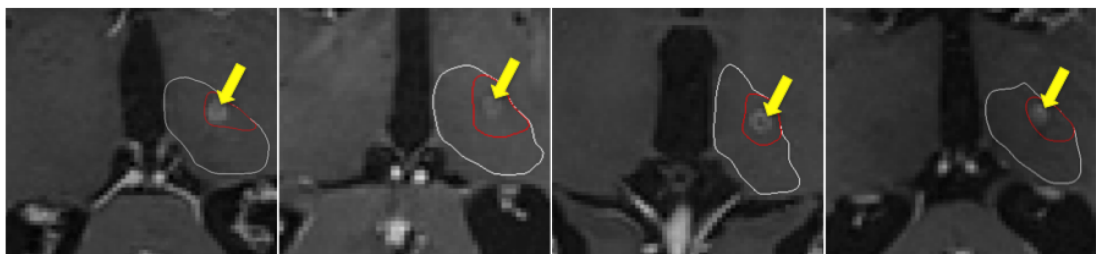


FIGURE 3.2 – Examples of the contrast enhancement (yellow fleashes) observed on the post-operative T1w images. Each panel show a different individual case in axial view. The white contour represents the thalamus, while the red one corresponds to the automatically segmented Ventral Latero-Ventral (VLV) nuclei group.

3.4 Graph-cut Partition of the Motor Group of Nuclei

3.4.1 Graph notions

A finite unidirectional graph $G = (V, E)$ is defined as a set of N vertices (V) also called nodes and set of edges (E) connecting respectively pair of vertices. An edge is characterised by a non-negative weight $w(i, j)$ reflecting the similarity between the linked nodes i and j . Subsequently, the $N \times N$ adjacency matrix A of a graph G is given as :

$$A_{ij} = \begin{cases} w(i, j), & \text{if } (i, j) \in E \\ 0, & \text{otherwise} \end{cases} \quad (3.1)$$

The degree of a vertex represents the sum of all weights of the edges incident to that vertex. If D is a $N \times N$ matrix containing the edges degree in its diagonal and zeros elsewhere, i.e. $D_{ii} = \sum_j A_{ij}$, the Laplacian of the graph is given by $L = D - A$ representing a real, symmetric, positive semi-definite matrix. In other words, the Laplacian eigenvalues λ_l are non-negative and the corresponding eigenvectors ϵ_l form an orthonormal basis. Consequently, for all $l = 0, \dots, N - 1$:

$$L\epsilon_l = (D - A)\epsilon_l = \lambda_l\epsilon_l \quad (3.2)$$

3.4.2 Graph partition

In the case of dividing the graph in two subsets A and B such as $A \cup B = V$ and $A \cap B = \emptyset$, the degree of dissimilarity between these sets is defined as the sum of the weights of the edges that have been removed to form the subgraphs. In graph theory it is also known as the *cut* :

$$cut(A, B) = \sum_{u \in A, v \in B} w(u, v) \quad (3.3)$$

Therefore, a minimisation of the *cut* value should give an optimal subdivision. Wu and Leahy [10] proposed to minimise the maximum inter-subgraphs cut thereby assuring minimisation of the similarity between clusters. This method is searching for a global optimal minimum, however is prone to fail in case of isolated vertices where its tendency is to segregate them in small subsets. Addressing this limitation, Shi and Malik [11] redefined the measure of disassociation as *normalized cut* (Ncut), which is the sum of ratios between the cut of the graph and the association of the subgraphs, the former representing the total connection from the subgraph nodes to all the nodes of the graph. Hence, for two partitions A and B the

normalized cut is given as :

$$Ncut(A, B) = \frac{cut(A, B)}{assoc(A, V)} + \frac{cut(A, B)}{assoc(B, V)} \quad (3.4)$$

which is no longer biased by isolated nodes.

The minimisation of the $Ncut$ can be transformed to minimization of the Rayleigh quotient [12]

$$r(y) = \frac{y^T (D - A)y}{y^T D y} \quad (3.5)$$

which is solved by its second smallest eigenvector and therefore, the corresponding eigenvalue is its minimum [11, 12]. In other words, for a bipartition of a graph the solution minimizing the $Ncut$ is the second smallest eigenvalue solving the generalised eigenvalue problem :

$$(D - A)y = \lambda D y \quad (3.6)$$

Accordingly, in the case of k partitions, where $V = \cup_{l=1}^k V_l$ and $V_m \cap V_n = \emptyset, \forall m \neq n$, the $Ncut$ disassociation criterium can be written as :

$$Ncut_k = \frac{cut(V_1, V - V_1)}{assoc(V_1, V)} + \frac{cut(V_2, V - V_2)}{assoc(V_2, V)} + \dots + \frac{cut(V_k, V - V_k)}{assoc(V_k, V)} \quad (3.7)$$

The top k eigenvalues could be then used to simultaneously solve such multi-partition [11]. The Multiclass Spectral Clustering [13] propose a discrete solution close to the continuous optima which is one of the first k leading eigenvectors. The outcome provided by this approach remains robust for any random initialisation [13].

3.4.3 VLV subdivision

Taking advantage of the graph partition, the VLV cluster was further divided in $Ncut$ segmentation framework. The aim was to explore only the diffusion information, therefore only the ODF coefficients in the SH basis were used as a feature for the subdivision.

The graph was build in k -nearest-neighbour (k -nn) mode. Its nodes were represented by the VLV voxels, while the edges by the respective Gaussian weighted function of the Euclidean

distance between the corresponding ODFs coefficients :

$$w(i, j) = e^{-\frac{\|ODF(i)-ODF(j)\|_2^2}{\sigma^2}} \quad (3.8)$$

where σ^2 is the variance of the ODF distances. The adjacency matrix was build in a way that each node was connected to its 10 nearest neighbour. An illustration of the graph is given in figure 3.3.

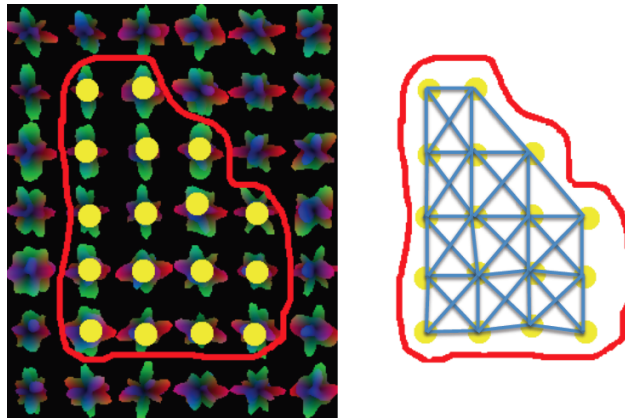


FIGURE 3.3 – Schematic representation of the build graph. With red is depicted the VLV cluster. On the left panel the VLV is superimposed on the ODF representation of the data illustrating the graph nodes (in yellow). The edges are depicted in blue in the right panel.

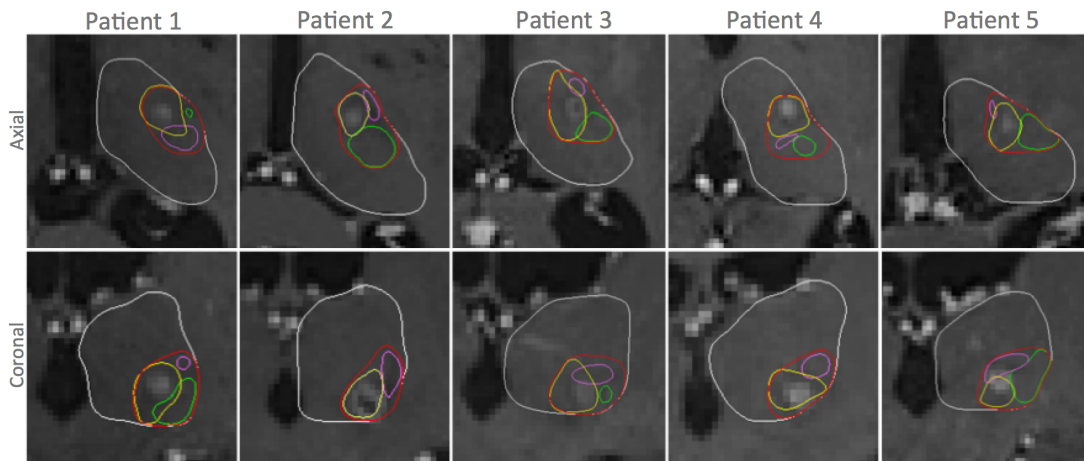


FIGURE 3.4 – Illustration of the VLV sub-partition. The white and the red contours represent the thalamus and the automatically segmented VLV nuclei group, respectively. The NCut sub-partitions are given in pink, yellow and green. The contrast enhancement (CE) corresponding to the GKS targeted area inside the yellow sub-cluster with an exception for Patient 5, which is an example where CE appears on the sub-partitions interface.

For each VLV of the 17 cases, the cluster was partitioned in three sub-clusters. The number

3 was empirically determined as the maximum number of clusters that gave a consistent subdivision pattern among the subjects.

The obtained subdivision was again with robust tendency overall the subjects. Moreover, it was qualitatively compared against the respective CE, which led to observe that for 12 out of 17 patients, one exclusive sub-cluster entirely covered the CE. In the remaining cases the CE was found either in the clusters interface or in another subdivision. Figure 3.4 gives a visual overview of the described results.

3.5 Study Extension on DBS data

The described VLV partition was also tested in additional data from drug-resistant tremor patients treated with bilateral DBS at CHUV. For both of them the pre-operative imaging protocol included T1w (MPRAGE) image (TR/TE=1900/2.43, TI=900 ms, isotropic voxels of 1 mm) and DWI (64 gradient directions, TR/TE=10300/84 ms, b-value=1000s/mm², voxel-size : 2.24x2.24x2.2mm³). All those sequences were acquired at 3T Skyra Siemens. Additionally, a post-operative Computer Tomography (CT) scan showing the implemented electrodes was available for both patients.

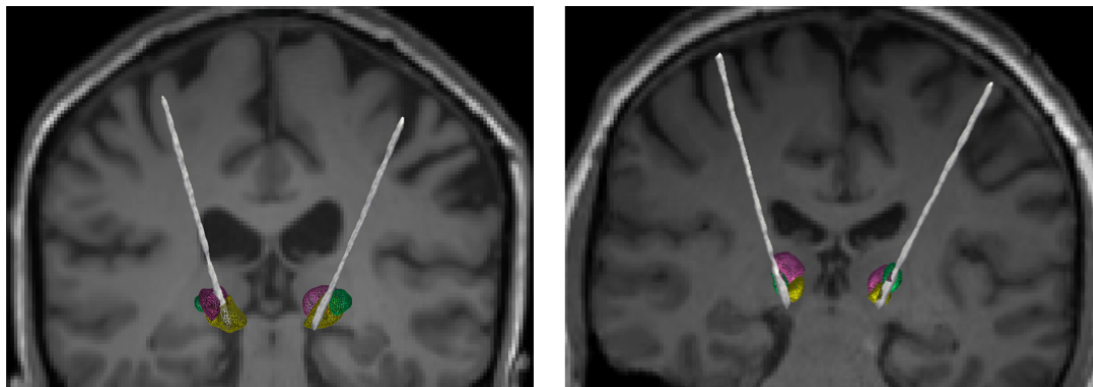


FIGURE 3.5 – Illustration of the VLV sub-partition in two drug-resistant tremor patients treated with DBS. One could observe that the final position of the implemented electrodes (in white) is always enclosed in the expected (yellow) VLV sub-cluster.

The treatment planning for both of the patients was done by employing the Medtronic DBS software for Vim targeting that rely also on landmarks information such as the AC-PC length and the width of the third ventricles. It should be however stated that while the Vim coordinates for the first patient were determined *blindly* i.e. as routinely done for this treatment, the lateral planning coordinates in the second case were adapted in accordance to the centroid of the anticipated VLV sub-cluster. Nevertheless, following the patients response during the surgery, in both cases the final electrodes position differed in 1 to 1.5 mm from the planning points. This is conforming the results from the previous studies showing that the difference between the “radiologically” obtained Vim and the “electrophysiologically” confirmed one could reach

up to 2 mm in approximately 35% and 1 mm in 65% of the treated cases [14]. Nevertheless, to unify and reinforce the stated conclusion, a bigger cohort should be explored.

The processing of the data was done following the described method in Chapter 2 and in section 3.4. The resulting partition of the thalamus and the sub-partition of the VLV cluster conformed the expected segmentation pattern respectively. Moreover, the VLV sub-cluster enclosing the CE in the tested GKS data contained the final electrodes position in these two cases (see figure 3.5).

3.6 Discussion

The work presented in this chapter extends the study of the proposed thalamic parcellation method to a large dataset of tremor patients. Although such data is prone to movement artefacts that could degrade the used imaging information, the clustering outcome demonstrated the method robustness in 98% of these cases.

One of the main drawbacks for the problematic of thalamic parcellation in the imaging field is the absence of an absolute reference for validation of the results. As previously mentioned, the standard MRI sequences lack in sufficient intrinsic contrast for distinguishing the anatomic thalamic subparts [15, 16]. In consequence, the validation of the state-of-the-art approaches, in general, is limited to a visual comparison with the available histological atlases [1, 7, 17, 18]. However, build upon a few species only, the atlases are restricted in enclosing the inter-subject variability [19] which weakness their reliability.

As the contrast enhancement (CE) appearing on the available follow-up data, was always inside VLV cluster, the presented study also showed an extended evaluation of the spatial allocation of the segmented group of motor nuclei. To the best of my knowledge, this analysis is a pioneer in validating an automatically delineated thalamic subpart with respect a clinical target.

From the proposed VLV subdivision, one exclusive sub-cluster was enclosing the CE in 71% of the tested cases giving the potential of this approach to outline a narrower spatial localisation of the Vim. These findings were further confirmed in two additional cases treated bilaterally with DBS where, differently from GKS, the treatment response and thereby, the confirmation of the targeting position, is immediate. Hence, an extension towards bigger tremor patient data could provide a possibility to predict the localisation of the target before the surgery.

The persistent VLV parcellisation pattern among the subject show that even at that size-level the segmentation is mainly driven by the diffusion information and not by the eventual noise in the data which, in general, behaves inconsistently. Nevertheless, the method limitations principally come from the relatively low spatial resolution of the explored DWI. An improved spatial resolution could lead to a finer subdivision not only of the VLV but the other thalamic subparts as well. Furthermore, as the diffusion signal not necessarily explain the underlying

histology of the tissue, but rather gives a complementary information, there is a need to include additional anatomical features for a better and more precise discrimination of the thalamic subparts.

3.7 Conclusion

The proposed method for thalamic nuclei segmentation remains robust even in clinical cases of patients with tremor that are likely to engender more motion artefacts. Moreover, with the target-related contrast enhancement appearing on the follow-up images always included inside the VLV cluster, this analysis gave also an extension towards a clinical validation regarding the spatial distribution of the segmented group of motor nuclei. The additional VLV subdivision showed tendency to restrain the localization of the targeted Vim area used for the treatment of drug-resistant tremor. The extension of this study on a bigger patient cohort could possibly lead to an automated prediction of the targeting position.

Bibliographie

- [1] M. R. Wiegell, D. S. Tuch, H. B. W. Larsson, V. J. Wedeen, Automatic segmentation of thalamic nuclei from diffusion tensor magnetic resonance imaging, *NeuroImage* 19 (2 Pt 1) (2003) 391–401.
- [2] Y. Duan, X. Li, Y. Xi, Thalamus segmentation from diffusion tensor magnetic resonance imaging, *International Journal of Biomedical Imaging* 2007 (2007) 90216.
- [3] L. Jonasson, P. Hagmann, C. Pollo, X. Bresson, C. Richero Wilson, R. Meuli, J.-P. Thiran, A level set method for segmentation of the thalamus and its nuclei in DT-MRI, *Signal Processing* 87 (2) (2007) 309–321.
- [4] L. Rittner, R. A. Lotufo, J. Campbell, G. B. Pike, Segmentation of thalamic nuclei based on tensorial morphological gradient of diffusion tensor fields, in : 2010 IEEE International Symposium on Biomedical Imaging : From Nano to Macro, 2010, pp. 1173–1176.
- [5] U. Ziyang, D. Tuch, C.-F. Westin, Segmentation of Thalamic Nuclei from DTI Using Spectral Clustering, in : Medical Image Computing and Computer-Assisted Intervention - MICCAI 2006, Lecture Notes in Computer Science, Springer, Berlin, Heidelberg, 2006, pp. 807–814.
- [6] U. Ziyang, C.-F. Westin, Joint Segmentation of Thalamic Nuclei from a Population of Diffusion Tensor MR Images, *Medical image computing and computer-assisted intervention : MICCAI International Conference on Medical Image Computing and Computer-Assisted Intervention* 11 (2008) 279–286.
- [7] S. C. Mang, A. Busza, S. Reiterer, W. Grodd, A. U. Klose, Thalamus segmentation based on the local diffusion direction : a group study, *Magnetic Resonance in Medicine* 67 (1) (2012) 118–126.
- [8] G. Guiot, J. Hardy, D. Albe-Fessard, G. Arfel, G. Vourc'h, E. Hertzog, P. Aleonard, Délimitation précise des structures sous-corticales et identification de noyaux thalamiques chez l'homme par l'électrophysiologie stéréotaxique, *Neurochirurgia* 5 (01) (1962) 1–18.
- [9] H. J. Johnson, G. Harris, K. Williams, BRAINSFit : Mutual Information Registrations of Whole-Brain 3d Images, Using the Insight Toolkit.
- [10] Z. Wu, R. Leahy, An optimal graph theoretic approach to data clustering : theory and its application to image segmentation, *IEEE Transactions on Pattern Analysis and Machine Intelligence* 15 (11) (1993) 1101–1113.
- [11] J. Shi, J. Malik, Normalized cuts and image segmentation, in : Proceedings of IEEE Computer Society Conference on Computer Vision and Pattern Recognition, 1997, pp. 731–737.

Bibliography

- [12] G. H. Golub, C. F. Van Loan, *Matrix Computations* (3rd Ed.), Johns Hopkins University Press, 1996.
- [13] S. X. Yu, J. Shi, Multiclass spectral clustering, in : *Proceedings Ninth IEEE International Conference on Computer Vision*, 2003, pp. 313–319 vol.1.
- [14] R. R. Tasker, L. W. Organ, P. A. Hawrylyshyn, *The Thalamus and Midbrain of Man : A Physiological Atlas Using Electrical Stimulation*, C.C. Thomas, 1982.
- [15] T. Gringel, W. Schulz-Schaeffer, E. Eloff, A. Frölich, P. Dechent, G. Helms, Optimized high-resolution mapping of magnetization transfer (MT) at 3 Tesla for direct visualization of substructures of the human thalamus in clinically feasible measurement time, *Journal of magnetic resonance imaging : JMRI* 29 (6) (2009) 1285–1292.
- [16] T. Tourdias, M. Saranathan, I. R. Levesque, J. Su, B. K. Rutt, Visualization of intra-thalamic nuclei with optimized white-matter-nulled MPRAGE at 7t, *NeuroImage* 84 (2014) 534–545.
- [17] T. E. J. Behrens, H. Johansen-Berg, M. W. Woolrich, S. M. Smith, C. a. M. Wheeler-Kingshott, P. A. Boulby, G. J. Barker, E. L. Sillery, K. Sheehan, O. Ciccarelli, A. J. Thompson, J. M. Brady, P. M. Matthews, Non-invasive mapping of connections between human thalamus and cortex using diffusion imaging, *Nature Neuroscience* 6 (7) (2003) 750–757.
- [18] S. C. L. Deoni, M. J. C. Josseau, B. K. Rutt, T. M. Peters, Visualization of thalamic nuclei on high resolution, multi-averaged T1 and T2 maps acquired at 1.5 T, *Human Brain Mapping* 25 (3) (2005) 353–359.
- [19] A. Morel, M. Magnin, D. Jeanmonod, Multiarchitectonic and stereotactic atlas of the human thalamus, *J. Comp. Neurol.* 387 (4) (1997) 588–630.

4

Comparison with 7 T Data

The work presented in this chapter is submitted for publication in Journal of Neurosurgery as **"Advanced Imaging of the Ventral Intermediate Thalamic Nucleus : A Proof of Concept"** with co-authors E. Najdenovska, C. Tuleasca, J. Jorge, P. Maeder, J. P. Marques, T. Roine, D. Gallichan, J.-P. Thiran, M. Levivier and M. Bach Cuadra. E. Najdenovska and C. Tuleasca have equally contributed to the present study. Preliminary results in the scope of this study were presented in an oral communication at the 13th International Stereotactic Radiosurgery Society (ISRS) congress in 2017 as **"Vim's Anatomical Landmarks : Indirect Targeting vs. Direct Visualization at 7T MRI"** with co-authors : E. Najdenovska, C. Tuleasca, J. P. Marques, J. Jorge, D. Gallichan, P. Maeder, J.-P. Thiran, M. Levivier and M. Bach Cuadra.

4.1 Introduction

The ventro-intermediate (Vim) nucleus is a part of the motor group of thalamic nuclei that, among with the antero-lateral subdivisions, acts as a relay between the basal ganglia, the cerebellum and the motor cortex [1]. It was initially defined by Guiot from electrophysiological recordings [2] and it's organized in a somatotopic manner, with the leg-area lying laterally and the face-area medially, measuring 2-4 mm in antero-posterior, 7-10 mm dorso-ventral and 4-6 mm medio-lateral [3].

The Vim is typically used as a target for treatment of drug-resistant tremor in functional-neurosurgery framework, such as deep brain stimulation (DBS), radiofrequency thalamotomy [4–7] or recently, the alternative minimally invasive techniques, Radiosurgery (RS) [8–10] and High Intensity Focused Ultrasound (HIFU) [11, 12].

The Vim cannot be directly visualized on current magnetic resonance (MR) sequences used routinely in clinical practice. The targeting methods are therefore indirect, employing atlases, stereotactic coordinates, or the quadrilateral of Guiot [8, 10, 13–15]. There is no consensus for a “gold standard” targeting method, thus providing variability among centers. This becomes particularly crucial for Vim RS and HIFU, which cannot rely on intraoperative target confirmation. Hence, there is a need of standardizing the targeting procedure.

Advanced MRI techniques can help in addressing Vim-targeting limitations. For instance, diffusion MRI (dMRI), describes more exquisite microstructure details, like the orientation of the fibres, which is different for each thalamic nucleus. Additionally, an emergent field is the study of thalamic subparts on ultra high-field MRI. Recently, Abosch et al. [16] suggested the possibility of a direct Vim visualization by using susceptibility weighted imaging (SWI) acquired at 7T that show an enhanced image contrast inside the thalamic area [16, 17].

In this study we aim to step forward in better identifying and localizing the Vim by comparing four different methods that define this nuclei : 1) The quadrilateral of Guiot as a routinely used clinical targeting method ; 2) The automated dMRI-based thalamic subdivision ; 3) the direct 7T-based visualization ; and 4) the atlas-based Vim outline. The first method is defining the Vim in a statistical manner based upon previous electrophysiological recordings, while the remaining reveals its anatomical structure. Being part of computer-assisted image-analysis techniques, the second and the fourth methods differ from the third one which underlies only on direct human-eye examination. Figure 4.1 shows an overview of these approaches.

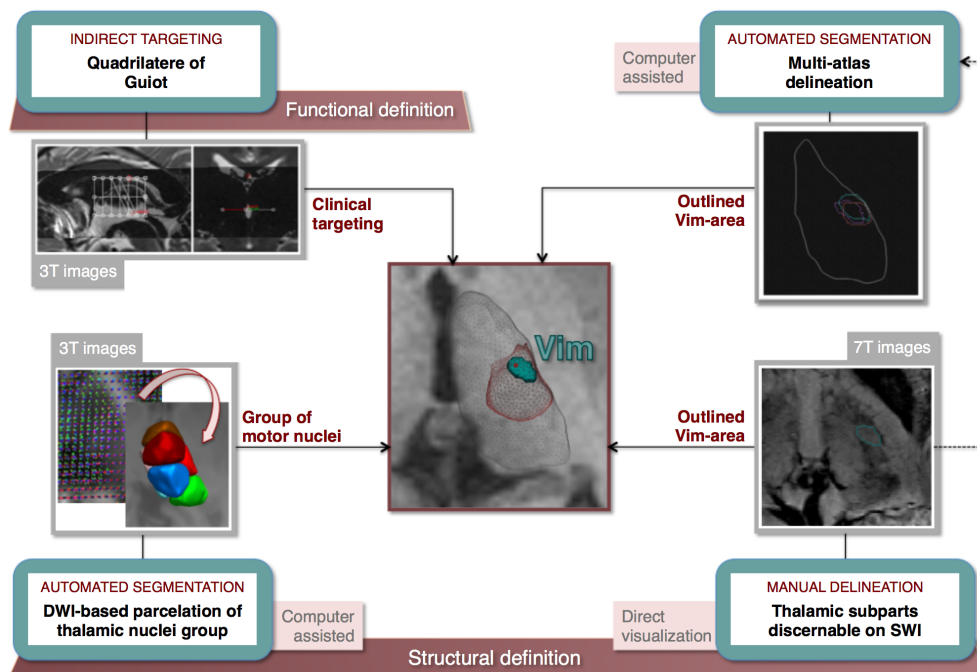


FIGURE 4.1 – Schematic overview of the methods used for defining the Vim

TABLE 4.1 – MRI protocol

Sequence	3 T T2-w	3 T T2-w CISS	3 T MPRAGE	3 T DWI	7 T MP2RAGE	7 T SWI
Resolution [mm ³]	0.5x0.5 x1.0	0.44x0.44 x0.44	1.0x1.0 x1.0	2.24x2.24 x2.2	0.6x0.6 x0.6	0.375x0.375 x1.0
Matrix size	512x512	320x320	256x256	98x98	256x320	512x512
Slices/ Partitions	160	80	160	52	320	72
Acquisition Time	4 min 43 s	8 min 08 s	4 min 1 s	9 min 10 s	10 min 38 s	7 min 30 s
TR [ms]	3200	6.18	2300	6300	6000	28
TE [ms]	402	2.75	2.98	84	2.64	20
TI [ms]	/	/	900	/	800/ 2700	/
Flip angles [degrees]	120	49	9	/	7/5	10
Target	Whole brain	Thalamus	Whole brain	Whole brain	Whole brain	Thalamus

4.2 Materials and Methods

4.2.1 Participants

Five healthy subjects (25 ± 2 years, two females, all right handed and with no particular brain disease and/or deformation caused by intracranial lesions) were scanned at both 3 T and 7 T. Local institutional review board approved the study and all participants gave written informed consent.

4.2.2 Image acquisitions

The acquisitions at 3 T (3T TIM-Trio SIEMENS scanner, 32-channel head coil) included the standard clinical Vim RS protocol : coronal T2-weighted (T2w), T2-weighted Constructive Interference Steady State (CISS)/Fiesta, T1-weighted (T1w, MPRAGE) and diffusion weighted images (DWI) acquired with 72 gradient directions and $b=1000 \text{ s/mm}^2$. At 7 T (68 cm-wide bore MRI system (SIEMENS Medical Solutions), 32-channel head coil (Nova Medical)) we acquired T1w MP2RAGE [18] and axial SWI. Acquisition parameters are given in table 4.1.

4.2.3 Common image space

The analyses, for each subject respectively, were performed in the individual anterior commissure - posterior commissure (AC-PC) image space. We first transformed the T2w into the AC-PC space by employing 3D Slicer [19] and choosing manually 30 brain mid-plane points. The resulting image was then used as a reference for the AC-PC alignment of the remaining sequences. More precisely, for each 3 T contrast, with the exception of the DWI, we performed a rigid-body transformation (six degrees of freedom, DOF). To correct the DWI Echo Planar

Imaging (EPI) distortion, we registered the fractional anisotropy map (FA) to the MPRAGE with a non-linear transform using FSL FNIRT [20, 21] (Analysis Group, FMRIB, Oxford, UK).

To overcome observed distortions in the frontal and the parietal cortex of the 7T data, we performed a 12-DOF linear transform between both skull-stripped 7T MP2RAGE and 3T MPRAGE. This transform was applied to the SWI rigidly (6-DOF) aligned beforehand to the corresponding MP2RAGE.

All registrations [22] were preformed with 100000 voxel samples and Mattes Mutual Information as cost function. The outcome quality was assessed by visual inspection of the matching between the ventricles.

Figure 4.2 summarizes the registration process. After being transformed to the AC-PC space, all images were resampled to the T2 CISS spatial resolution (0.44x0.44x0.44 mm³) using linear interpolation.

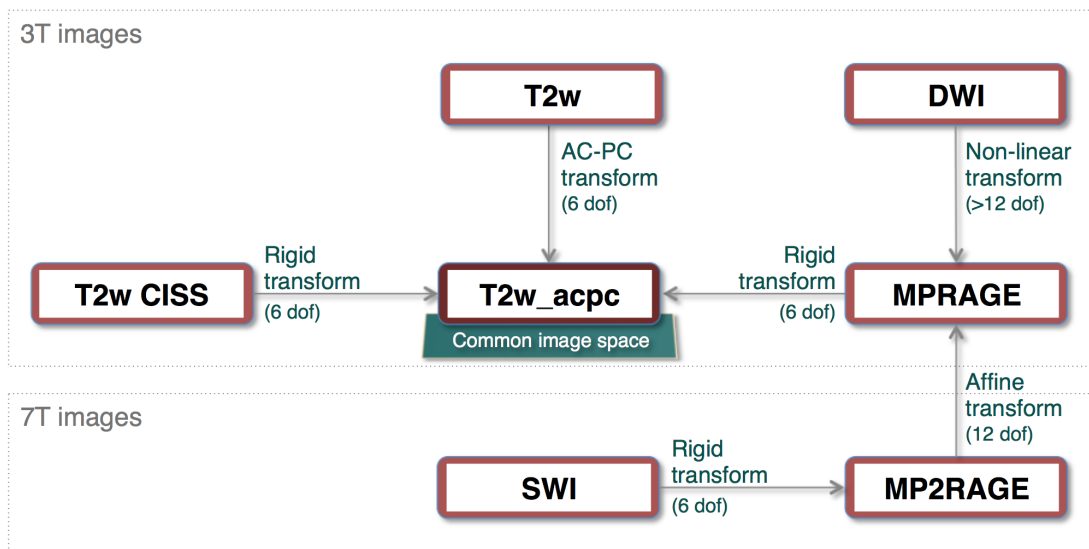


FIGURE 4.2 – Schematic overview of the registrations applied for transforming into the common image space

4.2.4 Targeting methods

Quadrilateral of Guiot

The quadrilatre of Guiot [2, 13] is defined upon anatomical landmarks, including AC, PC, thalamus height and third-ventricle lateral wall, all easily recognizable on T2 CISS. The final position is the Vim’s antero-inferior part, at 11 mm from the third-ventricle lateral border. An experienced neurosurgeon (CT) performed this targeting in MITK 3M3 (German Cancer Research Center, Heilderberg, Germany).

To test the reproducibility, Guiot targeting was performed six times for each subject, bilaterally and blindly. A sphere with 2 mm radius was drawn around each Guiot point to simulate both the 90 Gy isodose line and the contrast-enhanced area [23] visualized on follow-up MRI if a radiosurgical thalamotomy [24] would have been applied in the presented cases.

Automated 3T dMRI-based segmentation

Several research groups explored the dMRI advantages for automated thalamic subdivision [25–33]. The initial approaches are mainly based on diffusion tensor images i.e. a coarse diffusion representation. Recently, our group developed an approach [25] that relies on more detailed diffusion feature - the Spherical Harmonic (SH) representation of the Orientation Distribution Functions (ODFs) and outperforms the state-of-the-art methods by providing robust and reproducible segmentation pattern for a large dataset and different diffusion sequences. Our approach subdivides the thalamus in seven groups of nuclei corresponding to Morel's atlas [34] anatomy. One of the segmented groups of nuclei is the ventral latero-ventral cluster (VLV) enclosing the motor-related nuclei including the Vim (figure 4.3).

The DWI pre-processing included data denoising [35–37], bias field [20, 38], motion [39] and eddy current correction [40]. The SH coefficients of the constant solid angle ODFs of maximum order 6 were calculated using the FSL's `qboot` function [25].

The thalamic masks were initially obtained from the Freesurfer parcellation [41, 42] on each MPRAGE and redefined, as described by Battistella et al. [25], by eliminating the voxels having FA value greater than 0.55 or exceeding 5% probability to belong to the cerebrospinal fluid. The refined masks were further compared to the thalamic borders appearing more evident in SWI and consequently, for providing even more precise thalamic outline, several voxels were manually refined.

The thalamic subdivision was completed in the diffusion space of each subject and the resulting clusters were brought in the AC-PC space.

Additionally, as presented in section 3.4, the VLV cluster was further subdivided with NCut clustering [43] in three parts using only the ODF coefficients as a feature.

Manual Vim delineation on 7T SWI

SWI combines contrast from differences in effective transverse signal relaxation ($T2^*$) and in MR signal phase, both strongly affected by the magnetic susceptibility and the underlying tissue geometry [44, 45]. Accordingly, SWI has shown increased sensitivity, in respect to standard T1- or T2*w imaging, for visualizing deoxygenated blood vessels, vascular and axonal lesions, as well as calcium and iron depositions [46] and it allows better visualization of certain deep brain structures, including the thalamic subparts. Particularly, the Vim appears as a well-distinguishable hyper-intensity structure surrounded by darker regions [16] (figure 4.3A). This

is especially evident at higher magnetic field strengths, such as 7T, where the susceptibility-dependent contrast is more accentuated, and moreover, sub-millimeter spatial resolution can be easily achieved.

The manual delineation of the Vim on 7T SWI was primarily based upon the previous observations of Abosch et al. [16] and the Schaltenbrand and Wahren atlas [47] also used as reference in the mentioned study.

The thalamic lateral border and the internal capsule are well distinguishable on the 7T SWI. Referring to the Shaltenbrand's atlas, the Pulvinar as well is directly recognizable in the axial SWI plan (in green, figure 4.3A). Superior to it, again in axial plan, is the ventro-caudalus nucleus (Vc) appearing as a dark region (figure 4.3A, bright-violet) immediately posterior to a narrower zone with brighter image intensity that is considered as Vim (figure 4.3A, yellow). Above it, ventro-odalis (Vo) appears (figure 4.3A, bright-blue) as another dark area defining the superior border of the Vim. Additionally, the visualization of the medio-dorsal group allows the identification of the mesial Vim border.

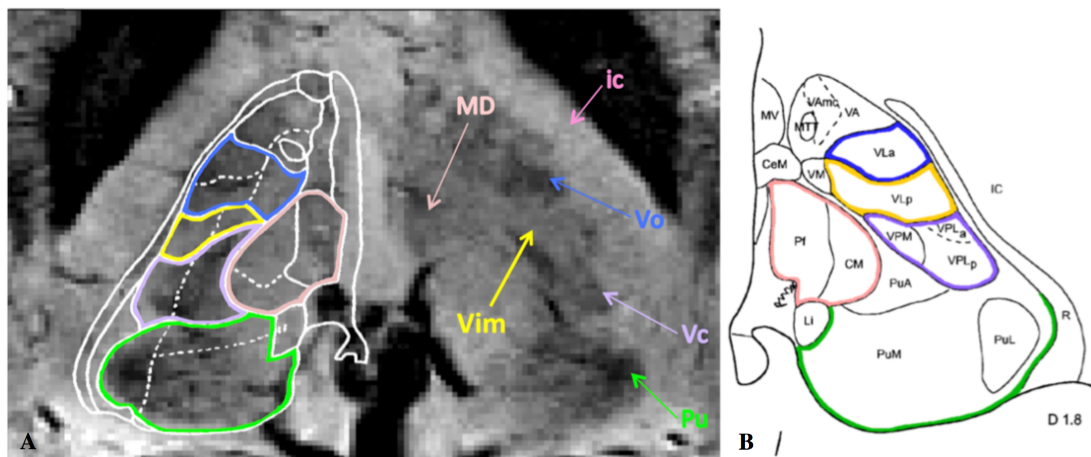


FIGURE 4.3 – Illustration of the visible structures corresponding to the thalamic area in axial view on the SWI acquired at 7T, based upon the illustration from the pioneering work of Abosch et al. [16]. In panel A the SWI features are compared with the Schaltenbrand atlas [47] (plate 53 Hd +3.5) superimposed on the right thalamus. The arrows and the respective color contours indicate the nuclei : Vim, Pulvinar (Pu), ventro-caudalus (Vc), ventro-odalis (Vo), the medio-dorsal group (MD) and the internal capsule (ic). The shown SWI image is part of the dataset used in this study. Panel B gives a corresponding axial plate of the Morel's atlas where the (same) color (shade) matches appropriate regions of the Schaltenbrand's atlas, while keeping the same nomenclature used in each one of them. In fact, considering the Morel's atlas [34] nomenclature, Vim is part of the Ventro-Lateral-posterior nuclei, which furthermore, together with ventro-lateral anterior and ventro-posterior nuclei form the VLV cluster.

Multi-atlas segmentation

One widely used state-of-the-art segmentation technique is the atlas-based registration, if an atlas is available. Having achieved the manual Vim outline, we considered each one of them as an atlas within a multi-atlas segmentation framework.

The framework was built in leave-one-out scenario, meaning that for each subject-target its own Vim outlines were not considered as atlases, but only those from the remaining subjects. The atlas registration was done in 2 steps. First, with an affine transform [22] we matched the respective MPRAGEs and we applied it to the corresponding SWI. Second, we perform a non-linear registration for a local correspondence using only the SWI as it gives more distinguishable thalamic features than the T1w, thus potentially allowing more accurate matching between the thalamic nuclei. To this end, we defined a volume of interest (VOI) surrounding the thalamus in which, in order to standardize the SWI intensities among all the subjects, we performed a histogram matching proposed by Nyúl et al. [48]. Non-rigid BSpline transform using maximum displacement of 1 mm [22] was computed in the VOI. The combination of both linear and non-linear transform was applied to the Vim outlines respectively and the final multi-atlas segmentation outcome was obtained by employing the Joint Label Fusion method with corrective learning [49].

4.2.5 Quantitative analyses

The intra-subject reproducibility of the Guiot targeting was estimated with the Euclidean distance between the six target points for each individual hemisphere, by taking as reference the first targeted point.

The volumes of the manual Vim and automatic VLV delineation were computed and normalized by the corresponding thalamic volume to ensure a relevant comparison across hemispheres and subjects.

The accuracy of the multi-atlas segmentation against the manual delineation was evaluated with Dice Coefficient [50] measuring their overlap. Overlap greater than 70% is considered as good match.

4.2.6 Qualitative analyses

The four investigated approaches provide outcomes at different size : from a single point to a group of nuclei. To better assess their spatial distribution, we further divided the VLV and the manually delineated Vim in eight geometrical sub-regions (figure 4.4). More specifically, for each region of interest (ROI), VLV or manual outline, we calculated the smallest rectangular cuboid containing all non-zero voxels whose mid-plane isolated the superior from the inferior part, while the in-plane diagonals the anterior, the lateral, the posterior and the ventral ROI part.

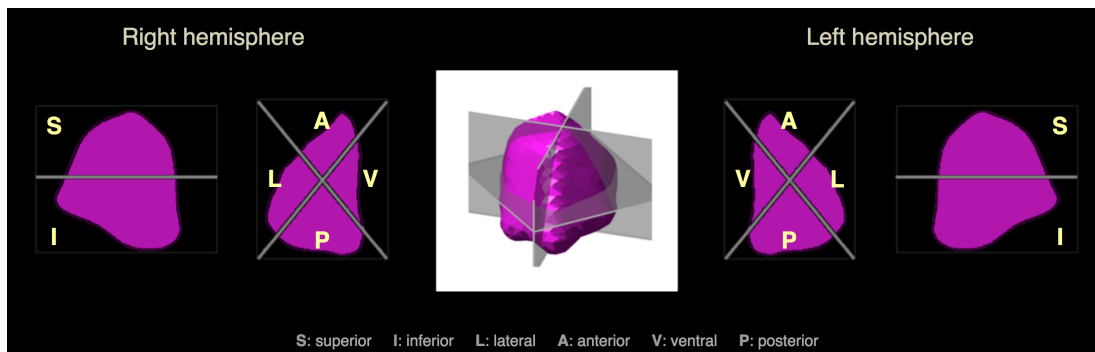


FIGURE 4.4 – Schematic representation of the ROIs separation in 8 regions in 2D and 3D view (middle). The labeling of the subparts is done according to the hemispheres to which the ROI belongs.

4.3 Results

4.3.1 Quadrilateral of Guiot

The obtained Guiot points were either overlapping or differing by one voxel. The maximum intra-subject difference was less than 1.3 mm, confirming to the targeting expectations of reproducibility (see the boxplots in figure 4.5).

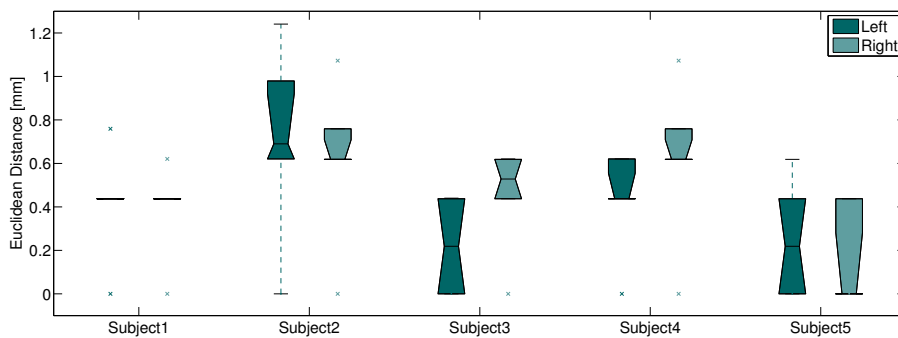


FIGURE 4.5 – Boxplot showing the difference between the six targeting points obtained by the quadrilateral of Guiot for each subject respectively

4.3.2 Automated 3T dMRI-based segmentation

For all subjects, we found similar segmentation pattern as previously reported for a larger cohort of 35 healthy subjects [25] (figure 4.6). Moreover, the VLV cluster represented the expected spatial extent and its volume was in the interval $[0.92, 1.27] \text{ cm}^3$ or 15-19% of the corresponding thalamic volume. Detailed values are reported in table 4.2.

TABLE 4.2 – The calculated volume of the manually delineated Vim and the VLV cluster. The presence of a blood vessel made impossible the manual delineation of the Subject 1’s right Vim (*).

Volume		Subject 1	Subject 2	Subject 3	Subject 4	Subject 5	
Manually delineated Vim	Left	mm ³	/(*)	76.3	83.3	82.8	67.2
		normalized	/(*)	1%	1.5%	1.1%	1%
	Right	mm ³	77.6	82	82.9	73	78.7
		normalized	1%	1.1%	1.2%	1.1%	1%
Automatically segmented VLV	Left	cm ³	1.1	1.3	1.1	1	1.2
		normalized	15%	17%	18%	14%	19%
	Right	cm ³	1	1.3	1.1	0.9	1
		normalized	14%	18%	16%	15%	15%

4.3.3 Manual Vim delineation on 7 T SWI

Both Vims were identified in four out of five subjects. In the fifth case, only the right Vim area was distinguishable, while on the left side, a blood vessel made difficult to discriminate any contrast difference that could have corresponded to the Vim (figures 4.6 and 4.7). Hence, in total, we had nine manually delineated Vims.

The manual delineation was nonetheless challenging and time-consuming, as the borders of the Vim were not unquestionably discernable due either to the lack of image intensity contrast or the presence of small blood vessels that sometimes could have been confounded with the surrounding nuclei. Moreover, the image intensity and its contrast variations differed between subjects (figure 4.7).

The manually delineated volumes were in the range [67.2, 83.3] mm³ and occupying 1-1.5% of the total thalamic volume (table 4.2).

4.3.4 Multi-atlas segmentation

To consider an equal contribution from both hemispheres, the subject with no manual left Vim outline was not considered for building the multi-atlas framework. Therefore, we used three Vim atlases per hemisphere.

The multi-atlas segmentation outlines were fairly comparable to the manual delineation (figure 4.8). The calculated Dice overlap was 35-64% for the left and 63-75% for the right hemisphere (table 4.3).

Chapitre 4. Comparison with 7 T Data

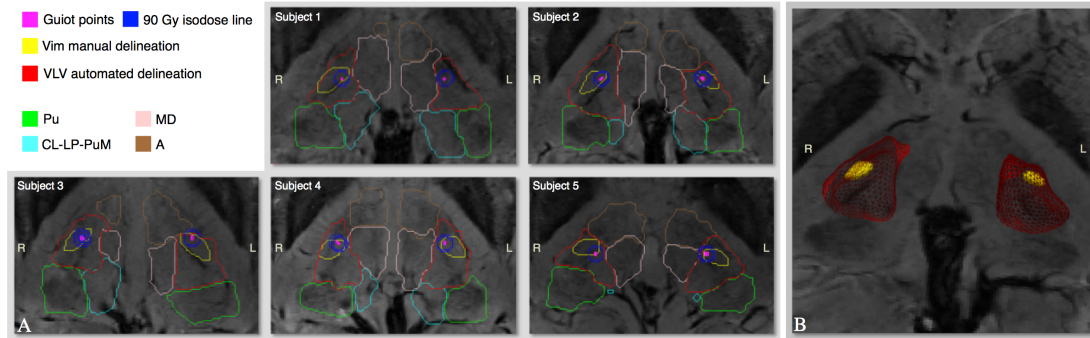


FIGURE 4.6 – Visual representation of the overall results. Panel A give the results in axial view of each subject respectively, while panel B shows a 3D view of the Subject 2 outlined Vim, as well as its localization inside the VLV cluster and within the thalamus. Among the shown findings, the Guiot points are given in magenta, the manual Vim delineation in yellow and the automatically segmented VLV cluster in red. The remaining automatically delineated clusters shown in panel A are : Pulvinar (Pu), medio-dorsal (MD) and the anterior (A) group of nuclei as well as the cluster enclosing the centro-lateral and the lateral posterior nuclei along with the medial part of the Pulvinar (CL-LP-PuM). It can be seen that for all the subjects the Guiot points are always inside and/or on the border of the manual delineation, which furthermore is observed in the anterior-lateral part of the VLV cluster close to its lateral border.

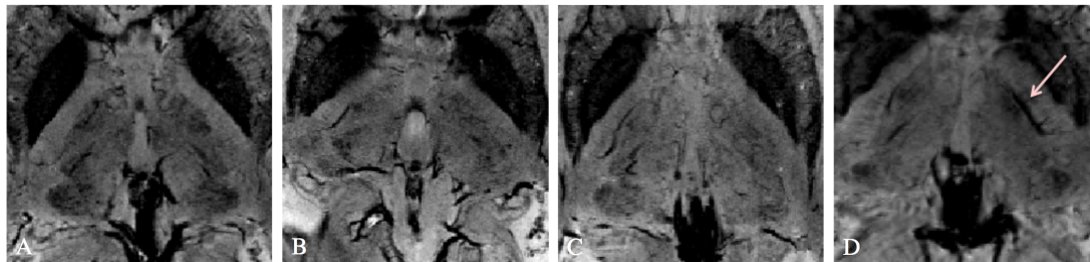


FIGURE 4.7 – Illustration of the difficulties encountered for the manual delineation of the Vim regarding the image contrast on SWI acquired at 7 T and the presence of blood vessels in the targeted area. We can observe that subjects in panel B and panel C do not present the same discriminative contrast variation around the expected Vim area in comparison with the subject shown in panel A. The arrow in panel D, corresponding to Subject 1, illustrates the relatively big blood vessel passing through the left targeted thalamic region that prevented manual discrimination of the Vim. The presence of small vessels surrounding the Vim can be observed in each panel.

TABLE 4.3 – The Dice Coefficient (DC) estimating the overlap between the multi-atlas Vim outline and the manual delineation

Subject	Subject 2		Subject 3		Subject 4		Subject 5	
	Left	Right	Left	Right	Left	Right	Left	Right
DC	64%	75%	42%	72%	35%	68%	35%	63%



FIGURE 4.8 – Visual comparison between the manual delineation and the multi-atlas outline of the Vim

4.3.5 Subdivision of the VLV cluster

The Ncut dMRI-based subdivision of the VLV cluster provided again, for all five subjects, the same sub-partition pattern as the one presented in the previous chapter (section 3.4). Considering the sub-cluster covering the contrast enhancement in the patients data, in this study for nine out of 10 thalami was enclosing the Guiot points and the simulated 90 Gy isodose lines. In the last thalamus the Guiot points were close to its border (see the right thalamus of Subject 1 in figure 4.9). However, the same sub-cluster does not enclose the entire manual Vim outline, but predominantly its anterior portion. All of these findings are illustrated in figure 4.9.

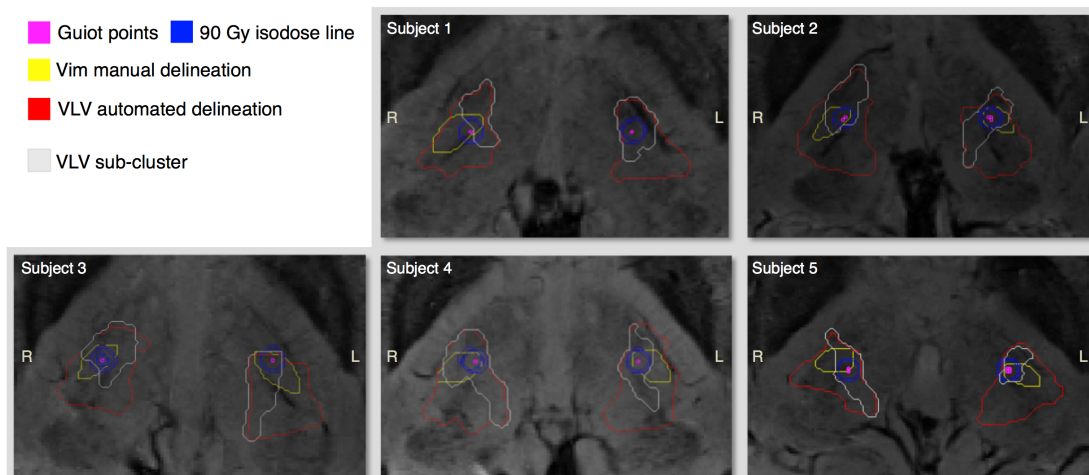


FIGURE 4.9 – Visual comparison between the VLV subcluster, the simulated clinical targeting and the manual Vim delineation

4.3.6 Qualitative comparison

The Guiot points were always inside or on the border of the manual delineation. The dMRI-based VLV cluster included always the manual Vim outline and therefore, the Guiot points as well. In average, the size of the VLV was 15-19 times bigger than the manual outline (see figure 4.6).

Considering the geometrical subdivision (figure 4.4), for seven out of nine cases the Guiot points were in the ventral part of the manual delineation. Additionally, these points were always in the inferior VLV partition, and with 80% rate in its anterior segment. For eight out of nine cases the manual Vim outline was found in the inferior VLV, in the ninth case being around the mid-plane. Furthermore, the manual outline was always next to the lateral VLV border and for eight out of nine cases lied in this cluster anterior/anterior-lateral part.

4.4 Discussion

With an aim of stepping forward to an improved targeting procedure, the presented study compares four different strategies for defining the Vim - a routinely used functional-neurosurgery target for treatment of drug-resistant tremor.

We observed that the clinical targeting points, defined by the quadrilateral of Guiot, are very likely to be found in a restrained area i.e. the ventral part of the manual Vim outline based on 7 T SWI. Representing only a point, Guiot targeting is however unable to define a full structural discrimination of the Vim. Nevertheless, the illustrative 90 Gy isodose lines were always inside the dMRI-based VLV cluster (figure 4.6).

The manual delineation is mainly confined within the VLV's inferior anterior-lateral division, which has anatomical relevance [34]. Moreover, this reveals a constrained area that most likely corresponds to the Vim within a region automatically delineated by computer-assisted image-analysis techniques, which has not been demonstrated previously.

The sub-cluster resulting from the proposed dMRI-based VLV subdivision conformed the expectations of encompassing the Guiot targeting and the simulated isodose of 90 Gy. However, this study showed that the sub-cluster is not including the entire outlined Vim. Hence, we could presume that further studies of this VLV subdivision, including bigger cohort and improved spatial resolution of the explored data, could potentially lead to narrower localization of the treatment target, but not necessarily to the Vim as a whole.

The manual delineation on the 7 T SWI data is however a time-consuming task as the Vim borders are not always obvious, mainly because of the presence of blood vessels, a low local image contrasts or contrast variability across subjects inside the thalamic area. In consequence, we assume having contour erring towards underestimation of the Vim extent. This is shown from the calculated volumes (table 4.2), which are near the lower limits of the known range [3]. Nevertheless, we provide more extensive Vim-focused analysis on 7 T data.

One limitation of the study comes from the studied population in terms of size and age. We are currently extending this study on data acquired from an elderly population, including healthy volunteers and patients with essential tremor. Preliminary analysis showed that the direct visualization of the Vim is more difficult comparing to the distinguishability in the healthy young population presented in this study.

Additional SWI analysis indicated that the image intensity contrast could also depend on the head orientation inside the scanner. This could be caused by anisotropic contributions to the local tissue susceptibility. For instance, white matter fibers have significantly anisotropic susceptibility [51]. Depending on the head orientation relative to the static MR field, the local susceptibility-based perturbations of the field may differ, and the resulting effects may thereby show significant changes in contrast. Anisotropic voxels may also add different partial volume effects depending on the head orientation. Thereupon, we would like to emphasize that even though 7 T SWI presents promising potential to improve the direct visualization [16], it cannot however be seen, with the current available technology, as a robust tool for easy and accurate Vim outline.

The proposed multi-atlas segmentation framework shows promising potential of delineating the Vim in automated manner. We assume that this segmentation quality is closely related to the use of SWI-features instead of T1w or T2w lacking in thalamic contrast variation. Consequently, when the 7 T SWI is available, it could be used as an alternative or as an initialization of a subject-related Vim segmentation, either manual or automated one. However, only three atlases were used, which limits the enclosed inter-subject variability. We expect improvement of the presented findings with an extension of the number of atlases to its optimum [52].

Although our main aim focuses on the Vim, this study also provides validation of the automated dMRI-based clustering against the directly visible SWI features. For example, in SWI the Pulvinar appears as the most-posterior distinguishable thalamic feature very dark laterally and brighter next to the ventricles (figure 4.3). Accordingly to previously reported findings [25], in figure 4.7 we see that the green Pu-cluster contour delineates mainly the darker nuclei part and a portion of medial Pulvinar (the brighter part) is enclosed in the CL-LP-PuM cluster. Furthermore, the spatial extent of the MD cluster coincides in general to the equivalent group of nuclei. All these findings support, above all, the spatial distribution of the VLV cluster.

The main limitation of the used dMRI-based subdivision method, as well as the other related state-of-the-art approaches, resides in the relatively low spatial resolution of the DWI data impeding both segmentation of finer thalamic subparts and accurate clusters borders regarding the SWI observable features.

Further studies on a larger dataset from subjects of broader age-scale should confirm the reported findings. However, given the potential of the automated dMRI-based segmentation and the direct visualization on 7 T SWI, both directly based on the individual anatomy, we suggest that their combination would further help to precisely and automatically define the exact Vim delineation.

4.5 Conclusion

The present study compares four different approaches for defining the Vim in healthy subjects. Although it was performed on a limited number of cases, we provide extensive analysis of the

Chapitre 4. Comparison with 7 T Data

directly distinguishable Vim-area on 7 T SWI and observe a restrained area corresponding to the Vim within a region automatically delineated in computer-assisted image-analysis techniques. Additionally, we propose a multi-atlas segmentation framework built in a multi-modal manner for an automated alternative of Vim delineation.

Bibliographie

- [1] J. Massion, The thalamus in the motor system, *Applied Neurophysiology* 39 (3-4) (1976) 222–238.
- [2] G. Guiot, J. Hardy, D. Albe-Fessard, G. Arfel, G. Vourc'h, E. Hertzog, P. Aleonard, Délimitation précise des structures sous-corticales et identification de noyaux thalamiques chez l'homme par l'électrophysiologie stéréotaxique, *Neurochirurgia* 5 (01) (1962) 1–18.
- [3] P. Tuite, A. Dagher (Eds.), *Magnetic Resonance Imaging in Movement Disorders : A Guide for Clinicians and Scientists*, 1st Edition, Cambridge University Press, Cambridge, 2013.
- [4] A. L. Benabid, P. Pollak, C. Gervason, D. Hoffmann, D. M. Gao, M. Hommel, J. E. Perret, J. de Rougemont, Long-term suppression of tremor by chronic stimulation of the ventral intermediate thalamic nucleus, *Lancet (London, England)* 337 (8738) (1991) 403–406.
- [5] S. Blond, D. Caparros-Lefebvre, F. Parker, R. Assaker, H. Petit, J. D. Guieu, J. L. Christiaens, Control of tremor and involuntary movement disorders by chronic stereotactic stimulation of the ventral intermediate thalamic nucleus, *Journal of Neurosurgery* 77 (1) (1992) 62–68.
- [6] M. S. Goldman, J. E. Ahlskog, P. J. Kelly, The symptomatic and functional outcome of stereotactic thalamotomy for medically intractable essential tremor, *Journal of Neurosurgery* 76 (6) (1992) 924–928.
- [7] P. R. Schuurman, D. A. Bosch, P. M. Bossuyt, G. J. Bonsel, E. J. van Someren, R. M. de Bie, M. P. Merkus, J. D. Speelman, A comparison of continuous thalamic stimulation and thalamotomy for suppression of severe tremor, *The New England Journal of Medicine* 342 (7) (2000) 461–468.
- [8] D. Kondziolka, J. G. Ong, J. Y. K. Lee, R. Y. Moore, J. C. Flickinger, L. D. Lunsford, Gamma Knife thalamotomy for essential tremor, *Journal of Neurosurgery* 108 (1) (2008) 111–117.
- [9] R. F. Young, F. Li, S. Vermeulen, R. Meier, Gamma Knife thalamotomy for treatment of essential tremor : long-term results, *Journal of Neurosurgery* 112 (6) (2010) 1311–1317.
- [10] C. Ohye, Y. Higuchi, T. Shibasaki, T. Hashimoto, T. Koyama, T. Hirai, S. Matsuda, T. Serizawa, T. Hori, M. Hayashi, T. Ochiai, H. Samura, K. Yamashiro, Gamma knife thalamotomy for Parkinson disease and essential tremor : a prospective multicenter study, *Neurosurgery* 70 (3) (2012) 526–536.
- [11] W. J. Elias, D. Huss, T. Voss, J. Loomba, M. Khaled, E. Zadicario, R. C. Frysinger, S. A. Sperling, S. Wylie, S. J. Monteith, J. Druzgal, B. B. Shah, M. Harrison, M. Wintermark, A pilot study of focused ultrasound thalamotomy for essential tremor, *The New England Journal of Medicine* 369 (7) (2013) 640–648.

Bibliography

- [12] N. Lipsman, M. L. Schwartz, Y. Huang, L. Lee, T. Sankar, M. Chapman, K. Hynynen, A. M. Lozano, MR-guided focused ultrasound thalamotomy for essential tremor : a proof-of-concept study, *The Lancet. Neurology* 12 (5) (2013) 462–468.
- [13] G. Guiot, S. Brion, M. Akerman, [stereotaxic anatomy of the internal pallidum, of the thalamus and of the internal capsule. studies of the individual variations. ii] 15 (1961) 703–41.
- [14] G. Guiot, D. Albe-Fessard, G. Arfel, E. Hertzog, G. Vourc'H, J. Hardy, P. Derome, P. Aleonard, [interpretation of the effects of thalamus stimulation in man by isolated shocks] 254 (1962) 3581–3.
- [15] A. Krauth, R. Blanc, A. Poveda, D. Jeanmonod, A. Morel, G. Székely, A mean three-dimensional atlas of the human thalamus : generation from multiple histological data, *NeuroImage* 49 (3) (2010) 2053–2062.
- [16] A. Abosch, E. Yacoub, K. Ugurbil, N. Harel, An Assessment of Current Brain Targets for Deep Brain Stimulation Surgery With Susceptibility-Weighted Imaging at 7 Tesla, *Neurosurgery* 67 (6) (2010) 1745–1756.
- [17] C. Lenglet, A. Abosch, E. Yacoub, F. D. Martino, G. Sapiro, N. Harel, Comprehensive in vivo Mapping of the Human Basal Ganglia and Thalamic Connectome in Individuals Using 7t MRI, *PLOS ONE* 7 (1) (2012) e29153.
- [18] J. P. Marques, T. Kober, G. Krueger, W. van der Zwaag, P.-F. Van de Moortele, R. Gruetter, MP2Rage, a self bias-field corrected sequence for improved segmentation and T1-mapping at high field, *NeuroImage* 49 (2) (2010) 1271–1281.
- [19] A. Fedorov, R. Beichel, J. Kalpathy-Cramer, J. Finet, J.-C. Fillion-Robin, S. Pujol, C. Bauer, D. Jennings, F. Fennessy, M. Sonka, J. Buatti, S. Aylward, J. V. Miller, S. Pieper, R. Kikinis, 3d Slicer as an image computing platform for the Quantitative Imaging Network, *Magnetic Resonance Imaging* 30 (9) (2012) 1323–1341.
- [20] S. M. Smith, M. Jenkinson, M. W. Woolrich, C. F. Beckmann, T. E. J. Behrens, H. Johansen-Berg, P. R. Bannister, M. De Luca, I. Drobnjak, D. E. Flitney, R. K. Niazy, J. Saunders, J. Vickers, Y. Zhang, N. De Stefano, J. M. Brady, P. M. Matthews, Advances in functional and structural MR image analysis and implementation as FSL, *NeuroImage* 23 Suppl 1 (2004) S208–219.
- [21] J. L. R. Andersson, M. Jenkinson, S. Smith, J. L. R. Andersson, M. Jenkinson, S. Smith, J. L. R. Andersson, P. a. E. S. Smith, J. L. Andersson, S. D. Smith, Non-Linear Registration aka Spatial Normalisation FMRIB Technial Report TR07ja2.
- [22] H. J. Johnson, G. Harris, K. Williams, BRAINSFit : Mutual Information Registrations of Whole-Brain 3d Images, Using the Insight Toolkit.

- [23] C. Tuleasca, E. Pralong, E. Najdenovska, M. B. Cuadra, J. R. F. Marques, F. Vingerhoets, J. Régis, J. Bloch, M. Levivier, Deep brain stimulation after previous gamma knife thalamotomy of the Vim for essential tremor is feasible! Clinical, electrophysiological and radiological findings, *Acta Neurochirurgica* 159 (7) (2017) 1371–1373.
- [24] A. M. Campbell, J. Glover, V. L. S. Chiang, J. Gerrard, J. B. Yu, Gamma knife stereotactic radiosurgical thalamotomy for intractable tremor : a systematic review of the literature, *Radiotherapy and Oncology : Journal of the European Society for Therapeutic Radiology and Oncology* 114 (3) (2015) 296–301.
- [25] G. Battistella, E. Najdenovska, P. Maeder, N. Ghazaleh, A. Daducci, J.-P. Thiran, S. Jacquemont, C. Tuleasca, M. Levivier, M. Bach Cuadra, E. Fornari, Robust thalamic nuclei segmentation method based on local diffusion magnetic resonance properties, *Brain Structure & Function* 222 (5) (2017) 2203–2216.
- [26] T. E. J. Behrens, H. Johansen-Berg, M. W. Woolrich, S. M. Smith, C. a. M. Wheeler-Kingshott, P. A. Boulby, G. J. Barker, E. L. Sillery, K. Sheehan, O. Ciccarelli, A. J. Thompson, J. M. Brady, P. M. Matthews, Non-invasive mapping of connections between human thalamus and cortex using diffusion imaging, *Nature Neuroscience* 6 (7) (2003) 750–757.
- [27] L. Jonasson, P. Hagmann, C. Pollo, X. Bresson, C. Richero Wilson, R. Meuli, J.-P. Thiran, A level set method for segmentation of the thalamus and its nuclei in DT-MRI, *Signal Processing* 87 (2) (2007) 309–321.
- [28] S. C. Mang, A. Busza, S. Reiterer, W. Grodd, A. U. Klose, Thalamus segmentation based on the local diffusion direction : a group study, *Magnetic Resonance in Medicine* 67 (1) (2012) 118–126.
- [29] J. O’Muircheartaigh, C. Vollmar, C. Traynor, G. J. Barker, V. Kumari, M. R. Symms, P. Thompson, J. S. Duncan, M. J. Koepp, M. P. Richardson, Clustering probabilistic tractograms using independent component analysis applied to the thalamus, *NeuroImage* 54 (3) (2011) 2020–2032.
- [30] L. Rittner, R. A. Lotufo, J. Campbell, G. B. Pike, Segmentation of thalamic nuclei based on tensorial morphological gradient of diffusion tensor fields, in : 2010 IEEE International Symposium on Biomedical Imaging : From Nano to Macro, 2010, pp. 1173–1176.
- [31] J. V. Stough, J. Glaister, C. Ye, S. H. Ying, J. L. Prince, A. Carass, Automatic method for thalamus parcellation using multi-modal feature classification, *Medical image computing and computer-assisted intervention : MICCAI ... International Conference on Medical Image Computing and Computer-Assisted Intervention* 17 (2014) 169–176.
- [32] M. R. Wiegell, D. S. Tuch, H. B. W. Larsson, V. J. Wedeen, Automatic segmentation of thalamic nuclei from diffusion tensor magnetic resonance imaging, *NeuroImage* 19 (2 Pt 1) (2003) 391–401.

Bibliography

- [33] U. Ziyan, D. Tuch, C.-F. Westin, Segmentation of Thalamic Nuclei from DTI Using Spectral Clustering, in : Medical Image Computing and Computer-Assisted Intervention – MICCAI 2006, Lecture Notes in Computer Science, Springer, Berlin, Heidelberg, 2006, pp. 807–814.
- [34] A. Morel, M. Magnin, D. Jeanmonod, Multiarchitectonic and stereotactic atlas of the human thalamus, *J. Comp. Neurol.* 387 (4) (1997) 588–630.
- [35] J.-D. Tournier, F. Calamante, A. Connelly, Mrtrix : Diffusion tractography in crossing fiber regions, *International Journal of Imaging Systems and Technology* 22 (1) (2012) 53–66.
- [36] J. Veraart, E. Fieremans, D. S. Novikov, Diffusion mri noise mapping using random matrix theory, *Magnetic Resonance in Medicine* 76 (5) (2016) 1582–1593.
- [37] J. Veraart, D. S. Novikov, D. Christiaens, B. Ades-Aron, J. Sijbers, E. Fieremans, Denoising of diffusion MRI using random matrix theory, *NeuroImage* 142 (2016) 394–406.
- [38] Y. Zhang, M. Brady, S. Smith, Segmentation of brain MR images through a hidden Markov random field model and the expectation-maximization algorithm, *IEEE transactions on medical imaging* 20 (1) (2001) 45–57.
- [39] A. Leemans, D. K. Jones, The B-matrix must be rotated when correcting for subject motion in DTI data, *Magnetic Resonance in Medicine* 61 (6) (2009) 1336–1349.
- [40] J. L. R. Andersson, S. N. Sotiropoulos, An integrated approach to correction for off-resonance effects and subject movement in diffusion MR imaging, *NeuroImage* 125 (2016) 1063–1078.
- [41] B. Fischl, D. H. Salat, E. Busa, M. Albert, M. Dieterich, C. Haselgrove, A. van der Kouwe, R. Killiany, D. Kennedy, S. Klaveness, A. Montillo, N. Makris, B. Rosen, A. M. Dale, Whole brain segmentation : automated labeling of neuroanatomical structures in the human brain, *Neuron* 33 (3) (2002) 341–355.
- [42] B. Fischl, A. van der Kouwe, C. Destrieux, E. Halgren, F. Ségonne, D. H. Salat, E. Busa, L. J. Seidman, J. Goldstein, D. Kennedy, V. Caviness, N. Makris, B. Rosen, A. M. Dale, Automatically parcellating the human cerebral cortex, *Cerebral Cortex (New York, N.Y. : 1991)* 14 (1) (2004) 11–22.
- [43] J. Shi, J. Malik, Normalized cuts and image segmentation, in : Proceedings of IEEE Computer Society Conference on Computer Vision and Pattern Recognition, 1997, pp. 731–737.
- [44] E. M. Haacke, Y. Xu, Y.-C. N. Cheng, J. R. Reichenbach, Susceptibility weighted imaging (SWI), *Magnetic Resonance in Medicine* 52 (3) (2004) 612–618.
- [45] E. M. Haacke, S. Mittal, Z. Wu, J. Neelavalli, Y.-C. N. Cheng, Susceptibility-Weighted Imaging : Technical Aspects and Clinical Applications, Part 1, *American Journal of Neuro-radiology* 30 (1) (2009) 19–30.

- [46] S. Mittal, Z. Wu, J. Neelavalli, E. Haacke, Susceptibility-Weighted Imaging : Technical Aspects and Clinical Applications, Part 2, *AJNR. American journal of neuroradiology* 30 (2) (2009) 232–252.
- [47] G. Schaltenbrand, W. Wahren, *Atlas for Stereotaxy of the Human Brain*, Thieme, 1977.
- [48] L. G. Nyúl, J. K. Udupa, X. Zhang, New variants of a method of MRI scale standardization, *IEEE transactions on medical imaging* 19 (2) (2000) 143–150.
- [49] H. Wang, P. A. Yushkevich, Multi-atlas segmentation with joint label fusion and corrective learning - an open source implementation, *Frontiers in Neuroinformatics* 7.
- [50] L. R. Dice, Measures of the Amount of Ecologic Association Between Species, *Ecology* 26 (3) (1945) 297–302.
- [51] S. Wharton, R. Bowtell, Effects of white matter microstructure on phase and susceptibility maps, *Magnetic Resonance in Medicine* 73 (3) (2015) 1258–1269.
- [52] J. Van de Velde, J. Wouters, T. Vercauteren, W. De Gerssem, E. Achten, W. De Neve, T. Van Hoof, Optimal number of atlases and label fusion for automatic multi-atlas-based brachial plexus contouring in radiotherapy treatment planning, *Radiation Oncology (London, England)* 11.

5

Multi-modal segmentation of the Vim

This chapter represents an extension of the work peer-reviewed and presented as an oral communication in the CLIP workshop of the 20th International Conference on Medical Image Computing and Computer Assisted Intervention (MICCAI) in September 2017. The corresponding 10-pages paper is published in the journal Lecture Notes in Computer Science, as part of the proceedings of MICCAI 2017, entitled as "**Towards an Automated Segmentation of the Ventro-intermediate Thalamic Nucleus**" with co-authors E. Najdenovska, C. Tuleasca, J. Jorge, P. Maeder, J.-P. Thiran, M. Levivier and M. Bach Cuadra.

5.1 Introduction

As shown in chapter 2, in the field of an automated thalamic parcellation, I proposed a robust and reproducible method that subdivides the thalamus in seven groups of nuclei using local diffusion properties expressed by the Orientation Distribution Functions (ODFs) in the Spherical Harmonic (SH) basis, which is outperforming the most advanced diffusion features so far [1]. One of the segmented clusters represents the ventral latero-ventral (VLV) thalamic part, i.e. the motor-related group of nuclei including the ventro-intermediate nucleus (Vim). The Vim cannot, however, be accurately depicted with diffusion MRI, for instance as a separate component of VLV, mainly due to the relatively low spatial resolution of the standard DWI (in general $\sim 2x2x2mm^3$).

On the other hand, as discussed in chapter 4, the susceptibility mapping approaches at ultra-high field (7 T) provide an improved intensity-contrast variation inside the thalamus. Moreover, Abosch et al. have indicated the correspondence of the observed features on susceptibility-weighted imaging (SWI) acquired at 7 T with the thalamic anatomy [2] and subsequently they

suggested the possibility of a direct visualization of the Vim on those images. Chapter 4 give more extensive analysis focused on the visually distinguishable Vim on 7 T SWI and show a tendency of the Vim to be found in the antero-lateral part of the automatically delineated VLV cluster.

Hence, the aim of this chapter is to automatically segment the Vim by combining SWI information at ultra-high field and the prior knowledge of the Vim localization inside the VLV group of nuclei. More specifically, the designed method combines NCut graph segmentation based on SWI intensity with a high-probability map of Vim localization derived from diffusion MRI thalamic clustering. Figure 5.1 shows a workflow of the proposed framework.

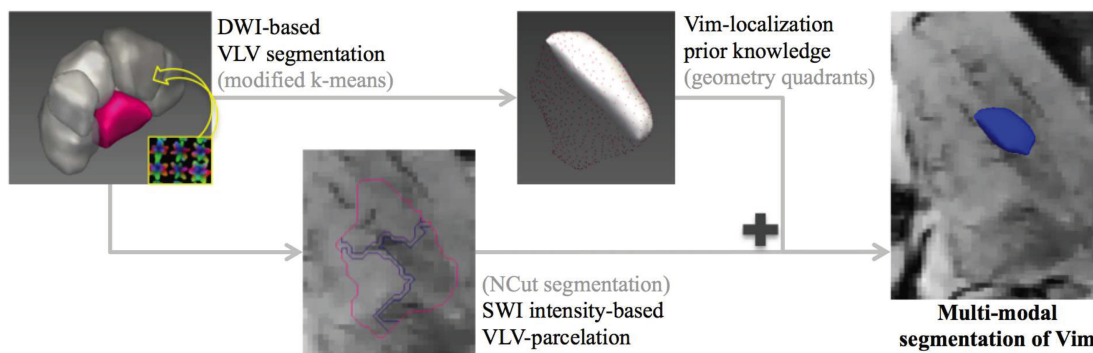


FIGURE 5.1 – Schematic overview of the proposed framework

5.2 Materials and Methods

5.2.1 Dataset

The study is performed in a dataset acquired at both 3 and 7 T from four healthy elderly subjects (mean \pm std : 67.2 ± 9.5 years, 3 males) and four healthy young subjects (28.5 ± 2.6 years, 2 males). None of the subjects had any particular neurological disease nor a brain deformation caused by intracranial lesions. The study was approved by the local institutional review board and an informed consent was obtained from all the participants.

In the further text, the elderly subjects will be also referred as ES1, ES2, ES3 and ES4, while the young cohort, representing Subject 2 - Subject 5 presented in chapter 4, all with manual delineation of both Vims, as YS2, YS3, YS4 and YS5.

Image Acquisitions

The data from elderly subjects at 3 T was acquired with a Prisma Siemens scanner and it included a T1-weighted (T1w, MPRAGE) sequence (TR/TE=2300/2.03 ms, TI=900 ms, voxel size : 1 mm^3) and DWI (64 gradient directions, $b=1000 \text{ s/mm}^2$, TR/TE=7100/84 ms, voxel-size : $2.24 \times 2.24 \times 2.2 \text{ mm}^3$). T1w images from the healthy young population were acquired with

3T TIM Trio Siemens scanner with similar acquisition parameters as those for the elderly population (also described in section 4.2.2).

For all eight subjects, the ultra-high field data was acquired with a 7 T, 68 cm-wide bore MRI system from SIEMENS Medical Solutions, equipped with a single-channel transmit / 32-channel receive head RF array (Nova Medical). This data included axial SWI (with a restrained field of view, FoV, surrounding the thalamus, TR/TE=28/20 ms, flip-angle 10°, voxel-size : 0.375x0.375x1 mm³, 72 slices) and T1w (MP2RAGE) sequence (TR/TE=6000/2.05 ms, T11/T12=800/2700 ms, flip-angles : 7/5°, voxel-size : 0.6x0.6x0.6 mm³).

5.2.2 Common Image Space

We choose to work in the individual anterior commissure-posterior commissure (AC-PC) image space of each subject. For the elderly cohort, the image space was defined by the T1 template in MNI space of voxel size 0.5x0.5x0.5 mm³ [3] whose AC-PC plane was aligned horizontally. Each 3T MPRAGE was transformed into this AC-PC space by a rigid transform, and the individual resulting image, T1w_acpc, was considered as reference for the successive image transformations described in the following sections.

For the young cohort, as reference was taken the corresponding T2w image brought into AC-PC with 3D Slicer [4] space by using 30 manually selected mid-brain points. The procedure is described in details in section 4.2.3.

5.2.3 Thalamic Parcellation

The preprocessing of the DWI included several steps : data denoising [5–7], bias field [8, 9], motion [10] and eddy current corrections [11]. Furthermore, with a non-linear registration, using FSL's FNIRT [8], between the T1w_acpc and the respective fractional anisotropy (FA) map, we compensated the EPI distortions presented in the DWI data. On the preprocessed data we performed the QBI fitting of the Constant Solid Angle ODFs (FSL qboot) with maximum SH order of 6, accordingly to [1].

The thalamus masks were obtained from the FreeSurfer's subcortical parcellation, performed for each 3 T MPRAGE, and further refined, as described in [1], by automatically removing voxels with FA value greater than 0.55 and cerebro-spinal fluid's probability exceeding 5%. Subsequently to a qualitative comparison between the re-fined masks and the SWI where the thalamic borders appear more discernible, missing voxels were manually added mainly in the anterior and the lateral part of the inferior thalamic slices.

Following the framework description in [1], the thalamus was subdivided in seven clusters by applying a modified k-means using as features the spatial position of the thalamic voxels and the corresponding ODF coefficients in the SH basis. The obtained results, including the VLV cluster were then brought in the AC-PC space by applying the non-linear transform, as

described earlier, matching the FA and T1w_acpc image.

5.2.4 The Proposed Framework

The VLV cluster, other than Vim, includes several motor-related nuclei. However, in correspondence to the findings described in [2] and the previous chapter (section 4.2.4), in SWI, the ventral nuclei surrounding the Vim, such as ventro-caudalis (Vc) and ventro-odalis (Vo), appear as darker regions in comparison with our area of interest (see figure 5.2). Relating to the observed contrast differences inside the VLV, the aim was to explore the SWI-intensity for a further VLV subdivision aiming towards an automated delineation of the Vim.

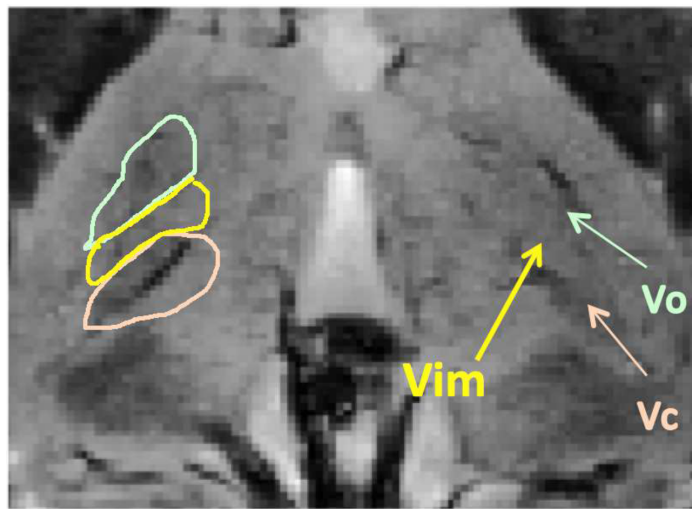


FIGURE 5.2 – Illustration of the SWI visible structures surrounding the Vim in axial view. On the right side we have manually in-plane draw of the visible ventral nuclei in correspondence with the Schaltenbrand and Wahren atlas [12], while on the left they are indicated with arrows. The yellow represents the Vim, while the bright green and the bright orange ventro-caudalis (Vc) and ventro-odalis (Vo), which are surrounding the Vim as darker areas.

SWI Preprocessing

The SWI were corrected for intensity inhomogeneities using the N4ITK bias field correction algorithm [13]. Accordingly to the procedure described in section 4.2.3, the obtained images were first registered to the corresponding 7T MP2RAGE with a rigid transform and then brought to the AC-PC space by applying the analogous affine transform that matched the 7T MP2RAGE and T1w_acpc.

Primary analysis of the SWI data showed high intensity variability among the subjects, notably related to their age and different head position in the scanner. Therefore, to standardize the image intensity appearing on these images, a histogram equalization algorithm proposed by Nyul et al. [14] was applied. It represents an one-to-one image transformation and therefore,

does not affect the image visual appearance. The histogram matching was done in a volume of interest (VOI) surrounding both thalami for each subject respectively. Figure 5.2 is representing an axial slice of the used VOI in one case. All four SWI images from the elderly population were used in the training step and the standard scale was build upon the deciles extracted from each image histogram. The results from this histogram matching are shown in figure 5.3.

To further enhance the edges and observable features on the SWI, the ITK gradient anisotropic diffusion filtering of conductance 0.3 was applied.

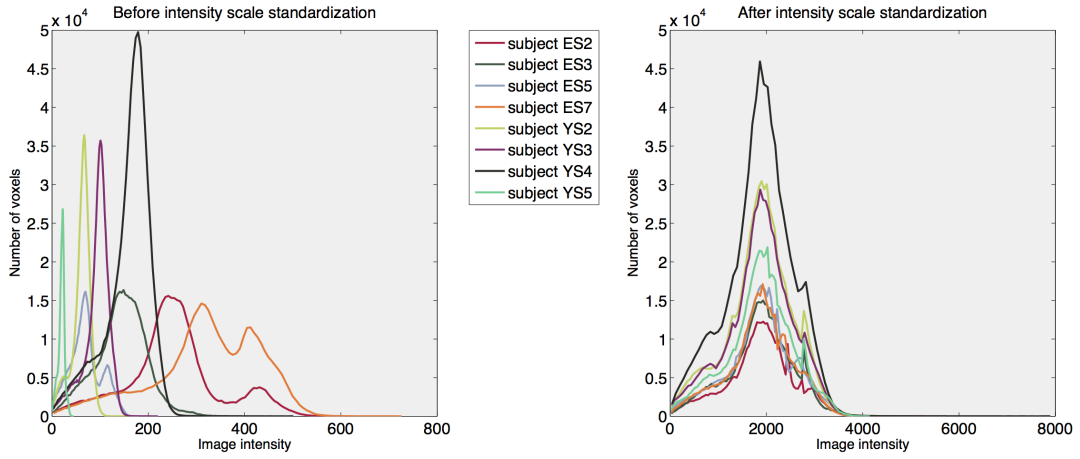


FIGURE 5.3 – Histogram equalization of the SWI intensity inside the thalamic area

Graph Representation and Parcellation

The preprocessed SWI-intensity information inside the VLV was transformed in a graph representation of the data. More precisely, a k-nn graph with 50 nearest neighbors was constructed with the edges' weights expressing the Gaussian weighting of the linear combination between the intensity distance (D_{int}) and the Euclidean distance (D_{pos}) among the i^{th} and the j^{th} VLV voxels :

$$D(i, j) = D_{int}(i, j) + \gamma D_{pos}(i, j) \tag{5.1}$$

where γ represents the ratio between $max(D_{int})$ and $max(D_{pos})$ and therefore, it acts as a scaling factor that brings the D_{pos} in the same range of values as D_{int} .

The parcellation of the graph was performed with Normalized Cut (NCut) partition [15] (for more details refer to section 3.4). We subdivided the VLV in 3 sub-clusters. The number 3 was chosen empirically since it gives a consistent parcellation pattern among the subjects. Moreover, the obtained clusters corresponded to the visually distinguishable VLV structure including a region with bright SWI intensity as the expected one in the Vim area, a region with

darker SWI intensity and an auxiliary part (see figure 5.5).

Geometry Quadrants

To isolate the inferior antero-lateral part of the VLV cluster obtained from diffusion MRI (section 5.2.3), *VLV_ial*, where the Vim is most likely to be found, VLV was divided using the geometry of the smallest rectangular cuboid that contains all of its non-zero voxels. More precisely, with the cuboid's mid-plane, the inferior part was separated from the superior one and with the in-plane diagonals the antero-lateral from the ventral-posterior part (see figure 5.4).

The separated *VLV_ial* portion was used to confine the NCut parcellation to the expected localization of the Vim (figure 5.5).

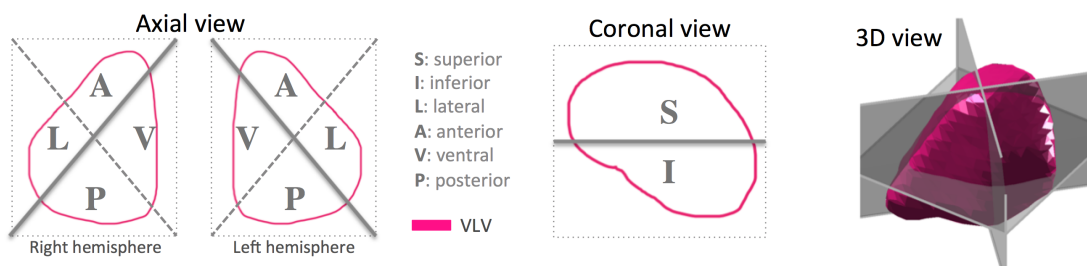


FIGURE 5.4 – Schematic illustration of the VLV-cluster separation in 8 geometrical quadrants

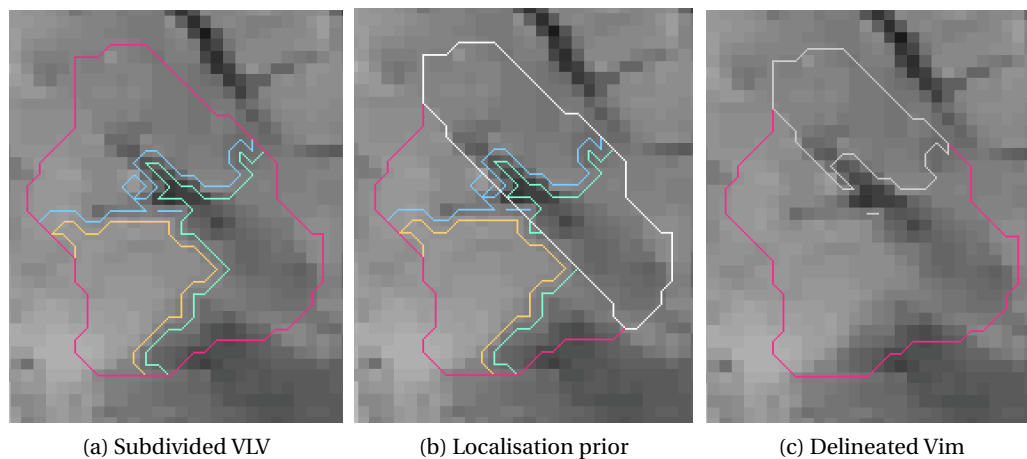


FIGURE 5.5 – Isolation of the inferior antero-lateral part of the left VLV cluster. In panel (a) the diffusion-based VLV outline is given with the magenta contour and additionally we can observe the three parcels obtained from SWI intensity-based NCut partition. The *VLV_ial* part for the given case is shown with the white contour in panel (b), while the final Vim outline, again in white, in panel (c)

5.2.5 Manual delineation of the Vim

Manual delineation of the Vim was done in all eight subjects by an experienced neurosurgeon (CT). As described in section 4.2.4, the delineation was mainly based upon the visible contrast variation together with the observation shown in [2] and the Schaltenbrand and Wahren atlas [12] and it was further used for evaluating the results of the proposed framework.

5.2.6 Multi-atlas segmentation

As the state-of-the-art lacks in automated Vim-delineation approaches, the aim of this chapter is to provide a direct segmentation of the Vim by using subject-specific information from both 3T DWI and 7T SWI. However, in case of available atlas, an alternative method would be applying atlas-based segmentation techniques.

In the previous chapter in section 4.2.4, I proposed a multi-atlas segmentation method enclosing two step for the matching between the images : first global correspondence achieved with affine transform between the corresponding T1w images and then local non-linear one between the respective SWI inside the thalamic area (the introduced VOI). The segmentation was done in leave-one-out scenario where the final multi-atlas outline was obtained by applying Joint Label Fusion method with corrective learning [16].

Having the Vim outlines for all eight subjects, the proposed atlas-based method was applied in this extended cohort in order to compare its outcome with the two other outlines, the manual and the multi-modal one introduced in this chapter.

5.2.7 Quantitative comparison

The obtained outlines were quantitatively compared with Dice coefficient of overlap [17]. Moreover, the true positive and true negative rate were also evaluated via the sensitivity and specificity respectively [18].

5.3 Results

The proposed multi-modal framework was tested for the group of 8 healthy subjects of different age scale or, more precisely, in 16 thalami in total. The intersection between the NCut parcellation and the VLV_ial portion mainly resulted in two subdivisions. Among the two, we choose as Vim outline the region showing brighter intensity (see figure 5.5).

The obtained findings are shown in figure 5.6 and figure 5.7, each of them representing one of the tested cohort. In some of the studied cases, a blood vessel was crossing the targeted area disintegrating its intensity homogeneity (see the right thalamus of ES1, ES2 and ES4 in figure 5.6, and the YS5's left thalamus in figure 5.7). However, an overlap with the manual

Chapitre 5. Multi-modal segmentation of the Vim

delineation was always observed. Moreover, for eight thalami the manual delineation was confined in the multi-modal outline.

In figure 5.6 and figure 5.7, notably for subjects ES3, ES4, YS2, YS4 and YS5, one can also notice that the automatically obtained outlines enclose minor parts of the surrounding structures or the internal capsule, which are mainly due to the irregular borders of the initial VLV region.

TABLE 5.1 – Volumes of the resulting Vim outlines

Volume [mm ³]	Multi-modal segmentation		Manual delineation		Multi-atlas segmentation	
	Left	Right	Left	Right	Left	Right
Subject ES1	122.5	149.2	93.0	94.5	42.7	23.7
Subject ES2	196.0	54.7	58.0	56.5	19.4	44.9
Subject ES3	198.4	187.2	81.5	65.5	32.4	9.7
Subject ES4	176.1	129.2	71.4	69.1	20.2	6.1
Subject YS2	156.9	160.2	76.3	82	66.9	71.6
Subject YS3	195.1	186.5	83.3	82.9	28.5	44.4
Subject YS4	189.8	113.5	82.8	73	42.4	42.4
Subject YS5	213.2	263.9	67.2	78.7	43.0	41.5

TABLE 5.2 – Overlap measures between the automated multi-modal segmentation and the manual delineation

Subject		ES1	ES2	ES3	ES4	YS2	YS3	YS4	YS5
Dice Coefficient	Left	56%	32%	51%	32%	51%	51%	30%	41%
	Right	35%	30%	32%	17%	41%	42%	42%	35%
Sensitivity	Left	64.52%	70.26%	88.19%	55.95%	77.81%	85.54%	49.03%	84.84%
	Right	44.84%	29.65%	60.88%	24.23%	60.27%	68.70%	53.17%	76.66%
Specificity	Left	99.93%	99.97%	99.99%	99.94%	99.97%	99.98%	99.93%	99.98%
	Right	99.89%	99.93%	99.96%	99.90%	99.95%	99.95%	99.95%	99.97%

TABLE 5.3 – Overlap measures the automated multi-atlas segmentation and the manual delineation

Subject		ES1	ES2	ES3	ES4	YS2	YS3	YS4	YS5
Dice Coefficient	Left	59%	32%	47%	31%	67%	35%	48%	42%
	Right	33%	63%	0%	13%	70%	63%	61%	57%
Sensitivity	Left	43.01%	21.55%	34.05%	20.25%	62.80%	23.46%	35.91%	34.21%
	Right	20.90%	56.42%	0%	7.05%	64.78%	48.68%	48.21%	43.79%
Specificity	Left	99.99%	99.99%	99.99%	99.99%	99.99%	99.99%	99.99%	99.99%
	Right	99.99%	99.99%	99.99%	99.99%	99.99%	99.99%	99.99%	99.99%

In terms of size, as reported in table 5.1, the multi-modal outline always delimitates bigger volume than the manual delineation. Since the expected size of the Vim is between 60 to 150 mm³ [19], the volumes of the proposed multi-modal delimitation are marginally exceeding the expected range. In contrast to this, the manual outlines are closer to the lower boundary of the anticipated size of the Vim.

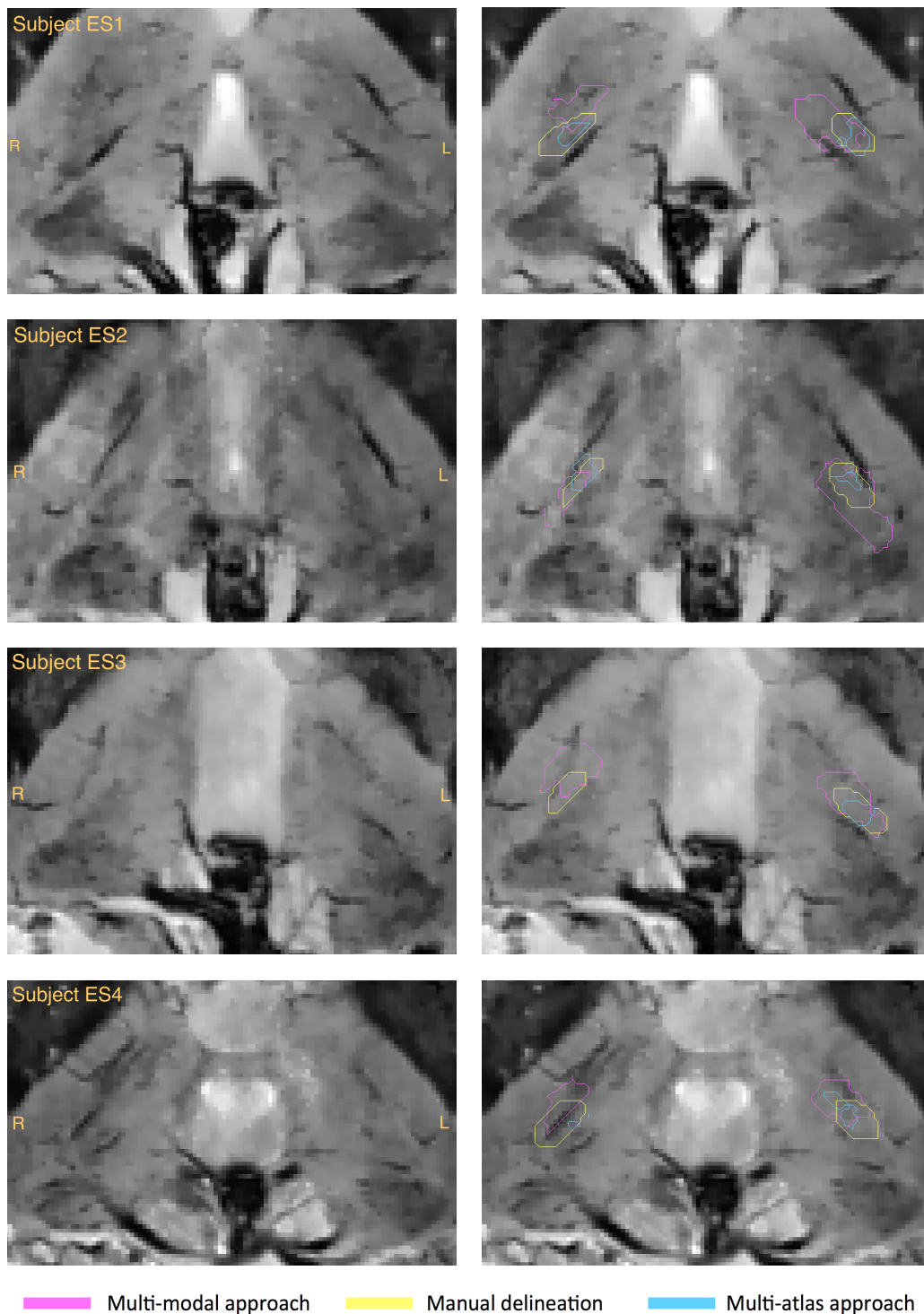


FIGURE 5.6 – Visual overview of the obtained findings for each elderly subject respectively. Left column gives a SWI-VOI slice, while the right the corresponding segmented contours.

The Dice coefficient measuring the overlap between the multi-modal and the manual outline was 38.6% in average with best score of 56%. For four out of 16 cases, the sensitivity was higher than 50% with maximum of 88.19%, while the specificity was always almost 100%. All overlap measures for each subject specifically are given in table 5.2.

The multi-atlas based approach provided, in general, slightly smaller in volume outlines than the manual delineation (see table 5.1). However, an overlap between them was again observed for each subject with exception of ES3 in the right hemisphere. Please refer to figures 5.6 and 5.7 for a visual overview of these results. The Dice coefficient showed better matching between the manual and the multi-atlas outline, than the multi-modal approach, with best score of 70%. Nevertheless, the sensitivity was higher than 50% for only three subjects while the specificity remain as high as for the multi-modal outline. Table 5.3 show these results for each subject respectively.

5.4 Discussion

Although performed on a limited number of subjects, the present study represents an important step towards an automated segmentation of the Vim area. We used local diffusion MR properties inside the thalamus for delimitation of an initial region of interest, the VLV cluster enclosing the motor-related thalamic nuclei, which was further subdivided using the 7T SWI intensity and a prior knowledge of the Vim localisation within the VLV.

In a lack of a *ground truth* for validation, the obtained multi-modal segmentation results were compared against the manual delineation of the Vim done based upon the 7T SWI visible features. The results show that, even though the resulting outlines are slightly overestimating the size of the Vim, they are however able to depict well the spatial localization of the targeted structure. The differences in size between the manual and the multi-modal delineation are leading to the obtained low to moderate Dice coefficients. Nonetheless, the calculated high true positive and true negative rate confirm a good matching between these two outlines.

As discussed in the previous chapter (section 4.4), due to the SWI inconsistency in contrast variation and random presence of blood vessels, the borders of the Vim are not always discernable and therefore, the manual delineation was done in an optic of including only the region that is undoubtedly corresponding to the Vim. Analogue to this, from the calculated volumes one can observe that the manual delineation tends to underestimate the Vim's extent. In consequence, the explored manual delineation does not represents the Vim in an absolute manner.

Since the multi-atlas approach was build upon the available manual delineation, it was expected that its outcome is close in volume to those manually depicted. However, in terms of overlap evaluation, the multi-atlas outcome showed lower sensitivity than the proposed multi-modal approach. Such finding demonstrates the potential of an imaging method based on individual subject's anatomy to outperform approaches build from statistical average among

a chosen population, such as the atlases. Nonetheless, the atlas-segmentation techniques remain the most pertinent alternative.

The multi-modal approach presents however several limitations. For instance, an affinity towards marginally inaccurate borders regarding the surrounding structures was observed in the resulting outline. This is mainly due to the DWI used for the VLV delineation which has approximately five times lower spatial resolution than the image reference space where the analysis were performed ($\sim 2x2x2mm^3$ versus $\sim 0.5x0.5x0.5mm^3$). Subsequently, the proposed method is prone to imprecise delineation of the initial region of interest i.e. the VLV thalamic part.

Another limitation, as well for the manual delineation, comes from the non-robust contrast variation observed on the SWI together with the presence of the blood vessels in an indiscriminate mode, inside the VLV and the thalamus in general, increasing the potential of delineated Vim's border inaccuracy. Moreover, the difference in contrast variation is even more enhanced between the dataset acquired from volunteers of different age scales, i.e. young and elderly population [20, 21]. More precisely, the Vim is not always as clearly distinguishable in the SWI from elderly subjects in comparison with the young population. Such drawback is of particular importance since the tremor patients are mainly part of the elderly population.

Recent developments in our group addressed current limitation of 7T SWI and achieved an improvement with incorporation of both contrast enhancement resulting from modified phase-magnitude combination and suppression of venous vessels [22]. Figure 5.8 give an example of the outcome. One can observe that the observable regions are more pronounced and therefore, more distinguishable, which leads to clearer discrimination of the Vim borders. Such findings are beneficial for both direct visualization and automated segmentation of the target, making this imaging method even more powerful tool for the direct targeting in functional neurosurgery applied for treatment of drug-resistant tremor.

Further studies on a bigger datasets should be done to explore more profoundly newly developed SWI advancements. Additionally, merging such information simultaneously with improved spatial-resolution DWI could potentially lead to even more precise Vim outline.

5.5 Conclusion

This chapter presents an automated approach for outlining the Vim area while exploring the 7T SWI intensity-based features inside the motor-related thalamic cluster obtained from previously introduced segmentation framework based on local diffusion properties. Although limited in exact border segmentation, the proposed method is able to discriminate the spatial localisation of the targeted area and therefore, represents a novel advancement in the field of automated subject-specific segmentation of the Vim.

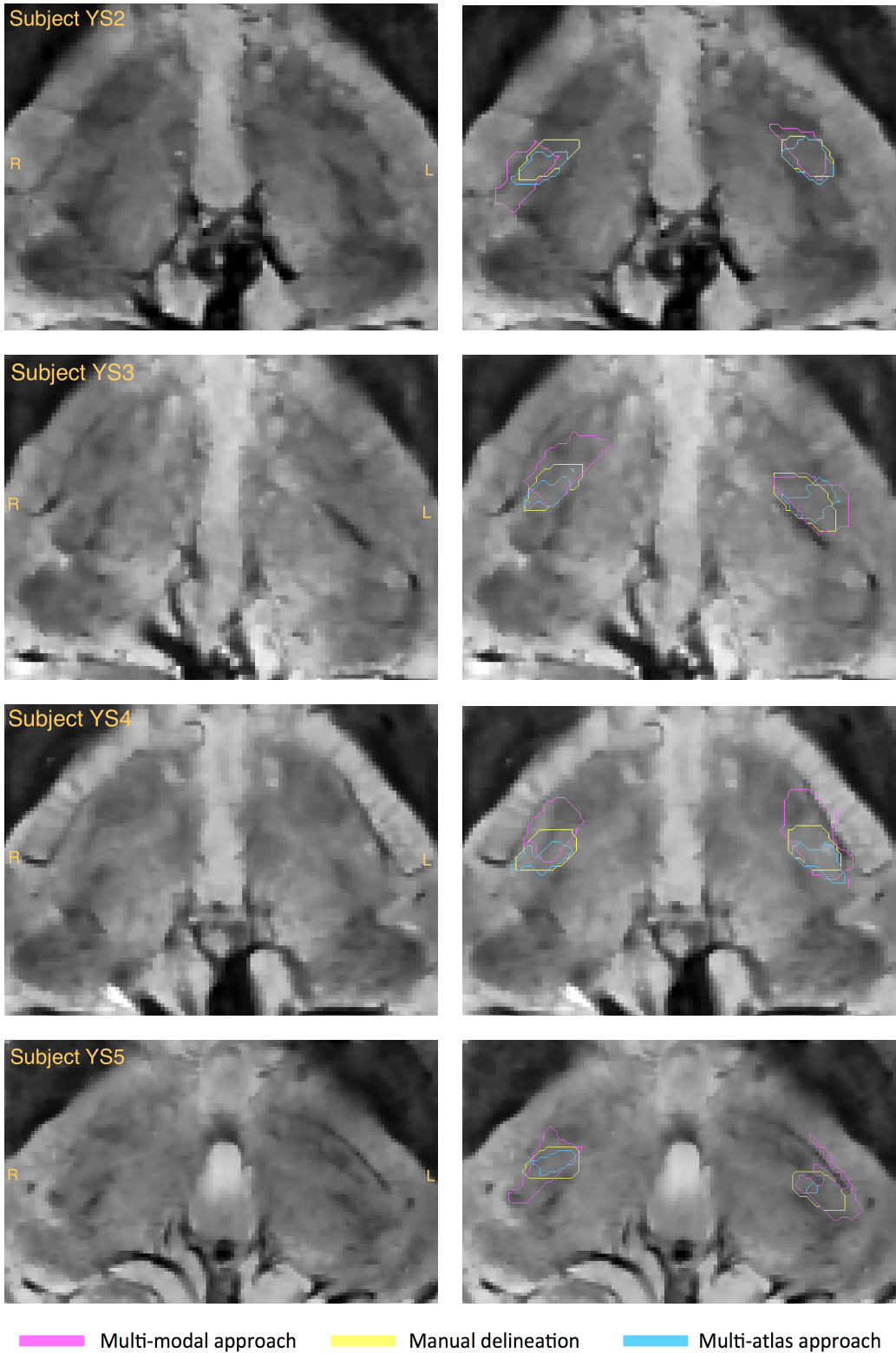


FIGURE 5.7 – Visual overview of the obtained findings for each young subject respectively. Left column gives a SWI-VOI slice, while the right the corresponding segmented contours.

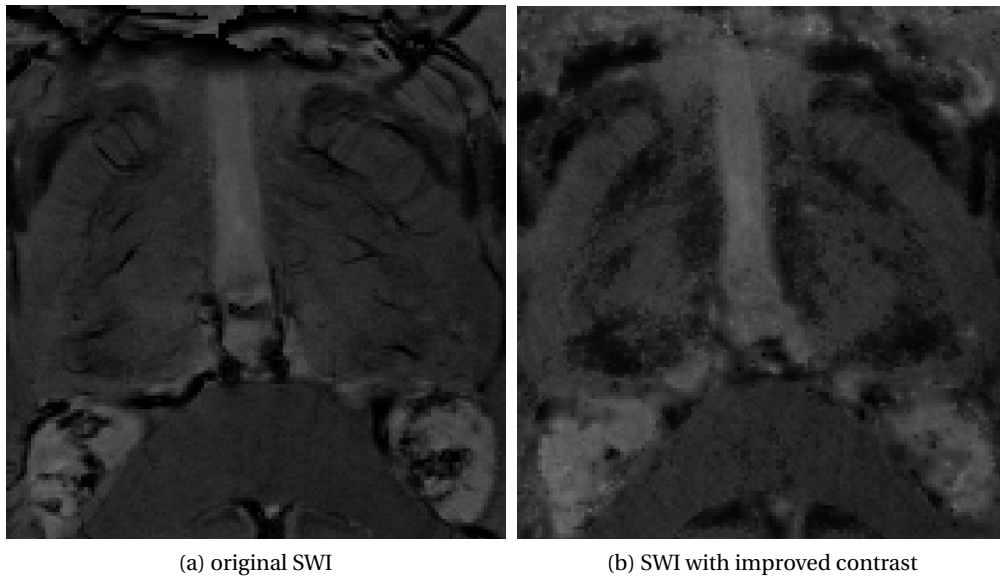


FIGURE 5.8 – Illustration of the improved SWI contrast developed in our group. Acknowledging Dr. João Jorge.

Bibliographie

- [1] G. Battistella, E. Najdenovska, P. Maeder, N. Ghazaleh, A. Daducci, J.-P. Thiran, S. Jacquemont, C. Tuleasca, M. Levivier, M. Bach Cuadra, E. Fornari, Robust thalamic nuclei segmentation method based on local diffusion magnetic resonance properties, *Brain Structure & Function* 222 (5) (2017) 2203–2216.
- [2] A. Abosch, E. Yacoub, K. Ugurbil, N. Harel, An Assessment of Current Brain Targets for Deep Brain Stimulation Surgery With Susceptibility-Weighted Imaging at 7 Tesla, *Neurosurgery* 67 (6) (2010) 1745–1756.
- [3] V. Fonov, A. Evans, R. Mckinstry, C. Almli, L. Collins, Unbiased nonlinear average age-appropriate brain templates from birth to adulthood, *Neuroimage* 47.
- [4] A. Fedorov, R. Beichel, J. Kalpathy-Cramer, J. Finet, J.-C. Fillion-Robin, S. Pujol, C. Bauer, D. Jennings, F. Fennessy, M. Sonka, J. Buatti, S. Aylward, J. V. Miller, S. Pieper, R. Kikinis, 3d Slicer as an image computing platform for the Quantitative Imaging Network, *Magnetic Resonance Imaging* 30 (9) (2012) 1323–1341.
- [5] J.-D. Tournier, F. Calamante, A. Connelly, Mrtrix : Diffusion tractography in crossing fiber regions, *International Journal of Imaging Systems and Technology* 22 (1) (2012) 53–66.
- [6] J. Veraart, E. Fieremans, D. S. Novikov, Diffusion mri noise mapping using random matrix theory, *Magnetic Resonance in Medicine* 76 (5) (2016) 1582–1593.
- [7] J. Veraart, D. S. Novikov, D. Christiaens, B. Ades-Aron, J. Sijbers, E. Fieremans, Denoising of diffusion MRI using random matrix theory, *NeuroImage* 142 (2016) 394–406.
- [8] S. M. Smith, M. Jenkinson, M. W. Woolrich, C. F. Beckmann, T. E. J. Behrens, H. Johansen-Berg, P. R. Bannister, M. De Luca, I. Drobnjak, D. E. Flitney, R. K. Niazy, J. Saunders, J. Vickers, Y. Zhang, N. De Stefano, J. M. Brady, P. M. Matthews, Advances in functional and structural MR image analysis and implementation as FSL, *NeuroImage* 23 Suppl 1 (2004) S208–219.
- [9] Y. Zhang, M. Brady, S. Smith, Segmentation of brain MR images through a hidden Markov random field model and the expectation-maximization algorithm, *IEEE transactions on medical imaging* 20 (1) (2001) 45–57.
- [10] A. Leemans, D. K. Jones, The B-matrix must be rotated when correcting for subject motion in DTI data, *Magnetic Resonance in Medicine* 61 (6) (2009) 1336–1349.
- [11] J. L. R. Andersson, S. N. Sotiropoulos, An integrated approach to correction for off-resonance effects and subject movement in diffusion MR imaging, *NeuroImage* 125 (2016) 1063–1078.

Bibliography

- [12] G. Schaltenbrand, W. Wahren, Atlas for Stereotaxy of the Human Brain, Thieme, 1977.
- [13] N. J. Tustison, B. B. Avants, P. A. Cook, Y. Zheng, A. Egan, P. A. Yushkevich, J. C. Gee, N4itk : improved N3 bias correction, *IEEE transactions on medical imaging* 29 (6) (2010) 1310–1320.
- [14] L. G. Nyúl, J. K. Udupa, X. Zhang, New variants of a method of MRI scale standardization, *IEEE transactions on medical imaging* 19 (2) (2000) 143–150.
- [15] J. Shi, J. Malik, Normalized cuts and image segmentation, in : *Proceedings of IEEE Computer Society Conference on Computer Vision and Pattern Recognition*, 1997, pp. 731–737.
- [16] H. Wang, P. A. Yushkevich, Multi-atlas segmentation with joint label fusion and corrective learning - an open source implementation, *Frontiers in Neuroinformatics* 7.
- [17] L. R. Dice, Measures of the Amount of Ecologic Association Between Species, *Ecology* 26 (3) (1945) 297–302.
- [18] K. J. van Stralen, V. S. Stel, J. B. Reitsma, F. W. Dekker, C. Zoccali, K. J. Jager, Diagnostic methods I : sensitivity, specificity, and other measures of accuracy, *Kidney International* 75 (12).
- [19] P. Tuite, A. Dagher (Eds.), *Magnetic Resonance Imaging in Movement Disorders : A Guide for Clinicians and Scientists*, 1st Edition, Cambridge University Press, Cambridge, 2013.
- [20] S. L. Harder, K. M. Hopp, H. Ward, H. Neglio, J. Gitlin, D. Kido, Mineralization of the Deep Gray Matter with Age : A Retrospective Review with Susceptibility-Weighted MR Imaging, *American Journal of Neuroradiology* 29 (1).
- [21] A. Pfefferbaum, E. Adalsteinsson, T. Rohlfing, E. V. Sullivan, MRI estimates of brain iron concentration in normal aging : Comparison of field-dependent (FDRI) and phase (SWI) methods, *NeuroImage* 47 (2) (2009) 493–500.
- [22] J. Jorge, E. Najdenovska, C. Tuleasca, J. P. Marques, M. Levivier, P. Maeder, R. Gruetter, M. B. Cuadra, Improved susceptibility-weighted imaging of the thalamic nuclei at 7t with enhanced contrast and venous vessel exclusion, in : *submitted for the Joint Annual Meeting ISMRM-ESMRMB*, 2018.

6

Conclusion and Perspectives

The first main contribution of this thesis was a **novel MRI-based approach for automated segmentation of the thalamic subparts** [1, 2]. In a modified k-means clustering framework, it explores local diffusion properties from DWI acquired at 3 T that are represented by the orientation distribution function (ODF) projected in spherical harmonics basis. The ODF ability to fully characterise the diffusion process in each voxel surpass the performance of the state-of-art features used for the thalamic parcellation. Therefore, in combination with a data-driven initialisation based on the spatial position, it provides a robust and a highly reproducible segmentation of **seven groups of thalamic nuclei** where each one of them presents a characteristic spatial distribution that is **closely matching the thalamic anatomy** presented in Morel's atlas [3].

Additional contribution of this thesis is the extensive evaluation on data acquired from both healthy volunteers and patients. The developed segmentation framework was primarily tested on a cohort of 35 healthy subject for which the diffusion data was acquired with traditional spatial resolution of $\sim 2x2x2mm^3$ [1, 2]. The evaluation was further extended for a relatively bigger healthy population enclosing 73 subject from the **Human Connectome Project (HCP) database** [4, 5] for which the available diffusion data was with improved voxel-size of $1.25mm$ isotropically. With a segmentation success rate of 92%, the obtained outcome from 67 HCP subjects classified as good parcellation was further used to build a **spatial probabilistic atlas maps (SPAM)** for **each cluster** in MNI space [6]. This population atlas could be used as a tool for subsegmenting the thalamus in subjects for which the diffusion data is not available.

Another extension of the segmentation-framework evaluation was done on a dataset acquired from 65 drug-resistant **tremor patients** treated with Gamma Knife surgery (GKS, 63 of them)

Chapitre 6. Conclusion and Perspectives

and Deep Brain Stimulation (DBS, 2) at Marseille University Hospital (CHU Timone, France) and Lausanne University Hospital (CHUV). This analysis showed that **the proposed thalamic parcellation approach remains robust** even in cases where the tested subject is prone to engender stronger motion artefacts [2, 7, 8].

One of the segmented cluster is the **ventral latero-ventral (VLV) group** that includes the motor-related thalamic nuclei. Among them is the ventro-intermediate nucleus (Vim) that is the most commonly used target for treatment of tremor in functional neurosurgery. The follow-up data available from 18 tremor patients treated with GKS allowed a **clinical validation** of the VLV spatial distribution since the target-related contrast enhancement appearing on those images was **always included in this cluster** [2, 7, 8].

The additional **subdivision of the VLV** cluster, based again on the ODF information, but this time in initialisation-independent graph-partition framework, led to a **narrower localization of the targeted Vim area** in 70% of the tested cases [7, 8]. This findings were further confirmed with the final electrode position in two tremor patients treated with DBS [8].

Another major contribution of this thesis refers the image analysis developed for exploring the advantages provided from a recent implementation done at 7T MRI. In a pilot study enclosing five healthy young subjects, aside from 3T DWI, susceptibility-weighted images (SWI) at 7 T were also acquired. Accordingly to the enhanced intensity contrast-variation provided by SWI inside the thalamic region, a manual delineation of the **visually distinguishable Vim** was realized. The comparison with the points of the Guiot's quadrilateral, used in both CHU Timone and CHUV for GKS treatment of tremor, showed **confined localisation of the targeting position** inside the manual outline [9, 10].

The improved in-vivo visualisation of several thalamic nuclei provided by 7T SWI validated further the spatial localisation of all the seven segmented group of nuclei. Moreover, the **directly detectable Vim** was always found in a **restricted area inside the automatically delineated VLV cluster**. However, the comparison between the diffusion-based VLV subdivision and the manual Vim outline showed that the anticipated subcluster is not including the entire Vim, but only the Guiot targeting points and the area corresponding to the 90 Gy isodose [9].

The distinguishable thalamic regions on **7T SWI** were further used for **improving** the thalamic matching between the images for **atlas-based segmentation** purposes. Consequently, the proposed multi-atlas segmentation framework built in a multi-modal manner could be considered as an alternative for an automated delineation or as initialisation of a subject-related segmentation of the targeted nucleus [9].

Finally, with combing both the spatial localisation of the Vim inside the VLV cluster and the 7T SWI intensity-based feature, I proposed a **method for an automated discrimination of the Vim spatial localisation** [11]. It was developed and evaluated for a dataset including four healthy young and additional four healthy elderly subject matching the age of the tremor patients. The introduced method, based only on the individual anatomy, showed **better**

segmentation sensitivity than the previously proposed **multi-atlas segmentation**.

In summary the contributions of these thesis can be categorized as :

1. Methodological developments

- Automated, robust and reproducible framework for segmenting seven thalamic subparts : anterior, ventral anterior, medio-dorsal, ventral latero-ventral, ventral latero-dorsal, pulvinar and a cluster enclosing the central lateral, the lateral posterior and portion of medial pulvinar.
- Delineation of a narrower region corresponding to the targeted Vim area via a subdivision of the automatically segmented motor thalamic part
- Multi-atlas segmentation approach based on matching thalamic features
- Automated subject-based delineation of the region representing the Vim

2. Outcome evaluation

- The proposed thalamic parcellation approach was tested in a large cohort including 123 healthy volunteers and 65 drug-resistant tremor patients. The explored DWI are from different acquisition schemes, including different scanners.
- The delineated group of motor nuclei was validated in 18 tremor patients treated with GKS having follow-up data that show target-related contrast-enhancement

3. Built tools

- Spatial probabilistic atlas maps for each segmented thalamic subpart in MNI space

4. Available data

- 5 healthy young subjects : T1w (MPRAGE), T2w, T2w CISS and dMRI acquired at 3T and T1w (MP2RAGE) and SWI acquired at 7T
- 4 healthy elderly subjects : T1w (MPRAGE), T2w, T2w CISS, dMRI and functional MRI acquired at 3T and T1w (MP2RAGE) and SWI acquired at 7T (ongoing acquisitions)
- Manual delineation of the Vim for all 9 subjects

Perspectives

The main limitation of the work presented in this thesis is related to the relatively coarse spatial resolution of the explored DWI, which is however representing the current standard diffusion MRI. Such drawback is due to the limited scan time while maintaining a good signal to noise ratio [12]. In relation to the presented findings, an improved spatial resolution could lead to more accurate borders discrimination of the segmented thalamic groups of nuclei as

well as more precise delineation while propagating them in other image space with superior resolution, such as the 7T SWI. Additionally, DWI data with finer voxels could potentially allow a robust segmentation of more than seven thalamic subparts. In the same context, the VLV subdivision could also be extended in number of clusters and therefore will possible provide more accurate localisation of the targeted area. All of these hypothesis could be tested in the currently available DWI data with better resolution, as the HCP data for instance. However, for overcoming the limitation in the standard datasets, one alternative would be to take advantage of the interpolation method proposed by Dyrby et al. [12] for upsampling the voxel-size up to its double that furthermore provides outcome able to capture anatomical features observable only with higher resolution.

In terms of diffusion MRI information, new advanced modellings such as the neurite orientation dispersion and density imaging (NODDI) [13], the spherical mean technique [14] and the mean apparent propagator (MAP MRI) [15] are tending to represent the diffusion process at a microstructural level and as such could be further explored for gaining new insights of the underlying characteristics discriminating the thalamic nuclei.

Other limitations come from the unstandardised contrast variation of the 7T SWI among different subjects, especially noticeable between young and elderly population [16, 17]. In addition, random appearance of blood vessels inside the thalamic region could also alter the provided information. As discussed in section 5.4, recent developments in our group succeeded at optimizing the SWI contrast (see figure 5.8) and, in consequence, provided clearer discrimination between the directly visible thalamic nuclei. Hence, the value of SWI has grown in terms of source for accurate and reliable features for delineation of not only the Vim but the other parts of the thalamus as well. Such advantage could possibly extend the accuracy performance of the already proposed methods for parcellating the thalamus based on manually labelled features [18, 19] which is mainly beneficial for data lacking in SWI. Or, when the individual SWI is available, it could be further employed in automated segmentation approaches such as the coupled level set functions as already used for exploring the diffusion information [20].

The DWI is representing the histology of the tissue in terms of the water molecules' displacement, while SWI give insights of the anatomical structures based on their sensitivity to magnetic susceptibility effects. Hence, as both imaging techniques are complementary between each other, a framework embodying simultaneously the two modalities has strong potential of providing a finer and more accurate delineation of the thalamic nuclei. This could be potentially achieved by employing the joint variational segmentation method proposed by Wojak et al. [21] that was build for segmenting tumour lesions for radiotherapy purposes. This approach is regularized with a Total Variation norm and allows simultaneous use of images with different spatial resolution (Computer Tomography and Positron Emission Tomography scans) while assuring a robust behaviour to eventual mis-registration between the images.

Bibliographie

- [1] G. Battistella, E. Najdenovska, P. Maeder, N. Ghazaleh, A. Daducci, J.-P. Thiran, S. Jacquemont, C. Tuleasca, M. Levivier, M. Bach Cuadra, E. Fornari, Robust thalamic nuclei segmentation method based on local diffusion magnetic resonance properties, *Brain Structure & Function* 222 (5) (2017) 2203–2216.
- [2] E. Najdenovska, G. Battistella, C. Tuleasca, P. Maeder, A. Daducci, J.-P. Thiran, M. Levivier, M. Bach Cuadra, Novel Robust Segmentation of the Thalamic Nuclei - Validation on Healthy Subjects and Patients, in : *Joint Annual Meeting ISMRM-ESMRMB*, 2015.
- [3] A. Morel, M. Magnin, D. Jeanmonod, Multiarchitectonic and stereotactic atlas of the human thalamus, *J. Comp. Neurol.* 387 (4) (1997) 588–630.
- [4] S. N. Sotiropoulos, S. Jbabdi, J. Xu, J. L. Andersson, S. Moeller, E. J. Auerbach, M. F. Glasser, M. Hernandez, G. Sapiro, M. Jenkinson, D. A. Feinberg, E. Yacoub, C. Lenglet, D. C. Van Essen, K. Ugurbil, T. E. J. Behrens, WU-Minn HCP Consortium, Advances in diffusion MRI acquisition and processing in the Human Connectome Project, *NeuroImage* 80 (2013) 125–143.
- [5] D. C. Van Essen, S. M. Smith, D. M. Barch, T. E. J. Behrens, E. Yacoub, K. Ugurbil, WU-Minn HCP Consortium, The WU-Minn Human Connectome Project : an overview, *NeuroImage* 80 (2013) 62–79.
- [6] E. Najdenovska, Y. Alemán-Gomez, G. Battistella, A. Griffa, M. Descoteaux, P. Hagmann, S. Jacquemont, P. Maeder, J.-P. Thiran, E. Fornari, M. Bach Cuadra, A probabilistic atlas of the human thalamic nuclei based on diffusion Magnetic Resonance Image segmentation, *Scientific Data in Nature*, under preparation.
- [7] E. Najdenovska, C. Tuleasca, X. Bresson, P. Maeder, G. Battistella, E. Fornari, J. Regis, J.-P. Thiran, M. Levivier, M. Bach Cuadra, Localization of the Ventro-Intermediate Thalamic Nucleus Using Local Diffusion Properties, in : *Annual Meeting of the Organization for Human Brain Mapping (OHBM)*, 2016.
- [8] E. Najdenovska, C. Tuleasca, J. Bloch, P. Maeder, N. Girard, T. Witjas, J. Regis, J.-P. Thiran, M. B. Cuadra, M. Levivier, Exploring Local Diffusion MRI Properties for Vim Localization : Evaluation in Clinical Cases, in : *International Stereotactic Radiosurgery Society (ISRS) congress*, 2017.
- [9] E. Najdenovska, C. Tuleasca, J. Jorge, P. Maeder, J. P. Marques, T. Roine, D. Gallichan, J.-P. Thiran, M. Levivier, M. Bach Cuadra, Advanced Imaging of the Ventral Intermediate Thalamic Nucleus : A Proof of Concept, *Journal of Neurosurgery*, under review.

Bibliography

- [10] E. Najdenovska, C. Tuleasca, J. P. Marques, J. Jorge, D. Gallichan, P. Maeder, J.-P. Thiran, M. Levivier, M. Bach Cuadra, Vim's Anatomical Landmarks : Indirect Targeting vs. Direct Visualization at 7T MRI, in : International Stereotactic Radiosurgery Society (ISRS) congress.
- [11] E. Najdenovska, C. Tuleasca, J. Jorge, J. P. Marques, P. Maeder, J.-P. Thiran, M. Levivier, M. B. Cuadra, Towards an Automated Segmentation of the Vento-Intermediate Thalamic Nucleus, in : Computer Assisted and Robotic Endoscopy and Clinical Image-Based Procedures, Lecture Notes in Computer Science, Springer, Cham, 2017, pp. 141–150.
- [12] T. B. Dyrby, H. Lundell, M. W. Burke, N. L. Reislev, O. B. Paulson, M. Ptito, H. R. Siebner, Interpolation of diffusion weighted imaging datasets, *NeuroImage* 103 (Supplement C).
- [13] H. Zhang, T. Schneider, C. A. Wheeler-Kingshott, D. C. Alexander, NODDI : practical in vivo neurite orientation dispersion and density imaging of the human brain, *NeuroImage* 61 (4) (2012) 1000–1016.
- [14] E. Kaden, F. Kruggel, D. C. Alexander, Quantitative mapping of the per-axon diffusion coefficients in brain white matter, *Magnetic Resonance in Medicine* 75 (4) (2016) 1752–1763.
- [15] E. Ozarslan, C. G. Koay, T. M. Shepherd, M. E. Komlosh, M. O. Irfanoglu, C. Pierpaoli, P. J. Basser, Mean apparent propagator (MAP) MRI : a novel diffusion imaging method for mapping tissue microstructure, *NeuroImage* 78 (2013) 16–32.
- [16] S. L. Harder, K. M. Hopp, H. Ward, H. Neglio, J. Gitlin, D. Kido, Mineralization of the Deep Gray Matter with Age : A Retrospective Review with Susceptibility-Weighted MR Imaging, *American Journal of Neuroradiology* 29 (1).
- [17] A. Pfefferbaum, E. Adalsteinsson, T. Rohlfing, E. V. Sullivan, MRI estimates of brain iron concentration in normal aging : Comparison of field-dependent (FDRI) and phase (SWI) methods, *NeuroImage* 47 (2) (2009) 493–500.
- [18] Y. Liu, P.-F. D'Haese, A. T. Newton, B. M. Dawant, Thalamic nuclei segmentation in clinical 3t T1-weighted Images using high-resolution 7t shape models, Vol. 9415, International Society for Optics and Photonics, 2015, p. 94150E.
- [19] J. Su, T. Turdias, M. Saranathan, P. Ghanouni, B. Rutt, THOMAS : Thalamus Optimized Multi-Atlas Segmentation at 3T, in : Joint Annual Meeting ISMRM-ESMRMB, 2016, 2016.
- [20] L. Jonasson, P. Hagmann, C. Pollo, X. Bresson, C. Richero Wilson, R. Meuli, J.-P. Thiran, A level set method for segmentation of the thalamus and its nuclei in DT-MRI, *Signal Processing* 87 (2) (2007) 309–321.
- [21] J. Wojak, E. D. Angelini, I. Bloch, Joint variational segmentation of CT-PET data for tumoral lesions, in : 2010 IEEE International Symposium on Biomedical Imaging : From Nano to Macro, 2010, pp. 217–220.



Appendixes

A.1 Assessment of Frameless versus Frame-based Registration of Computed Tomography and Magnetic Resonance Imaging in Gamma Knife Surgery Planning

The work in this section was presented as first author oral communication at the 17th International Meeting of Leksell Gamma Knife Society in 2014. The list of co-authors includes : E. Najdenovska, C. Tuleasca, F. Vingerhoets, J.-P. Thiran, M. Levivier and M. Bach Cuadra.

Introduction

Gamma Knife surgery (GKS) is a neurosurgical, minimally invasive, stereotactic procedure, combining image guidance with high-precision convergence of multiple gamma rays emitted by 192 sources of Cobalt-60 (Leksell Gamma Knife Perfexion[®], Elekta Instruments, AB, Sweden) [1]. It is currently used in many neurosurgical conditions, as an alternative to open microsurgery. As an image-guided therapeutic approach, exploring multimodal information from both Computer Tomography (CT) and magnetic resonance (MR) sequences is of crucial importance for optimal treatment planning.

The imaging protocols used for treatment planning may vary among hospital centres and depend on the pathological condition. As an example, in the case of brain metastases, both native and injected T1-weighted contrast (T1w) are used [2, 3] ; for trigeminal neuralgia, T2 constructive interference in steady state (T2 CISS) / Fast Imaging Employing Steady-state Acquisition (Fiesta, Siemens) is additionally used to have a good visualization of the trigeminal nerve

Annexe A. Appendixes

and surrounding cistern [4] ; in vestibular schwannomas, the use T2 CISS/Fiesta (Siemens) native (if the tumor is of small size) and/or injected if the tumor is of bigger size, entering in contact with the brainstem is recommended [5] ; additionally, for the ventro-intermediate (Vim) thalamotomy, the information provided by diffusion weighted imaging (DWI) is essential for ensuring a steep gradient towards the internal capsule [6]. Furthermore, CT is used to check for, and correct if necessary, any distortions that might appear on the MRI [7–10].

To adequately exploit the multi-modal information, a precise voxel-to-voxel correspondence must be ensured between the different therapeutic images prior to starting the treatment planning. Hence, accurate and robust image-registration techniques are needed.

Currently, within Leksell GammaPlan[®] (LGP, Elekta Instruments, AB, Sweden) planning software, the “gold standard” for achieving the image matching is the Indicator Box (a piece of the fiducial-based system attached to the stereotactic frame, figure A.1), which is a compulsory element during the acquisition of the planning images. The stereotactic frame itself is considered of major importance for several reasons : firstly, it provides the reference system for the so-called “stereotactic coordinates” allowing a high precision, while making the correspondence between the patient and device coordinate system ; secondly, it is an immobilizing device that has a high accuracy, ensuring successful targeting of small to medium-size intracranial conditions ; thirdly, due to its design, LGP can determine the error of this registration.

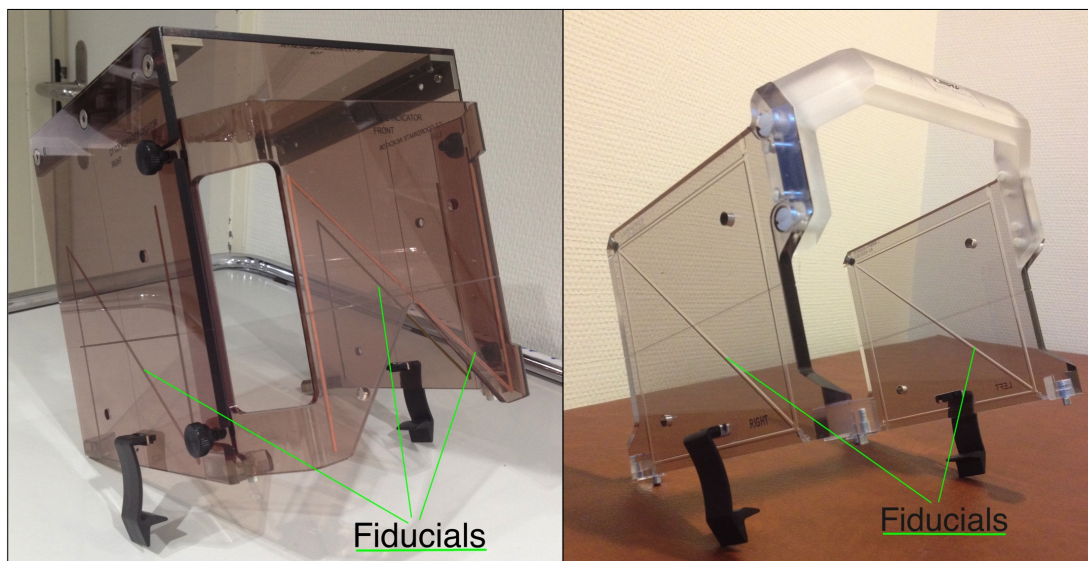


FIGURE A.1 – The Indicator Boxes used for acquiring the therapeutic images (Leksell Gamma Knife Perfexion[®], Elekta Instruments, AB, Sweden) : CT (left) MRI (right).

In other surgical and most radiosurgical therapeutic approaches, MR images are indeed acquired in a frameless mode. This is often the case in Linear Accelerator (LINAC)-based radiosurgery where matching between the different planning images is achieved by a voxel-based image transform. A similar approach could be used in LGP, where non-stereotactic MR can be co-registered with stereotactic CT and/or MR. However, in the absence of the fiducials,

A.1. Assessment of Frameless versus Frame-based Registration of Computed Tomography and Magnetic Resonance Imaging in Gamma Knife Surgery Planning

LGP currently can not display the respective registration error. Furthermore, beyond treatment planning precision, the error estimation in the absence of fiducials would be of high practical value in measuring the accuracy of pre-operative and follow-up MR images.

Few studies attempted to estimate the quality of the voxel-based registration for GKS purposes, either by working with image phantoms [11–13] or by comparing the target contours on real clinical cases [13]. All of them used the LGP software for matching the images.

Watanabe et al. used a TOWER phantom [11, 14] and estimated a mean error of the CT-T1w merging as the difference between the coordinate positions of the 9 phantom landmarks (tips of thin cylindrical acrylic rods). The calculated registration error was, on average, 1.18 ± 0.36 mm. However, the analysed images had highly different slice thickness (1mm for the T1w and 2 or even 3 mm for the CT), while their spatial resolution was quite comparable (0.43 mm^2 vs. 0.53 mm^2 for T1w and CT respectively). Other two studies worked on phantom images with more similar voxel-size as they are currently used in everyday clinical practice. Sajeev et al. [12] explored a Perspex phantom with 5 volume chambers serving as landmarks for the error estimation. The reported error values for the CT-T1 fusion were 0.38 mm, 0.62 mm and 0.93 mm along x, y and z axis respectively. Recently, similar results for images acquired from phantoms were reported by [13]. Among other analyses, they have evaluated the error between the stereotactic CT and the MRI co-registered with it. A grid-patterned phantom and an acrylic plate with 9 small cylinder-shaped baths were employed. The measured error along each direction (x, y and z) was less than 1 mm.

Additionally to the landmark-based error calculated for phantom images, Nakazawa et al. [13] have also estimated the voxel-based registration quality for real clinical cases, by geometrically comparing the targets delineated on the stereotactic MR with frame and the diagnostic frameless MR, co-registered to the stereotactic CT. The explored MR modality was the 3-dimensional spoiled gradient recalled acquisition in the steady state (3D-SPGR) of patients with big vestibular schwannomas lesions injected with Gadolinium. The error was expressed either by the volume difference between the outlined targets (0.05 ml in average) or by the root mean square (RMS) error between the centre-of-gravity coordinates (1.06 ± 0.60 mm). It is the only study that investigates real clinical images. Still, along with the fact that their dataset enclosed only 11 cases, the error estimation relies on the target delineation that is a subjected-dependent task and therefore, not a highly reliable reference.

The purpose of our work is to assess the accuracy of the voxel-based registration between the CT and MR images with an aim of overcoming the limitations of the previous studies. Our main contribution is to quantitatively estimate the voxel-based registration error for real clinical cases (not phantoms) while considering the most reliable reference for the GKS users - the stereotactic frame (see figure A.1). Additionally, we perform the analysis on a big data set from 30 patients containing three different MR contrasts. Moreover, we also aim to find a value expressing the difference between the outcomes provided by the voxel-based and the landmark-based transform seen as the gold standard for GKS treatment planning.

Materials and Methods

Dataset

Our study involved CT and MR therapeutic stereotactic images from 30 patients, treated with GKS at the Lausanne Univeristy Hospital during the period from July 2010 to June 2014. The dataset is composed of two mains groups :

1. Twenty patients (mean age : 62.6 ± 15.4 years) without parenchyma deformation. The treated conditions were idiopathic trigeminal neuralgia (14 patients) and small vestibular schwannomas (corresponding to Koos grades I and II [15], 6 patients). For all those patients we had several therapeutic image acquisitions : individual native (non-injected) and injected T1w images and the CT scan. Moreover, for 10 among the 14 trigeminal neuralgia patients the corresponding T2 CISS were also included in the dataset.
2. Ten patients (mean age 64.6 ± 8.7 years) treated for brain metastasis, therefore with significant deformation of the brain parenchyma. This dataset involved their native T1w MR and the CT scan.

All CT images were acquired with LightSpeed V CT, GE Medical Systems considering the following protocol : 2 rad exposure, 200 mA X-Ray-Tube-Current, 120 kV KVP, voxel-size : $0.5 \times 0.5 \times 0.625$ mm³, in-plane dimension : 512x512, number of slices varying between 241 and 295. The T1w images for the 6 patients treated form small vestibular schwannomas were obtained from a 1.5T Symphony SIEMENS Scanner, having TR/ TE = 2160/ 4.88 ms, voxel-size : $1 \times 1 \times 1.5$ mm³, dimension : 256x256x144, while the remaining 24 (form the first and the second data set) with a 1.5T SIEMENS Aera Scanner using TR/ TE = 1910/ 3.01 ms, voxel-size : $1 \times 1 \times 1$ mm³, dimension : 256x256x176. The T2 CISS images were also obtained with 1.5T SIEMENS Aera Scanner having TR/ TE = 5.99/2.75, flip angle 62°, voxel-size : $0.5 \times 0.5 \times 0.5$ mm³, dimensions : 512x512x88.

Frameless Registration

We have first simulated “frameless” images by cropping the fiducials part from each therapeutic MR image (figure A.2(b)). The obtained frameless images were registered afterwards to their corresponding CT (figure A.2(c)) by a rigid transform (six degrees of freedom) and Mutual Information as similarity metric within 3D Slicer BRAINSFit module [16]. Our choice of similarity metric is supported with the findings of Skrel et al.[17], which classifies the Mutual Information as the most appropriate measure for CT-MR rigid registration. Moreover, the Image MergeTM module from the LGP software is also based on the Mutual Information between the images.

This process allowed the estimation of the transform that should be applied to one MR image in order to transform it into the corresponding CT space, without taking into account the

A.1. Assessment of Frameless versus Frame-based Registration of Computed Tomography and Magnetic Resonance Imaging in Gamma Knife Surgery Planning

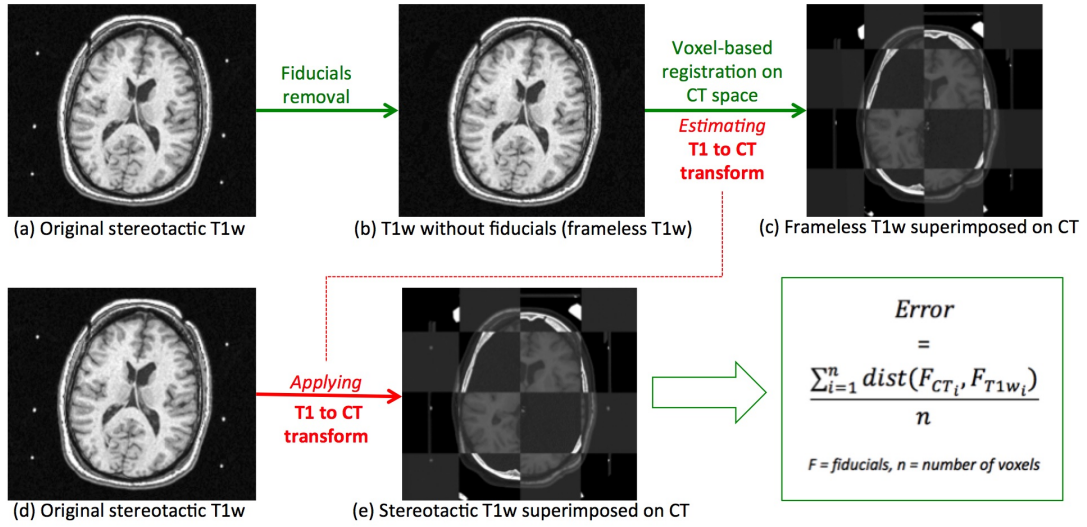


FIGURE A.2 – Schematic overview of the employed validation framework

prior knowledge of the stereotactic fiducials. Hence, the estimated registration transforms were applied on each respective original MR image (the therapeutic MR image with frame, figure A.2(d)) and consequently we have brought both fiducials (from CT and from MR) in the same image space without considering them as a registration reference (figure A.2(e)). Figure 2 gives a schematic overview of the explained methodology.

This procedure was applied for both non-injected and the injected T1w images. For T2 CISS, the process of rigid-registration estimation was slightly different. Due to the challenge of matching images with very different fields of view (the T2 CISS of our dataset have a very small FOV), we first estimated the transform that brings the CT image to the T2 CISS space (without fiducials) and then we applied its inverse to the T2 CISS.

Error Estimation

The estimation of the registration error was obtained by calculating the mismatch between the CT and the MR fiducials. In other words, we want to express the error as a distance between the points that should ideally be aligned.

There are certain differences between the CT and MR fiducials that should be considered. In fact, to accommodate the requirements for the imaging process, both CT and the MR images are acquired with physically different Indicator Boxes (figure A.1). The fiducials for the CT scans are made of high contrast copper material rods, while those for MRI, of tubing filled with copper sulphate. There is also a dissemblance between the shapes in the top and the bottom part of the fiducials (see figures A.1, A.3 and A.4). Additionally, as it is very well known by the GKS users, in the MRI sequences, geometrical distortion are observed near the top and the right part of the fiducials. For these reasons, the comparison between the CT and MR

Annexe A. Appendixes

fiducials was done in a volume of interest (VOI) i.e. a volume enclosing the middle part of the indicators, starting 5 mm below the top extreme and ending 5 mm above the lowest fiducials' point (figures A.3(a) and A.3(b)).

Similarly to CT, T1w MR fiducials were also extracted from the VOI by applying a threshold that was empirically set to 200 for all T1w-dataset. Isolated voxels were again eliminated by keeping only regions with more than 1000 connected voxels. For T2 CISS images, the considered VOI was smaller due to their limited field of view (see figures A.3(c) and A.3(d)). The threshold for extracting their fiducials was empirically set to 400, while the one for removing isolated regions to 500 voxels. The MR fiducials were then superimposed to the corresponding CT distance-map. Therefore the error was calculated as the mean value of the distances between each corresponding fiducial point.

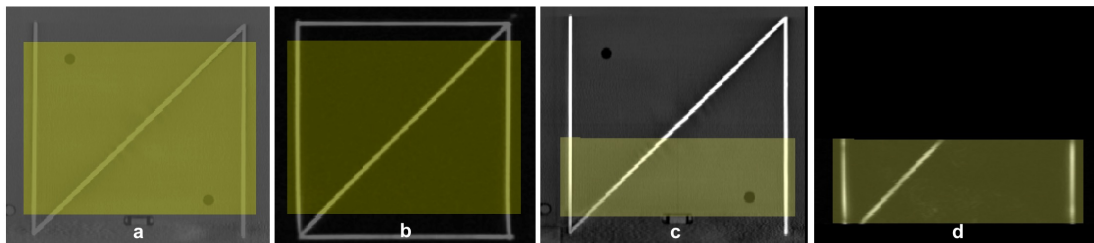


FIGURE A.3 – The fiducials and the volume of interest (VOI, the yellow zone) in which the registration error is calculated. In (a) and (c) are shown the CT fiducials, in (b) those from the T1w images and in (d) from the T2 CISS. The ROI for the T1w images is represented in (a) and (b), while (c) and (d) show the ROI for T2 CISS.

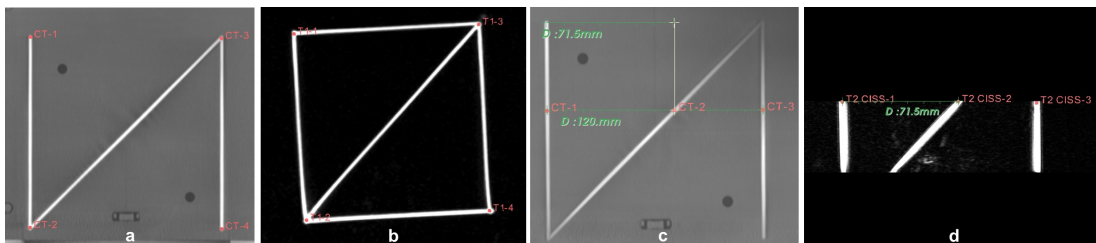


FIGURE A.4 – The chosen landmarks for the frame-based registration shown on the right side of the fiducials. The selected points for the landmark registration between CT and T1w are presented in (a) and (b), and in (c) and (d) those for the CT-T2 CISS matching along with the measurements done for this purpose.

Frame-based Registration

Similarly to the LGP procedure, we additionally perform a landmark-based registration. For this aim we use the Fiducial Registration module from the 3D Slicer software estimating again a six-parameter transform (<http://slicer.org>).

We explored this frame-based matching for the following set of images :

A.1. Assessment of Frameless versus Frame-based Registration of Computed Tomography and Magnetic Resonance Imaging in Gamma Knife Surgery Planning

- Between the non-injected T1w and the CT of all 30 patients, where for each image the extreme fiducials points were chosen as landmarks (4 from the left and 4 from the right frame, see figures A.4(a) and A.4(b)).
- Between the T2 CISS and the CT, where 6 landmarks were considered (3 from each side taken from the top T2 CISS slice). To ensure a precise selection of the landmarks on both modalities, we first measured the distances between the chosen T2 CISS points and then we have selected the corresponding CT landmarks (see figures A.4(c) and A.4(d)).

Finally, the registration error was calculated as described above, in section *Error Estimation*.

Frameless vs. Frame-based Registration

A Wilcoxon Signed-Rank test was performed in order to evaluate the statistical difference between the calculated errors committed with the frame-less and the frame-based registration techniques.

Results

Subjects with no significant deformation of the brain's parenchyma

T1w images. The voxel-based registration errors are in the range between 0.41 mm and 0.70 mm among all 20 patients with a maximal variance of 0.46 mm. Moreover, there were no significant differences between the outcomes of the two registration methods ($p=0.44$, applying Wilcoxon Signed-Rank test). In fact, the observed error values for the frame-based registration were between 0.39 mm and 0.69 mm with a maximal variance of 0.41 mm. A boxplot of the error statistics is shown in figure A.5. As a reference level, the T1w spatial resolution of 1mm is shown with a black line.

Injected T1w images. The errors estimated for the frameless registration of the injected T1w images were very similar to those of the non-injected considering the same MI-based registration technique. In this case the values were in the interval between 0.39 mm and 0.62 mm with maximal variance of 0.33 mm (see figure A.6). The Wilcoxon Signed-Rank test's score of $p=0.98$ showed that there is high correlation between the voxel-based registration outcomes of these two T1w modalities.

T2 CISS images. Three subjects were excluded from T2 CISS set of analysis since the voxel-based registration failed to match the respective images. In fact, in the physical image space, the T2 CISS images of those 3 cases were considerably more distant from their corresponding CT. Consequently to this, for a small FOV as the one of the used T2 CISS, the registration method was unable to estimate the correct transform. We assume that an initial manual approaching of the images could overcome this limitation but, since here we are aiming to present only the results coming from a fully automatic image registration method, we did not

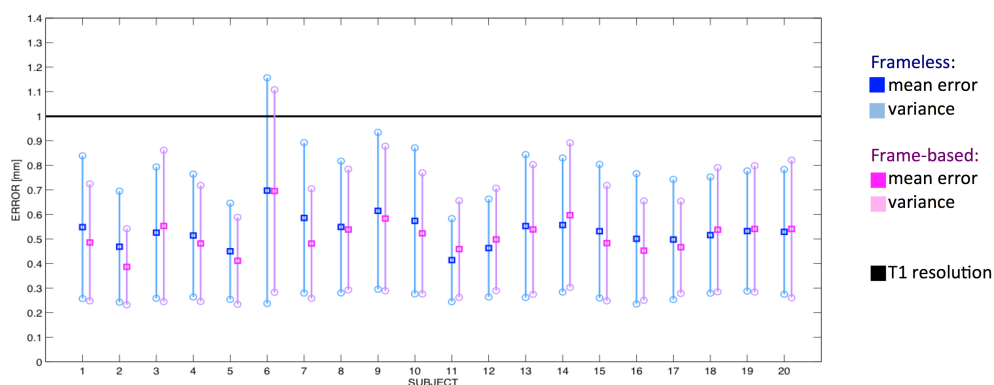


FIGURE A.5 – Statistical boxplot describing our findings considering the T1w images acquired from patients with no significant deformation of the brain. In pink are shown the results of the voxel-based registration and in blue those from the landmark-based. The black horizontal line gives a reference for the smallest spatial resolution of the images that we are transforming during the registration (T1w).

further extent the study.

For the final set of 7 images, the calculated error for the voxel-based registration was between 0.35 mm and 0.57 mm with maximum variance of 0.3 mm, while for the landmarks-based registration between 0.32 mm and 0.60 mm with maximum variance of 0.34 mm (see figure A.7). The statistical comparison with a score of $p=0.7$ showed that there is no significant difference between the outcomes of both registration techniques even for this modality.

Subjects with significant deformation of the brain’s parenchyma

Error lower than 1mm for the CT-T1w registration was calculated even for those cases where, due to the pathology, there is an important shifting of the brain’s parenchyma. More precisely, the estimated error for all 10 subjects with brain metastasis was in the range between 0.46 mm and 0.63 mm with a maximum variance of 0.35 mm. The landmarks-based registration gave similar errors : between 0.46 mm and 0.60 mm with a maximum variance of 0.33 mm (see figure A.8). Furthermore, the corresponding errors from both registration techniques were again non-statistically different ($p=0.38$).

Discussion

Our study has shown a confidently high precision of the voxel-based registration transform between CT and several MR modalities.

In the case of T1w images, we estimated an error lower than its spatial resolution with a small variance. Moreover, Wilcoxon Signed-Rank test showed no statistical difference between this error with the one committed while applying a landmark-based registration, the gold standard

A.1. Assessment of Frameless versus Frame-based Registration of Computed Tomography and Magnetic Resonance Imaging in Gamma Knife Surgery Planning

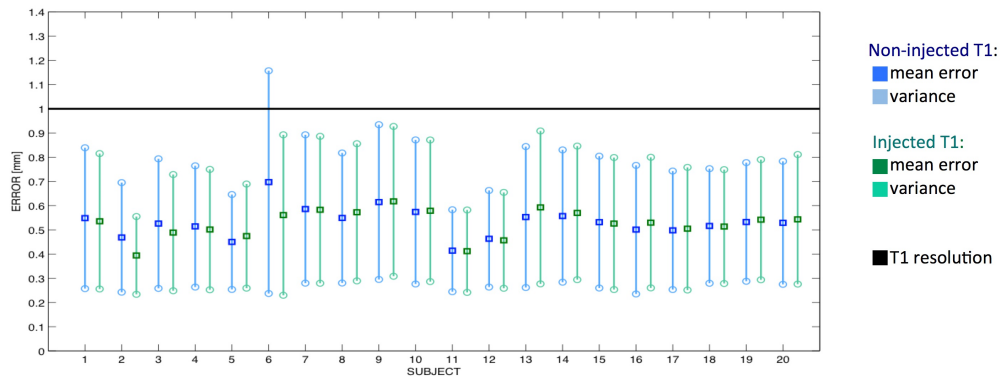


FIGURE A.6 – Statistical boxplot comparing visually the errors estimated for the frameless registration between T1w and CT (blue) and injected T1w and CT (green). The black horizontal line gives a reference for the smallest spatial resolution of the images being transformed (the non-injected and the injected T1w).

for GKS treatment planning.

Furthermore, the high correlation between the outcomes of the frameless CT-non-injected T1w and CT-injected T1w matching affirms that the registration result will not be affected by our choice to work with the injected T1w image instead of the non-injected one and vice-versa.

The results of the dataset coming from patients with metastases were in the same range as the estimated error for the dataset of subjects without brain deformation. Consequently to this, we showed that even in the case of images presenting brain abnormalities and therefore, no regular levels of intensity, we can still be confident in the frameless registration outcome.

For the T2 CISS images the obtained error ($<0.6\text{mm}$) was comparable to its spatial resolution. The Wilcoxon Signed-Rank test demonstrated a high correlation between the frameless and the frame-based registration, which again, affirms equivalency between both registration techniques. However, these results should be taken with caution because here, we worked with a relatively low number of cases (10) and for 30% of them the voxel-registration failed to match the images. Therefore, further studies on extended T2 CISS dataset should be realized in order to conclude this behaviour.

The voxel-based transform inside LGP is provided by the Image MergeTM module, which performs a transform with six degrees of freedom using mutual information between the images and a global optimizer. We performed our study outside LGP; however, since we used the same standard 3D image registration techniques as within the station, our findings remain relevant.

As we already mentioned, around the top and the bottom part of the MR Indicator Box there are geometrical distortion in the images that deforms the fiducials corners. Knowing this, our T1w landmarks were chosen in the exact crossing point between the corresponding vertical and horizontal line of the fiducials, regardless of this distortion. Still, in order to evaluate

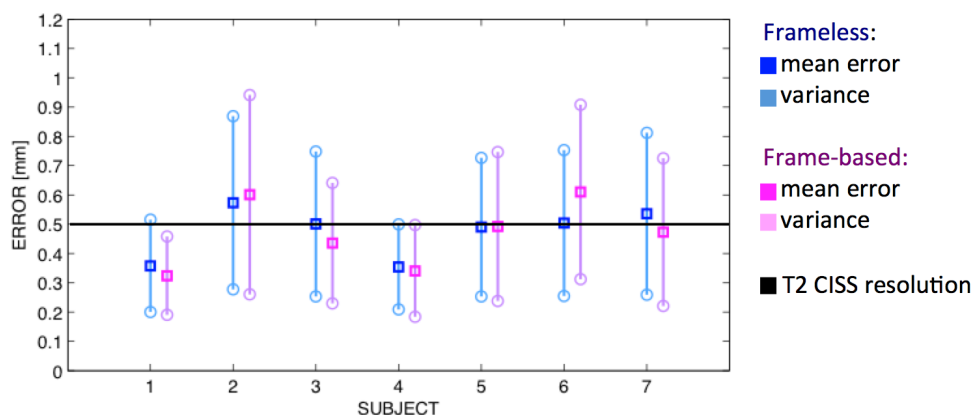


FIGURE A.7 – Statistical boxplot comparing visually the errors estimated for the frameless (blue) and the frame-based (pink) registration between T2 CISS and CT. The black horizontal line gives a reference for the spatial resolution of the image being transformed (T2 CISS).

the influence of landmark selection on the error estimation, we have performed additional frame-based registration for 4 cases of T1w images, where the landmarks were chosen in the middle part of the frame (2 cm above the bottom and 2 cm below the top fiducial line, respectively). The obtained errors were then compared with the corresponding ones of the landmark-based transform shown in this study. The difference between the estimated errors was in the order of 0.01 mm, which was the reason for remaining confident in our choice of landmarks.

Since CT and MR images are acquired with different Indicator Boxes, there is a probability of slight dissemblance between the thicknesses of the respective fiducials, which could induce an additional systematic error contributing to the error we evaluate. A systematic error might also be present as a consequence of an imperfect extraction of the frame from the images or the linear interpolation applied to the transformed image. Therefore, our reported error values might be slightly overestimated, but they remain valid nevertheless. Eventually, they would even become lower by overcoming the above limitations.

Our study strongly surpasses the limitation of the previously reported ones. Our advantages with respect to the previous reported studies are : 1) we are using a big dataset of real clinical images enclosing 3 different MRI contrasts from 30 patients either with non-significant or big brain deformation ; 2) we rely on the most reliable reference of comparison - the fiducials of the Indicator Box, for estimation of the voxel-based registration quality ; and 3) we compare statistically with the outcome of the landmark-based registration, which is currently considered as a gold standard for defining the therapeutic images with the stereotactic frame inside the LGP reference space.

A.1. Assessment of Frameless versus Frame-based Registration of Computed Tomography and Magnetic Resonance Imaging in Gamma Knife Surgery Planning

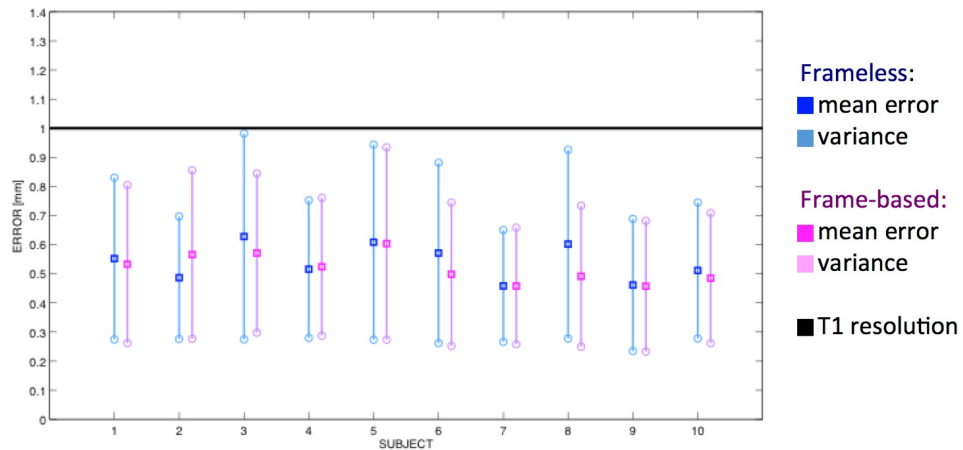


FIGURE A.8 – Statistical boxplot comparing visually the errors estimated for the frameless (blue) and the frame-based (pink) registration between T1w and CT acquired from patients with brain metastasis. The black horizontal line gives a reference for the spatial resolution of the image being transformed (T1w).

Conclusions

Our study has demonstrated a high accuracy of the linear voxel-based registration between the CT and different MR modalities used for stereotactic radiosurgery planning. Furthermore, we have also shown that this frameless registration method is statistically equivalent to the fiducials-based matching, which is seen as the gold standard in everyday practice of Gamma Knife surgery treatment planning.

A.2 Thalamic parcellation

A.2.1 Supplementary material

The following figures were presented as supplementary material for the paper “**Robust thalamic nuclei segmentation method based on local diffusion magnetic resonance properties**“ with co-authors : E. Najdenovska, G. Battistella, P. Maeder, N. Ghazaleh, A. Daducci, J.-P. Thiran, S. Jacquemont, C. Tuleasca, M. Levivier, E. Fornari and M. Bach Cuadra published in **Brain Structure and Function** 2017, Volume 222, Issue 5, pp 2203–2216.

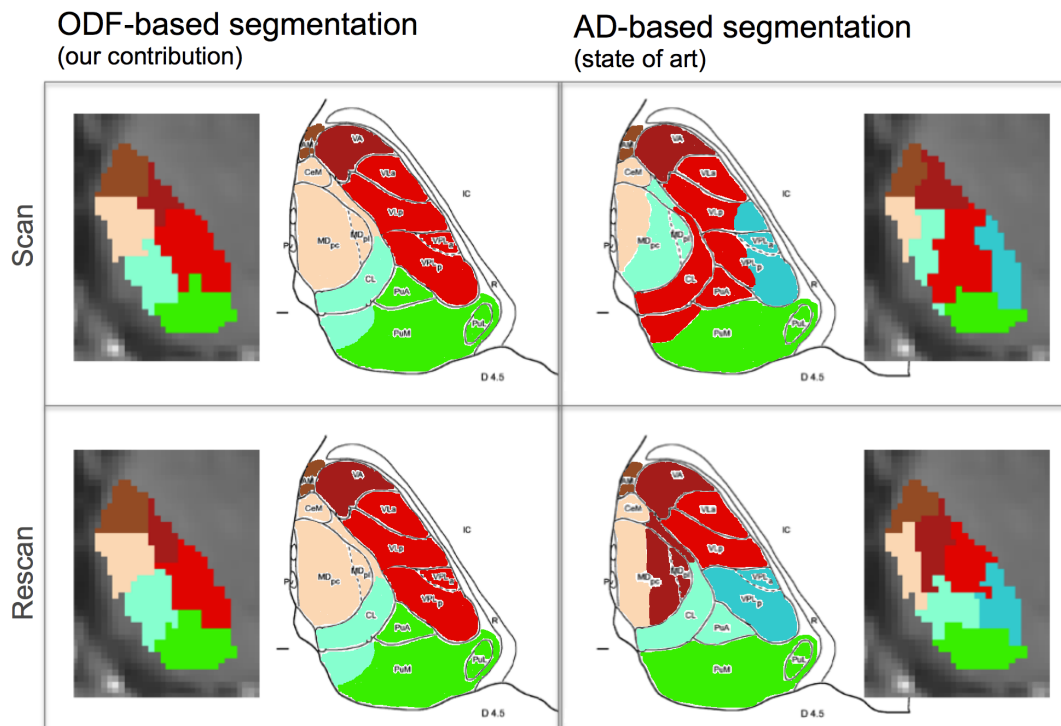


FIGURE A.9 – Single-subject comparison with the axial slice D 4.5 of Morel's atlas

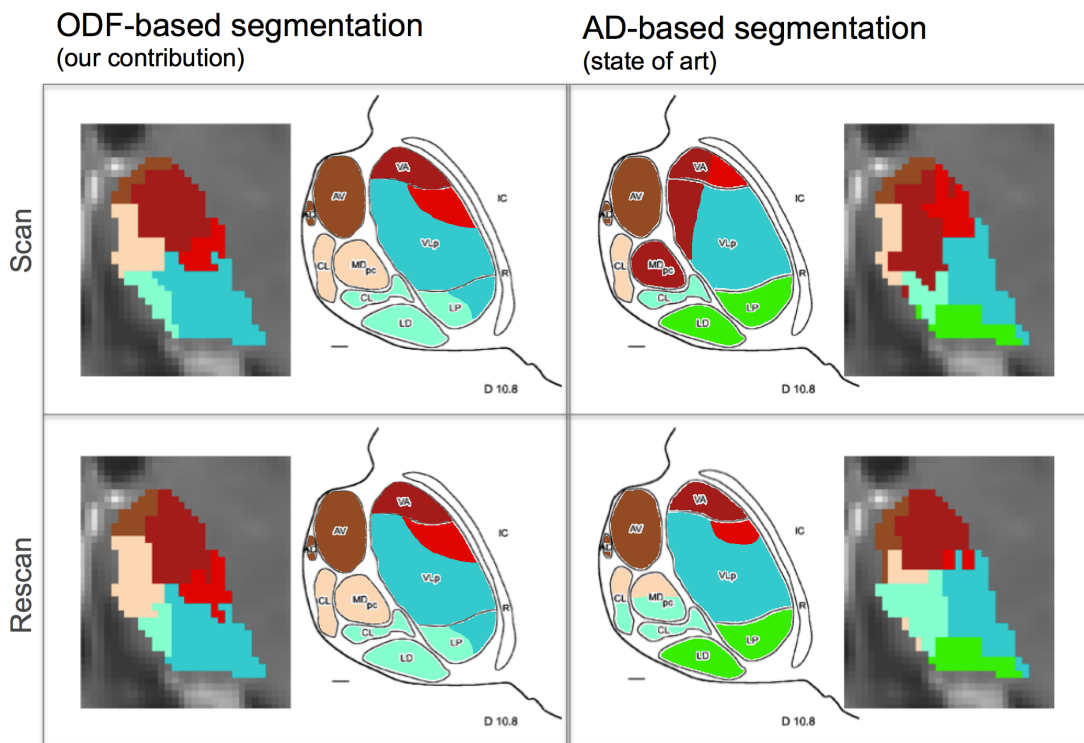


FIGURE A.10 – Single-subject comparison with the axial slice D 10.8 of Morel's atlas

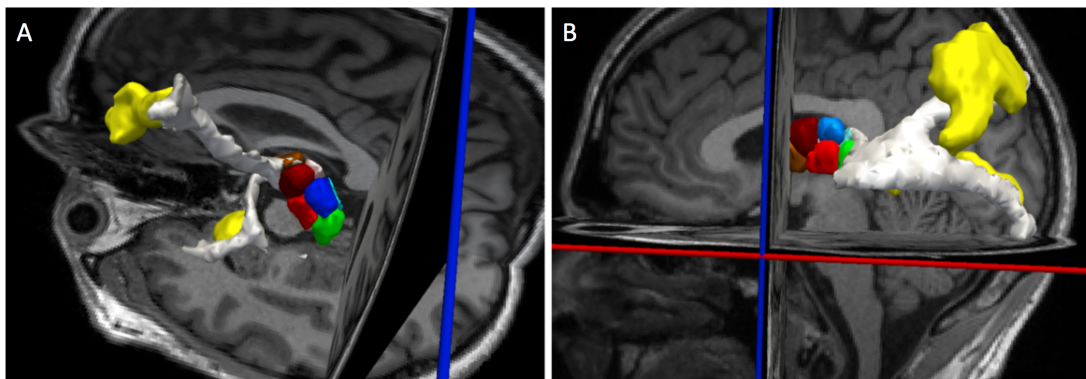


FIGURE A.11 – Reconstruction of thalamic long connections. 3D views of the reconstructed fiber tracts (in white) for the Medio-Dorsal group (panel A) and the Pulvinar (panel B). Probabilistic tracts were reconstructed using the whole thalamus mask and the following seed regions (in yellow) : left middle frontal sulcus and amygdala for the MD group, and left inferior angular gyrus and left calcarine sulcus for the Pulvinar.

A.2.2 Study extension

To further test the robustness of the proposed method for thalamic parcellation for other diffusion sequences, the evaluation of the framework was extended for a cohort of 73 healthy subjects coming from the Human Connectome Project (HCP) database [18, 19].

Annexe A. Appendixes

The dataset included T1w sequences (MPRAGE contrast, TR 2400 ms, TE 2.14 ms, TI 1000 ms, FOV 224x224 mm, voxel size 0.7 mm isotropic) and a multi-shell DWI sequence (spin-echo EPI acquisition, 270 diffusion weighted volumes over 3 shells i.e. for 3 b-values :1000, 2000 and 3000 s/mm² and 18 b₀ volumes, TR 5520 ms, TE 89.5 ms, FOV 210x180 mm, voxel size 1.25 mm isotropic). The acquisition was done with Siemens 3T Skyra scanner in Washington University or University of Minnesota.

The thalamus masks were again initially obtained from the FreeSurfer (v 5.3.0) parcellation on each T1w and then refined accordingly to the proposed method. To calculate the FA map, the tensor fitting was estimated on the diffusion images acquired with b=1000s/mm². The rest of the processing was following the steps described beforehand (in chapter 2)

The parcellation of the thalamus showed the same segmentation pattern for 67 out of the 73 subjects. In the remaining six subjects, for reasons that should be further explored, the outcome did not correspond to the expected spatial distribution of the clusters, therefore there were considered as a failure. Nevertheless, with success rate of approximately 92% we demonstrated the robustness of our algorithm for diffusion data acquired in multi-shell setting and furthermore, with improved spatial resolution.

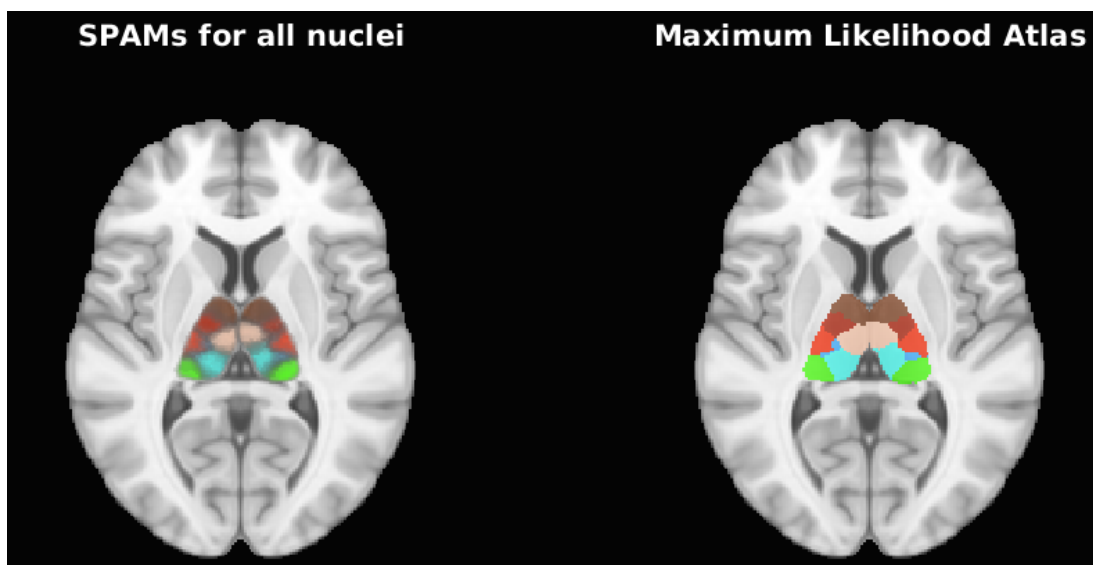


FIGURE A.12 – Illustration of the build atlas in an axial view

These results were used for building spatial probabilistic atlas maps (SPAM) for each cluster in MNI space (see figure A.12). Such a tool could further provide an atlas-based thalamic subsegmentation for subjects where the diffusion data is not available. This work is currently under preparation for submitting it to the journal Scientific Data in Nature entitled as "**A probabilistic atlas of the human thalamic nuclei based on diffusion Magnetic Resonance Image segmentation**" with co-authors Elena Najdenovska, Yasser Alemán-Gómez, Giovanni Battistella, Allesandra Griffa, Maxime Descoteaux, Patric Hagmann, Sebastien Jacquemont, Philippe Maeder, Jean-Philippe Thiran, Eleonora Fornari and Meritxell Bach Cuadra.

Bibliographie

- [1] M. Levivier, T. Gevaert, L. Negretti, Gamma Knife, CyberKnife, TomoTherapy : gadgets or useful tools ?, *Current Opinion in Neurology* 24 (6) (2011) 616–625.
- [2] P. Hanssens, B. Karlsson, T. T. Yeo, N. Chou, G. Beute, Detection of brain micrometastases by high-resolution stereotactic magnetic resonance imaging and its impact on the timing of and risk for distant recurrences, *Journal of Neurosurgery* 115 (3) (2011) 499–504.
- [3] B. Lippitz, C. Lindquist, I. Paddick, D. Peterson, K. O'Neill, R. Beaney, Stereotactic radiosurgery in the treatment of brain metastases : the current evidence, *Cancer Treatment Reviews* 40 (1) (2014) 48–59.
- [4] C. Tuleasca, R. Carron, N. Resseguier, A. Donnet, P. Roussel, J. Gaudart, M. Levivier, J. Régis, Patterns of pain-free response in 497 cases of classic trigeminal neuralgia treated with Gamma Knife surgery and followed up for least 1 year, *Journal of Neurosurgery* 117 Suppl (2012) 181–188.
- [5] J. Régis, R. Carron, C. Delsanti, D. Porcheron, J.-M. Thomassin, X. Murracchiole, P.-H. Roche, Radiosurgery for vestibular schwannomas, *Neurosurgery Clinics of North America* 24 (4) (2013) 521–530.
- [6] C. Ohye, Y. Higuchi, T. Shibasaki, T. Hashimoto, T. Koyama, T. Hirai, S. Matsuda, T. Serizawa, T. Hori, M. Hayashi, T. Ochiai, H. Samura, K. Yamashiro, Gamma knife thalamotomy for Parkinson disease and essential tremor : a prospective multicenter study, *Neurosurgery* 70 (3) (2012) 526–536.
- [7] C. Yu, M. L. Apuzzo, C. S. Zee, Z. Petrovich, A phantom study of the geometric accuracy of computed tomographic and magnetic resonance imaging stereotactic localization with the Leksell stereotactic system, *Neurosurgery* 48 (5) (2001) 1092–1098 ; discussion 1098–1099.
- [8] B. Fischl, D. H. Salat, E. Busa, M. Albert, M. Dieterich, C. Haselgrove, A. van der Kouwe, R. Killiany, D. Kennedy, S. Klaveness, A. Montillo, N. Makris, B. Rosen, A. M. Dale, Whole brain segmentation : automated labeling of neuroanatomical structures in the human brain, *Neuron* 33 (3) (2002) 341–355.
- [9] C. P. Karger, P. Hipp, M. Henze, G. Echner, A. Hoss, L. Schad, G. H. Hartmann, Stereotactic imaging for radiotherapy : accuracy of CT, MRI, PET and SPECT, *Physics in Medicine and Biology* 48 (2) (2003) 211–221.
- [10] C. Tuleasca, R. Carron, N. Resseguier, A. Donnet, P. Roussel, J. Gaudart, M. Levivier, J. Régis, Multiple sclerosis-related trigeminal neuralgia : a prospective series of 43 patients treated with gamma knife surgery with more than one year of follow-up, *Stereotactic and Functional Neurosurgery* 92 (4) (2014) 203–210.

Bibliography

- [11] Y. Watanabe, E. Han, Image registration accuracy of GammaPlan : a phantom study, *Journal of Neurosurgery* 109 Suppl.
- [12] S. Thomas, S. Sampath, B. IndiraDevi, G. Bhanumathy, S. Supe, M. Musthafa, A novel technique to evaluate the geometrical accuracy of CT-MR image fusion in Gamma Knife radiosurgery procedures, *Polish Journal of Medical Physics And Engineering* 16 (2) (2011) 55–66.
- [13] H. Nakazawa, Y. Mori, M. Komori, Y. Shibamoto, T. Tsugawa, T. Kobayashi, C. Hashizume, Validation of accuracy in image co-registration with computed tomography and magnetic resonance imaging in Gamma Knife radiosurgery, *Journal of Radiation Research* 55 (5) (2014) 924–933.
- [14] Y. Watanabe, C. K. Lee, B. J. Gerbi, Geometrical accuracy of a 3-tesla magnetic resonance imaging unit in Gamma Knife surgery, *Journal of Neurosurgery* 105 Suppl (2006) 190–193.
- [15] W. T. Koos, J. D. Day, C. Matula, D. I. Levy, Neurotopographic considerations in the microsurgical treatment of small acoustic neurinomas, *Journal of Neurosurgery* 88 (3) (1998) 506–512.
- [16] H. J. Johnson, G. Harris, K. Williams, BRAINSFit : Mutual Information Registrations of Whole-Brain 3d Images, Using the Insight Toolkit.
- [17] D. Skerl, B. Likar, J. M. Fitzpatrick, F. Pernus, Comparative evaluation of similarity measures for the rigid registration of multi-modal head images, *Physics in Medicine and Biology* 52 (18) (2007) 5587–5601.
- [18] S. N. Sotiropoulos, S. Jbabdi, J. Xu, J. L. Andersson, S. Moeller, E. J. Auerbach, M. F. Glasser, M. Hernandez, G. Sapiro, M. Jenkinson, D. A. Feinberg, E. Yacoub, C. Lenglet, D. C. Van Essen, K. Ugurbil, T. E. J. Behrens, WU-Minn HCP Consortium, Advances in diffusion MRI acquisition and processing in the Human Connectome Project, *NeuroImage* 80 (2013) 125–143.
- [19] D. C. Van Essen, S. M. Smith, D. M. Barch, T. E. J. Behrens, E. Yacoub, K. Ugurbil, WU-Minn HCP Consortium, The WU-Minn Human Connectome Project : an overview, *NeuroImage* 80 (2013) 62–79.

Education

PhD in Life Sciences	Centre d'Imagerie BioMedicale (CIBM), University of Lausanne (UNIL) 2014-2018 <ul style="list-style-type: none"> • Thesis Project: « Multi-modal MR image processing at high field for thalamic nuclei segmentation: application to Gamma Knife Radiosurgery Planning » (under direction of Prof. M. Levivier and Dr. M. Bach Cuadra) <ul style="list-style-type: none"> ○ <i>Task:</i> Providing a MRI-based tool for an automated segmentation of the thalamic nuclei with particular interest on the Vim as the most commonly used target in stereotactic neurosurgery for treatment of tremor ○ <i>Achievements:</i> <ul style="list-style-type: none"> - Recruiting healthy volunteers and acquiring MRI data at 3T and 7T - Developing a robust method based on DWI for thalamic parcellation closely matching the anatomy and outperforming the state-of-art, tested in 200 healthy subjects and patients - Proposing a multi-modal framework for an automated delineation of the Vim area
Master of Science MSc in Electrical and Electronics Engineering	Ecole Polytechnique Fédérale de Lausanne (EPFL), specialization: <i>Information technologies</i> 2010-2012 <ul style="list-style-type: none"> • Master Project: « Brain lesion and tissue segmentation in MRI of stroke patients: acute and chronic stage » (under direction of Prof. J.-P. Thiran and supervision of Dr. Meritxell Bach Cuadra) 2011-2012 Signal Processing Laboratory (LTS5), EPFL in collaboration with Laboratory of Research in Neuroimaging (LREN), CHUV <ul style="list-style-type: none"> ○ <i>Achievement:</i> <i>Developing a framework for an accurate automated segmentation of both healthy and damaged tissue in stroke patients, tested in 85 cases with good performance in 87% of them</i> • Semester Project: « Graph wavelets for adapted domain in image processing » 2011 Medical Image Processing Lab (MIPLab), EPFL (under direction of Prof. Dimitri Van De Ville)
Bachelor of Science BSc in Electrical and Electronics Engineering	Ecole Polytechnique Fédérale de Lausanne 2007-2010 <ul style="list-style-type: none"> • Bachelor Project: « Metric learning with latent information for classification » 2010 Signal Processing Laboratory (LTS2), EPFL (under direction of Prof. Pierre Vanderghenst)
Preparatory Cours CMS	Ecole Polytechnique Fédérale de Lausanne 2006-2007
Secondary School (Mathematics and Science)	« Jane Sandanski » 2002-2006 Strumica, Macedonia

Professional experiences

Researcher Assistant	Neurosurgery Service and Gamma Knife Center in CHUV 11.2012-02.2014 <ul style="list-style-type: none"> • Project: « Image Processing for Gamma Knife Radiosurgery » (supervised by Dr. M. Bach Cuadra)
Internship	Signal Processing Laboratory 5 (EPFL) in a collaboration with Neurosurgery Service and Gamma Knife Center in CHUV 03.2012-11.2012 <ul style="list-style-type: none"> • Project: « Image Processing for Gamma Knife Radiosurgery » (supervised by Dr. M. Bach Cuadra)
Teacher Assistant	<ul style="list-style-type: none"> « Diffusion MRI: from physics to brain networks » (UNIL, Prof. P. Hagmann, Dr. M. Bach Cuadra) 2017-2018 « Introduction to MATLAB » (UNIL, Dr. M. Bach Cuadra and Dr. J.-F. Knebel) 2014-2016 « Structural MRI Analysis for Neuroscientists » (UNIL, Dr. Meritxell Bach Cuadra) 2014-2016 « Analysis I & II » (EPFL, Prof. J. Stubbe) 2010-2011 « Circuits and Systems » (EPFL, Prof. D Atienza Alonso) 2009-2010

Awards

ISMRM Research & Education Foundation pour l'Université de Lausanne	Trainee (Educational) Stipend: waved seven-day registration to the ISMRM 23 rd Annual Meeting 2015 Travel Grant: participation to the 17 th International Meeting of Leksell Gamma Knife Society 2014
---	--

Technical Skills

Operating Systems	MacOS, Linux and Windows
Software	3D Slicer, MITK, Ants, FSL, SPM, FreeSurfer, FiberNavigator, ImageJ, SolidWorks, Altium, LabView, PSpice
Programming languages	Matlab, Bash, C++, Java, Latex, VHDL, Assembleur
Specialization	Medical image processing (MRI: T1w, T2w, DWI, SWI)

Journal Papers

- Brain Structure and Function, 2017 **E. Najdenovska**, G. Battistella, P. Maeder, N. Ghazaleh, A. Daducci, J.-P. Thiran, S. Jacquemont, C. Tuleasca, M. Levivier, M. Bach Cuadra, E. Fornari «**Robust Thalamic Nuclei Segmentation Method Based on Local Diffusion Magnetic Resonance Properties**»
- World Neurosurgery 2018 C. Tuleasca, **E. Najdenovska**, J. Regis, T. Witjas, N. Girard, J. Champoudry, M. Fouzi, J.-P. Thiran, M. Bach Cuadra, M. Levivier and D. Van de Ville «**Ventro Lateral Thalamus abnormal Connectivity in Essential Tremor Before And After Thalamotomy: A resting-state Function Magnetic Resonance Study**»
- World Neurosurgery 2018 C. Tuleasca, J. Regis, **E. Najdenovska**, T. Witjas, N. Girard, J. Champoudry, M. Fouzi, J.-P. Thiran, M. Bach Cuadra, M. Levivier and D. Van de Ville «**Pretherapeutic Functional Imaging Allows Prediction of Head Tremor Arrest After Thalamotomy for Essential tremor: The Role of Altered Interconnectivity Between Thalamolimbic and Supplementary Motor Circuits**»
- Brain 2018 C. Tuleasca, J. Regis, **E. Najdenovska**, T. Witjas, N. Girard, J.-P. Thiran, M. Bach Cuadra, M. Levivier and D. Van de Ville «**Visually-sensitive networks in essential tremor: evidence from structural and functional imaging**»
- Acta Neurologica Scandinavica 2017 C. Tuleasca, **E. Najdenovska**, J. Regis, T. Witjas, N. Girard, J. Champoudry, M. Fouzi, J.-P. Thiran, M. Bach Cuadra, M. Levivier and D. Van de Ville «**Pretherapeutic functional neuroimaging predicts tremor arrest after thalamotomy**»
- Acta Neurochirurgica, 2017 C. Tuleasca, **E. Najdenovska**, J. Regis, T. Witjas, N. Girard, J. Champoudry, M. Faouzi, J.-P. Thiran, M. Bach Cuadra, M. Levivier and D. Van de Ville «**Clinical Response to Vim's Thalamic Stereotactic Radiosurgery for Essential Tremor is associated with distinctive functional connectivity patterns**»
- Acta Neurochirurgica, 2017 C. Tuleasca, E. Pralong, **E. Najdenovska**, M. Bach Cuadra, J. P. Marques, F. Vingerhoets, J. Regis, J. Bloach M. Levivier «**Deep Brain Stimulation After Previous Gamma Knife Thalamotomy of the Vim for Essential Tremor is Feasible! Clinical, Electrophysiological and Radiological Findings**»
- Acta Neurochirurgica, 2017 C. Tuleasca, T. Witjas, **E. Najdenovska**, A. Verger, N. Girard, J. Champoudry, J.-P. Thiran, D. Van de Ville, M. Bach Cuadra, M. Levivier, E. Guedj and J. Regis «**Assessing the clinical outcome of Vim radiosurgery with voxel-based morphometry: visual areas are linked with tremor arrest**»

Conference Presentations

- 20th International Conference on MICCAI Society (09.2017, Québec City, Québec, Canada) **E. Najdenovska**, C. Tuleasca, J. Jorge, J. P. Marques, P. Maeder, J.-P. Thiran, M. Levivier, M. Bach Cuadra, «**Towards an Automated Segmentation of the Ventro-Intermediate Nucleus**» (oral communication)
- 13th International Stereotactic Radiosurgery Society Congress (05.2017, Montreux) **E. Najdenovska**, C. Tuleasca, J. Bloch, P. Maeder, N. Girard, T. Witjas, J. Regis, J.-P. Thiran, M. Bach Cuadra, M. Levivier, «**Exploring Local Diffusion MRI Properties for Vim Localization: Evaluation in Clinical Cases**» (oral communication)
- 13th International Stereotactic Radiosurgery Society Congress (05.2017, Montreux) **E. Najdenovska**, C. Tuleasca, J. P. Marques, J. Jorge, D. Gallichan, P. Maeder, J.-P. Thiran, M. Levivier, M. Bach Cuadra «**Vim's anatomical Landmarks: Indirect Targeting vs. Direct Visualization at 7T MRI**» (oral communication)
- 22nd Annual Meeting of the Organization for Human Brain Mapping (06.2016, Geneva) **E. Najdenovska**, C. Tuleasca, X. Bresson, P. Maeder, G. Battistella, E. Formari, J. Regis, J.-P. Thiran, M. Levivier, M. Bach Cuadra «**Localization of the Ventro-Intermediate Thalamic Nucleus Using Local Diffusion Properties**» (poster)
- ISMRM 23rd Annual Meeting & Exhibition (30.05-05.06.2015, Toronto, Ontario, Canada) **E. Najdenovska**, G. Battistella, C. Tuleasca, P. Maeder, A. Daducci, J.-P. Thiran, M. Levivier, E. Fornari, M. Bach Cuadra «**Novel Robust Segmentation of the Thalamic Nuclei – Validation on Healthy Subjects and patients**» (poster)
- 17th International Meeting of Leksell Gamma Knife Society (05.2014 New York City, USA) **E. Najdenovska**, C. Tuleasca, F. Vingerhoets, J.-P. Thiran, M. Levivier, M. Bach Cuadra «**Assessment of Frameless vs. Frame-based Registration of Computer Tomography and Magnetic Resonance Images in Gamma Knife Surgery Planning**» (oral communication)

Languages

Macedonian	Mother tongue	German	Basic level (A1)
French	Advanced level (C2), daily practice	Spanish	Intermediate level (B1)
English	Advanced level (C2), daily practice	Serbian	Advanced level (C1)
Italian	Intermediate level (B1)	Bulgarian	Intermediate level (B1)
English	Advanced level (C2)		